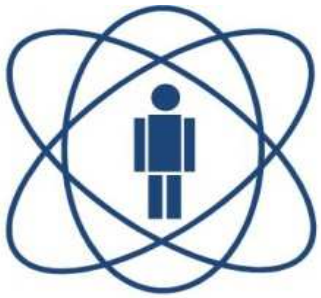

CENTRO BRASILEIRO DE PESQUISAS FÍSICAS
http://www.cbpf.br



CENTRO BRASILEIRO DE PESQUISAS FÍSICAS

Aplicações da Microscopia Eletrônica de Transmissão à Nanotecnologia

André Luiz Pinto

LABNANO

LABORATÓRIO MULTIUSUÁRIO DE NANOCIÊNCIA E NANOTECNOLOGIA (LabNano)



CBPF

















Configuração Atual

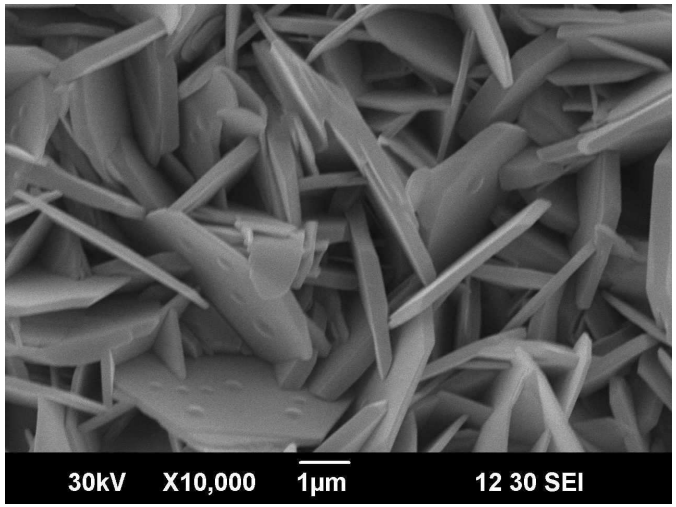
- Sala de Preparação de Amostras
- MEV
- Nanolitografia por Feixe de Elétrons
- Sala Limpa
- Infraestrutura para Deposição de Filmes Finos
- MET

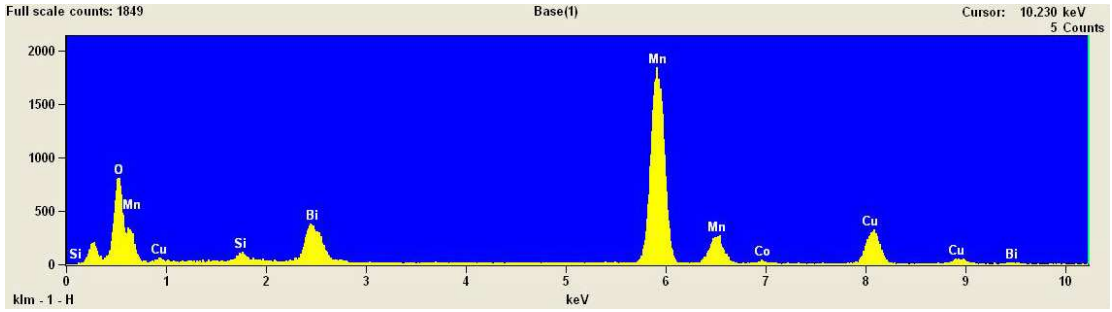


MEV Jeol 6490LV

- MEV-LV
  - Resolução ~ 3 nm
  - Baixo Vácuo (< 300 Pa)
  - EDS



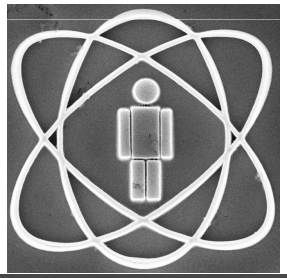


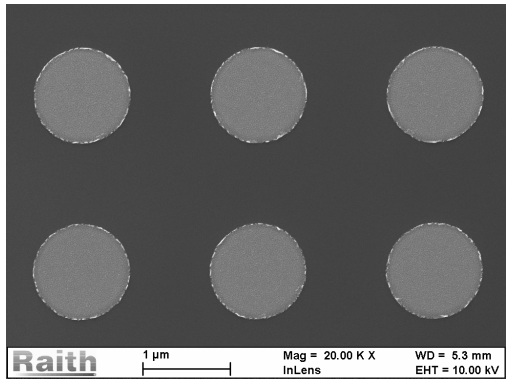


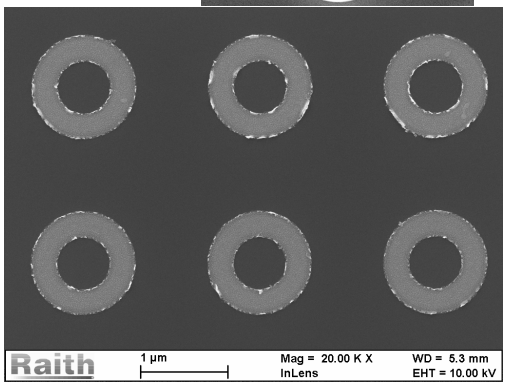
Sistema de Nanolitografia por Feixe de Elétrons - Raith e-line

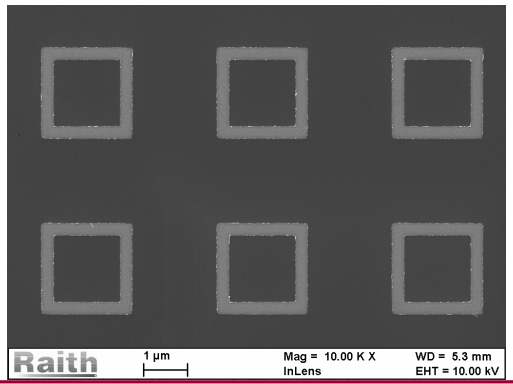
- MEV/Nanolitografia
  - Resolução para imagem ~ 2 nm
  - Resolução para litografia < 20 nm
  - "Stiching" < 40 nm
  - Sobreposição < 40 nm
  - Sistema de injeção de gases
  - Sistema de feixe fixo
  - Nanomanipuladores
  - Sistema de deposição 3D





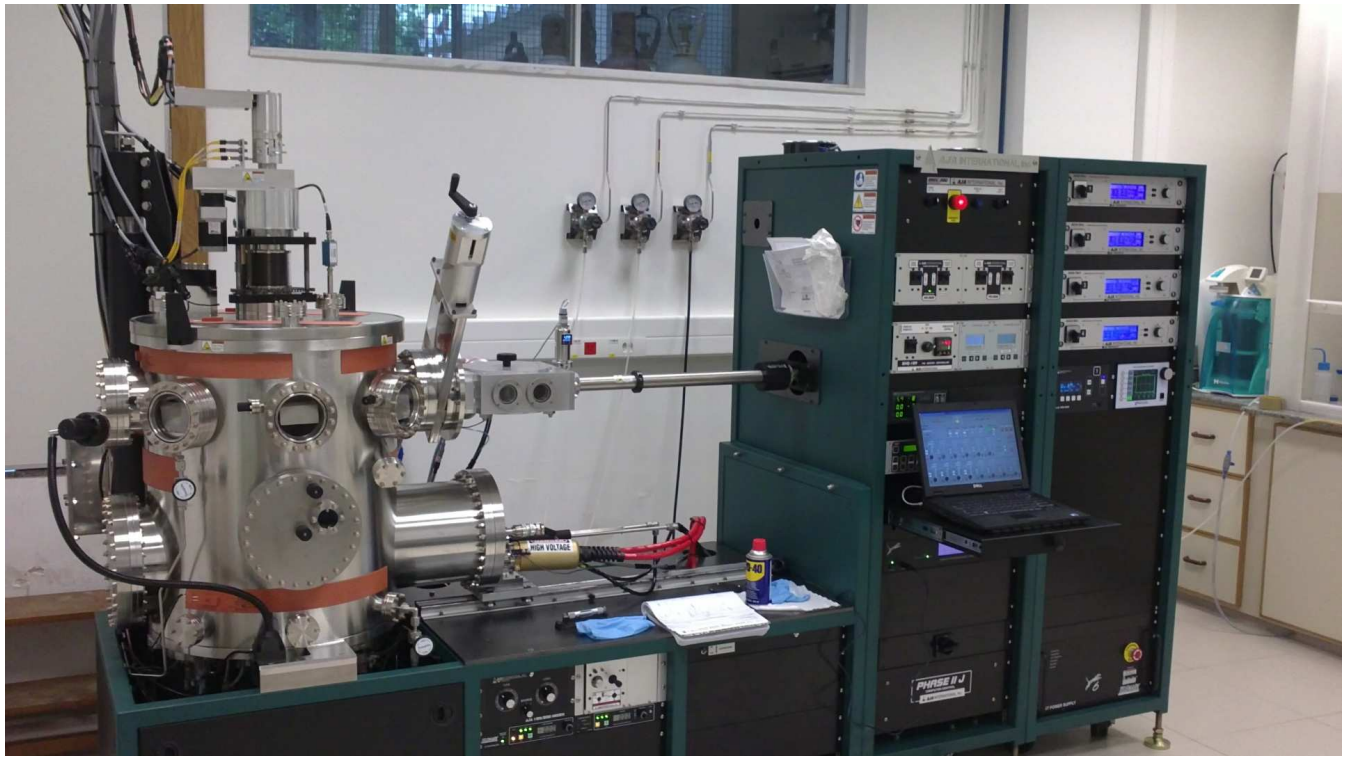






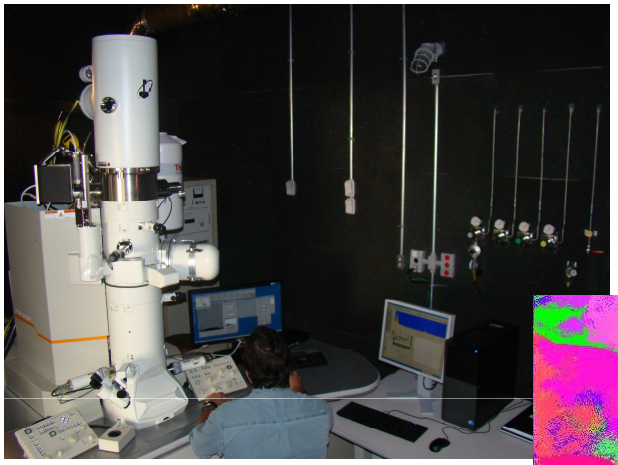
Infraestrutura para Deposição Física

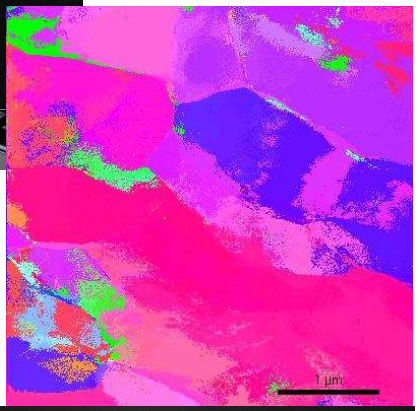
- Ablação a laser
- Sistema de Sputering dedicado a óxidos
- Sistema de Vaporização Catódica

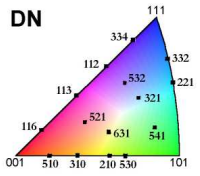


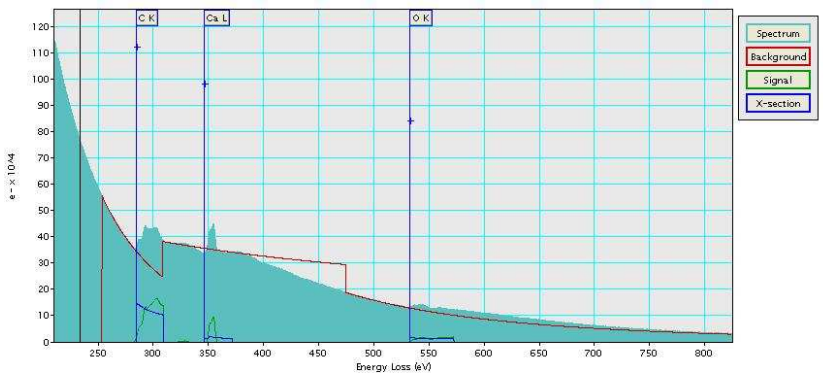
MET-FEG Jeol 2100F

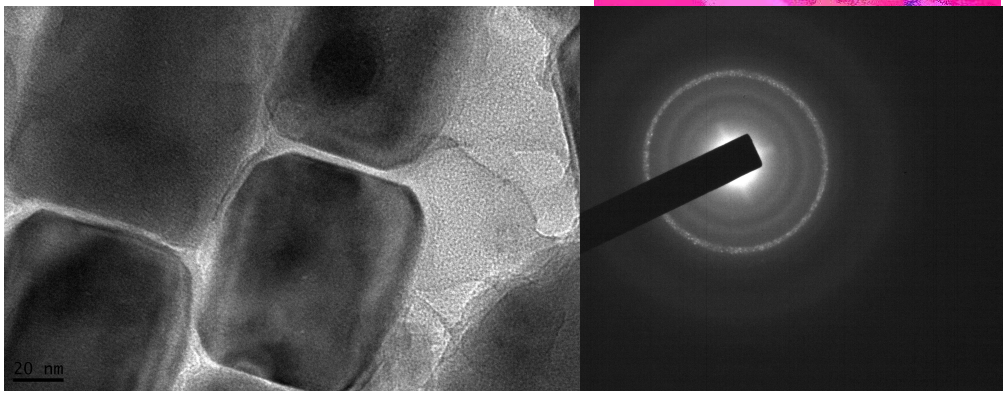
- Características
  - Resolução de ponto ~ 2,3 Å
  - Resolução de rede ~ 1 Å
  - Resolução STEM ~ 1,6 Å
  - HAADF
  - Microscopia de Lorentz
  - EDS
  - EELS
  - Difração com Precessão
  - Biprisma para holografia



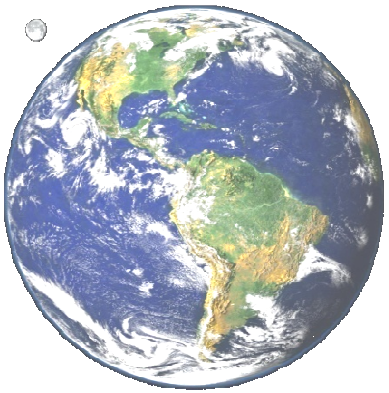








100 milhões de vezes menor

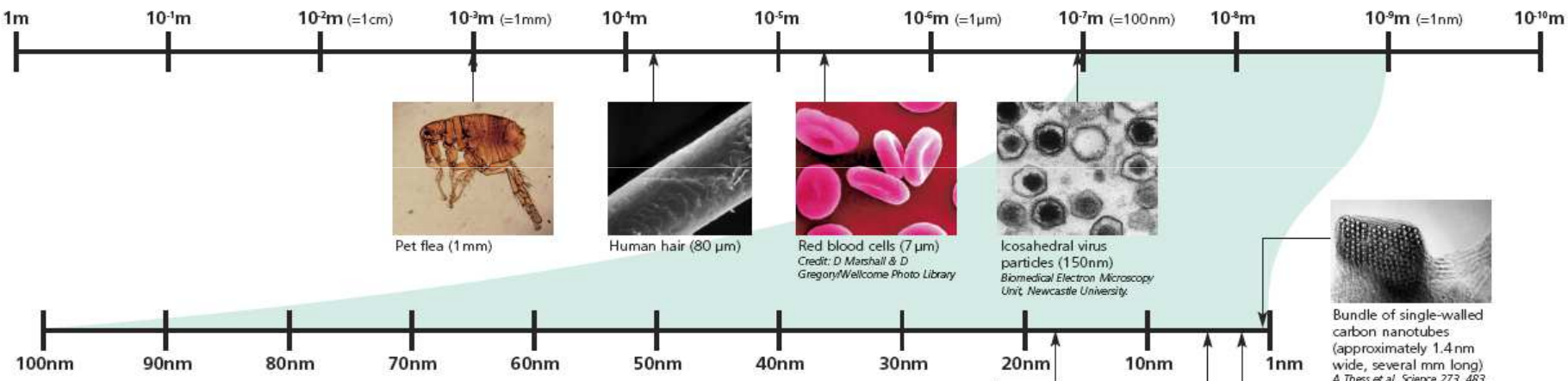




Football (approximately 22 cm)



carbon 60 (0.7 nm)
R.Drautz

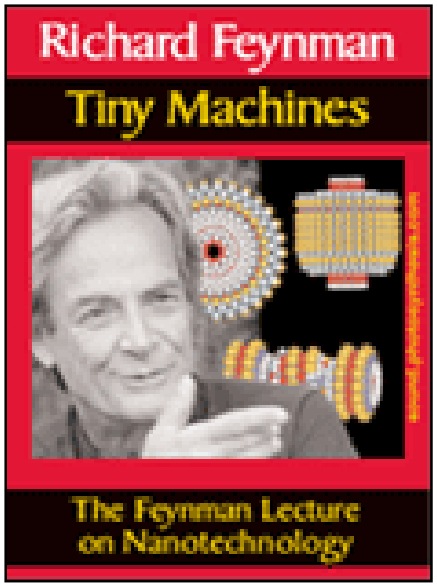


Fonte: The Royal Society & The Royal Academy of Engineering (2004), Nanoscience and nanotechnologies.

the atomic scale - approximately 0.2 nm.

Richard Feynman, 1959
"There's plenty of room at the bottom"

- "The principles of physics, as far as I can see, do not speak against the possibility of maneuvering atom by atom. It is not an attempt to violate any laws; it is something, in principle, that can be done; but in practice, it has not been done because we are too big."



Nosso Arsenal para Observação

- Aumento x Resolução (lateral)



- Olho humano – 0,1 mm
- Microscopia Ótica – 0,5 μm
- Microscópio Eletrônico de Varredura (MEV) – 1 - 4 ηm
- Microscópio Eletrônico de Transmissão (MET) – 0,7 - 1,4 Å
- Microscópio de Ponta de Prova (SPM) – 0,3 Å

Histórico do MET

Ruska recebeu o prêmio Nobel em 1986 pelo 1º microscópio eletrônico (transmissão) construído em 1932

Binnig e Rohrer receberam o Nobel também em 1986 pelo primeiro SPM construído em 1981



Knoll e Ruska em Berlim nos anos 1930

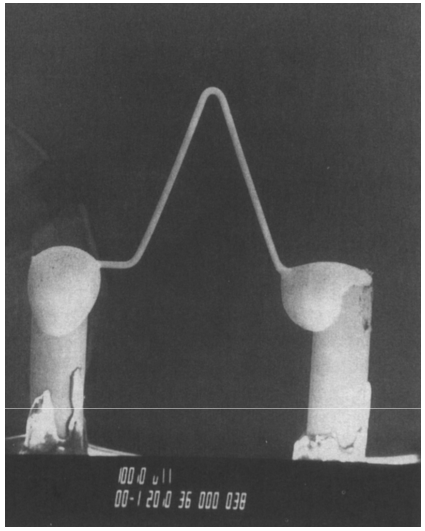
Williams e Carter, 2009

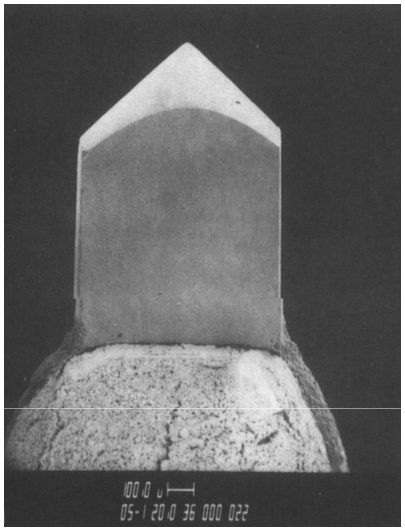
1º MET



http://www.wikipedia.org

Canhões de Elétrons





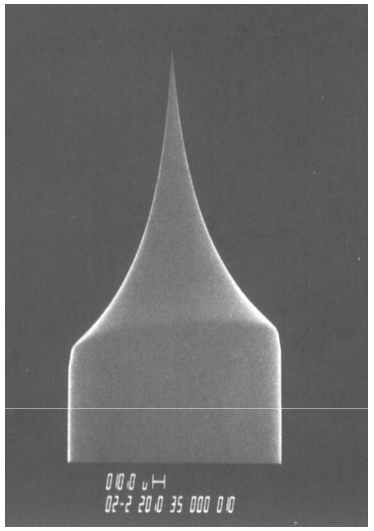


TABLE 5.1 Characteristics of the Principal Electron Sources

	Units	Tungsten	LaB_6	Schottky FEG	Cold FEG
Work function, Φ	eV	4.5	2.4	3.0	4.5
Richardson's constant	A/m^2K^2	6×10^9	4×10^9		
Operating temperature	K	2700	1700	1700	300
Current density (at 100 kV)	A/m^2	5	10^2	10^5	10^6
Crossover size	nm	$> 10^5$	10^4	15	3
Brightness (at 100 kV)	A/m^2sr	10^{10}	5×10^{11}	5×10^{12}	10^{13}
Energy spread (at 100 kV)	eV	3	1.5	0.7	0.3
Emission current stability	%/hr	<1	<1	<1	5
Vacuum	Pa	10^{-2}	10^{-4}	10^{-6}	10^{-9}
Lifetime	hr	100	1000	>5000	>5000

Energia dos Elétrons

- Comprimento de onda

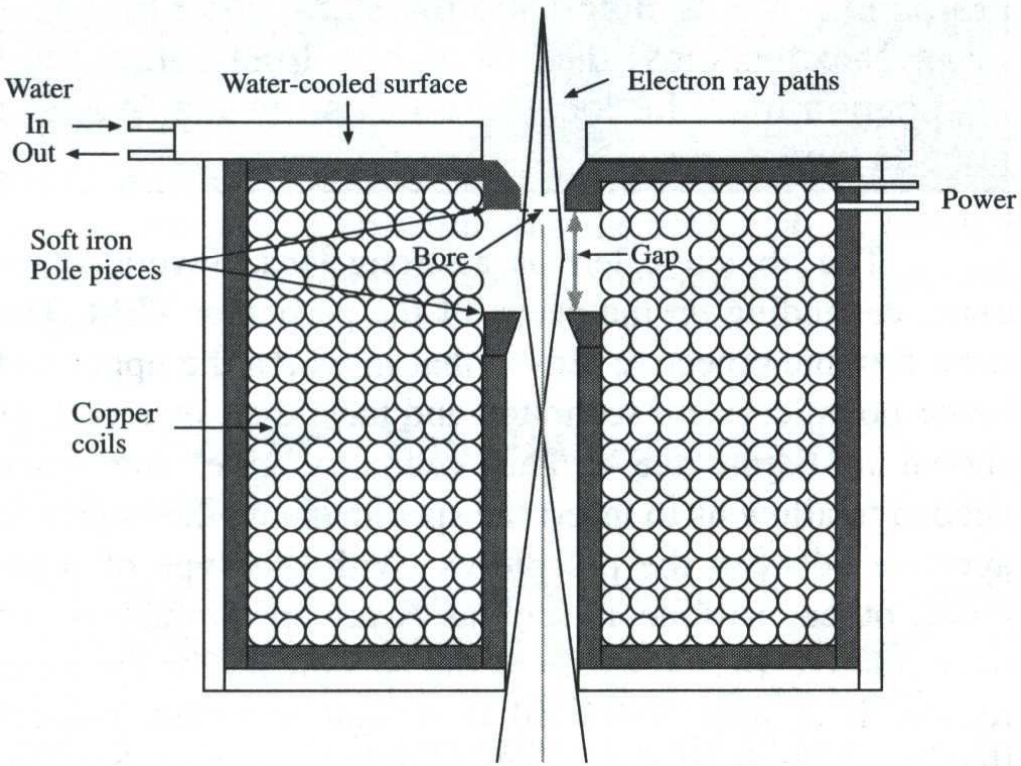
$$\lambda = \frac{h}{\sqrt{2m_o eV}}$$

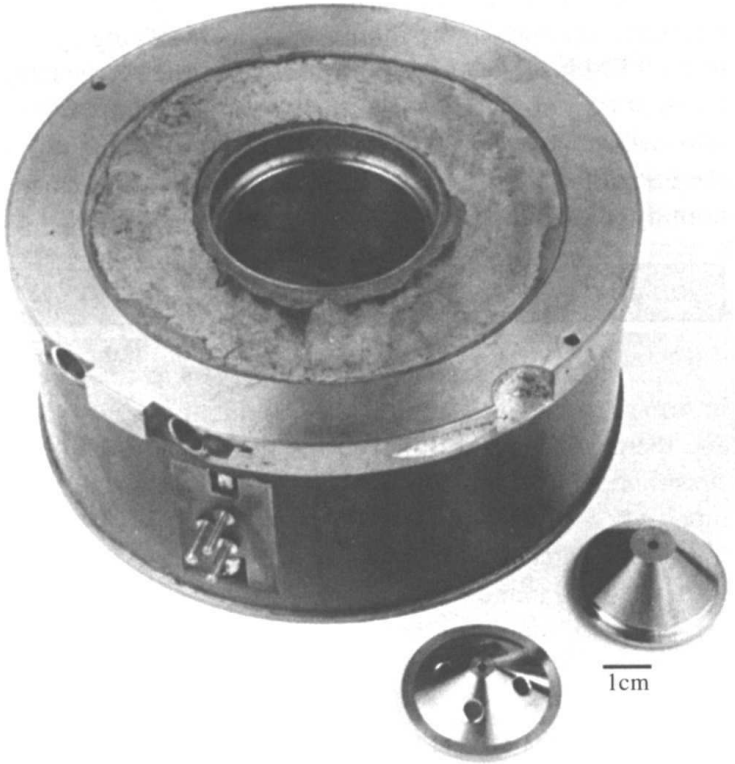
- Correção relativística

$$\lambda = \frac{h}{\sqrt{2m_o eV\left(1+\frac{eV}{2m_o c^2}\right)}}$$

Lentes em Microscopia Eletrônica

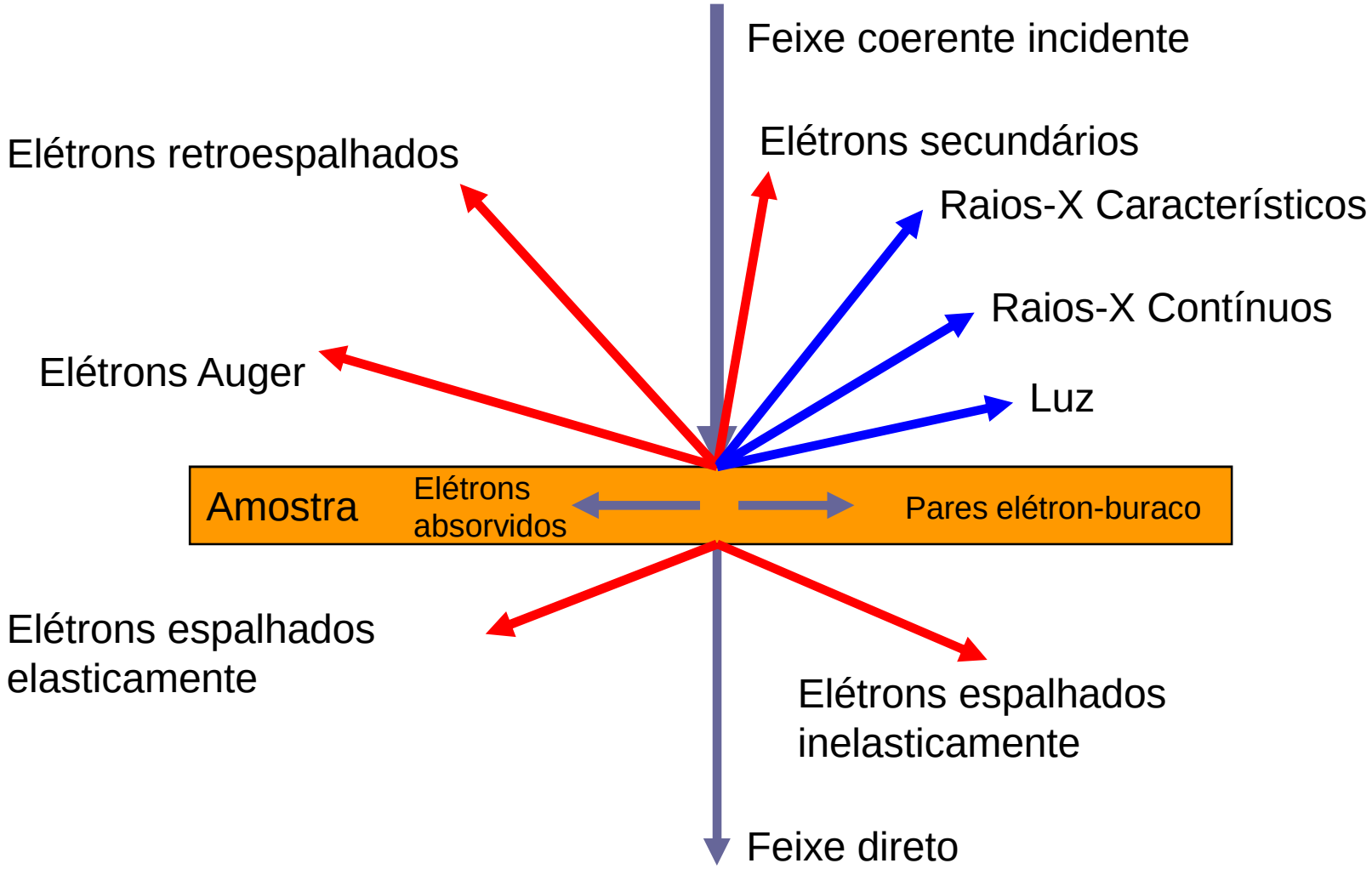
Aspecto interno e externo de uma lente magnética



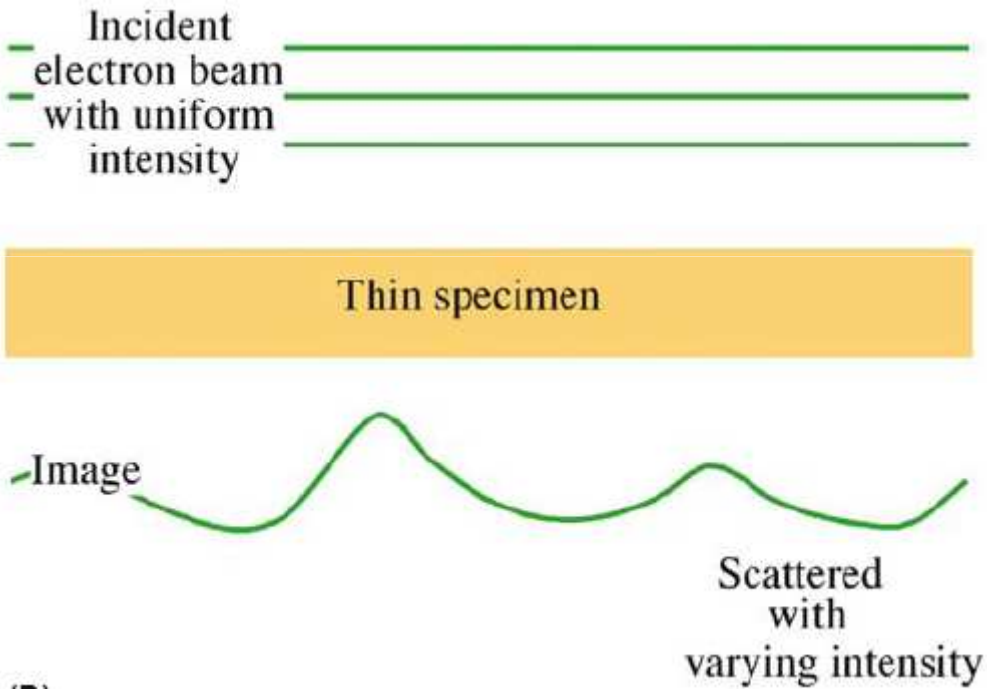


Williams e Carter, 2009

Interação Elétron-Amostra

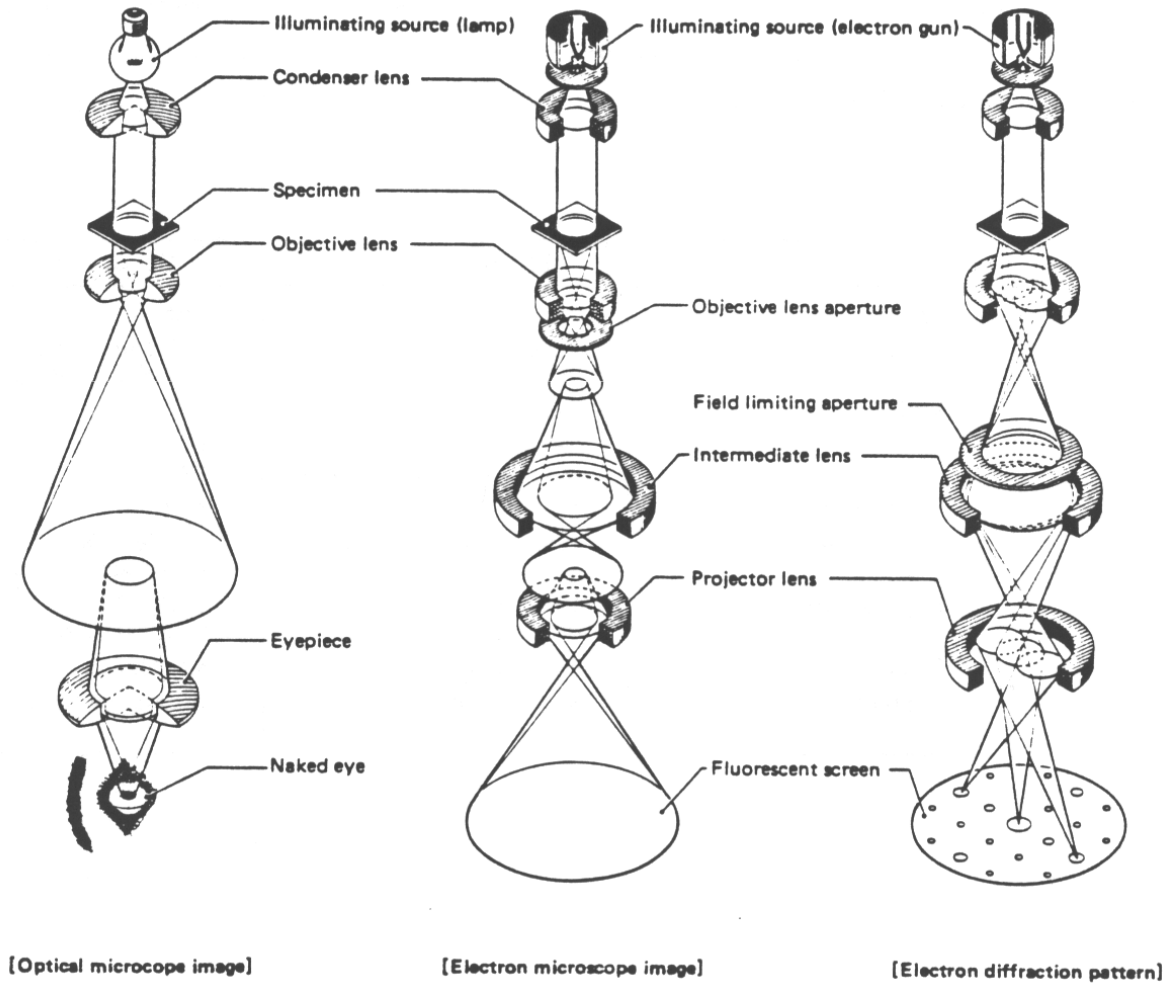


Interação Elétron-Amostra



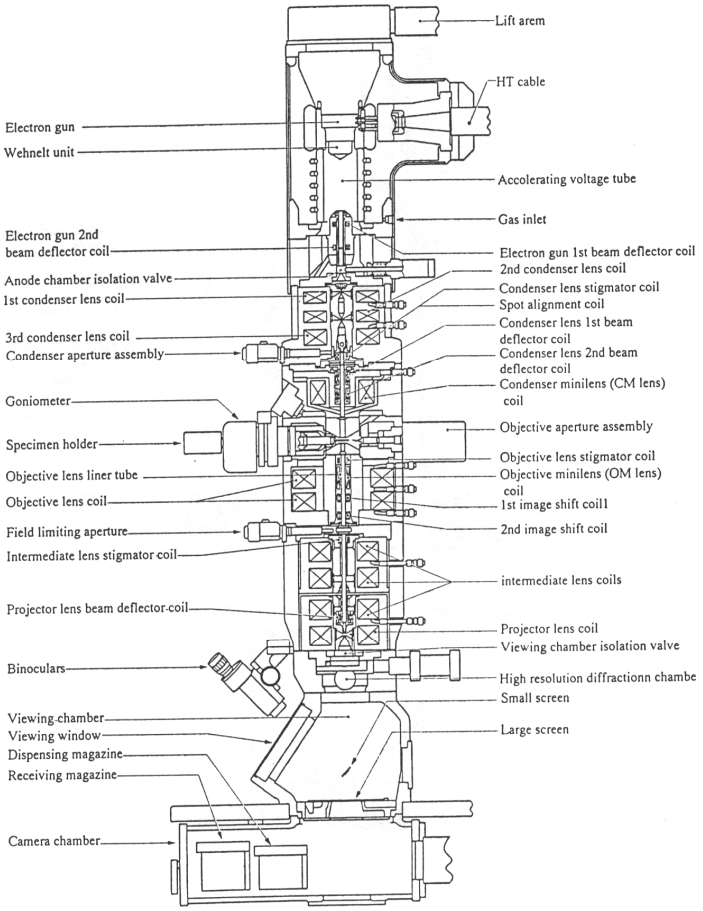
Williams e Carter, 2009

Arquitetura de um MET



Jeol

Um MET Moderno



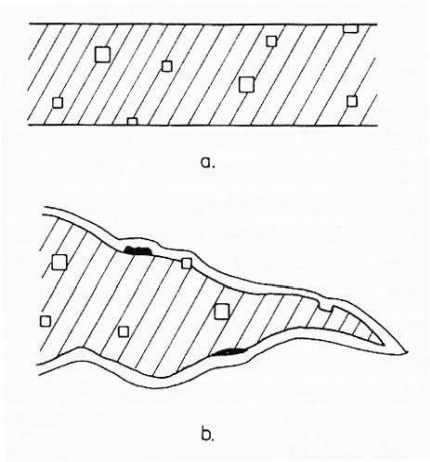


Jeol

Amostras para MET

Suposição de um só evento de espalhamento

Espessura < 100 ηm

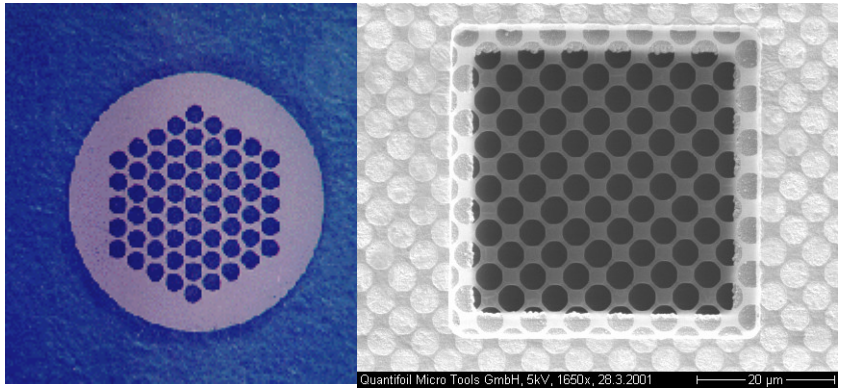


Pergunta básica:

- **Amostra de Folha Fina**

  ou

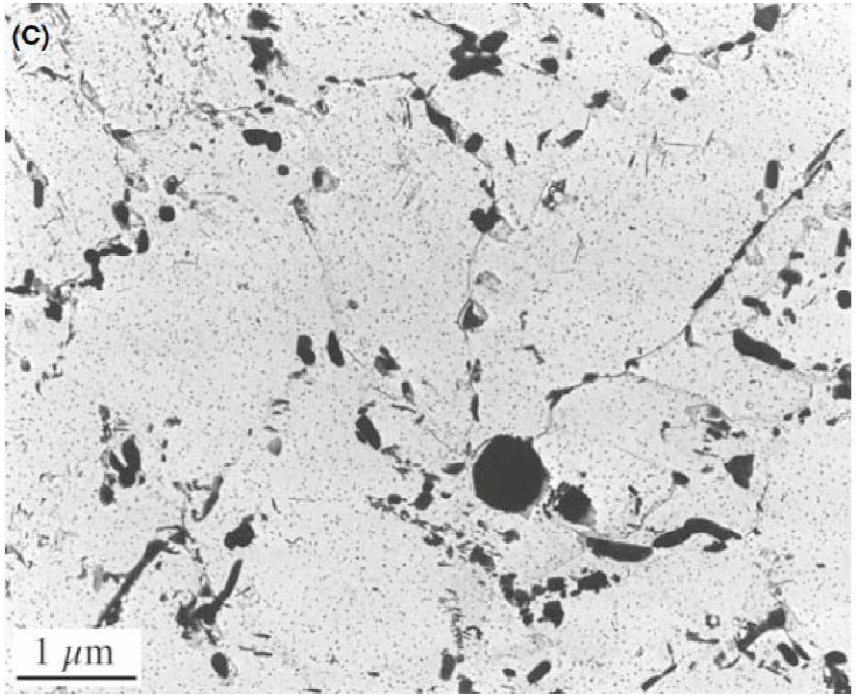
- **Grade**



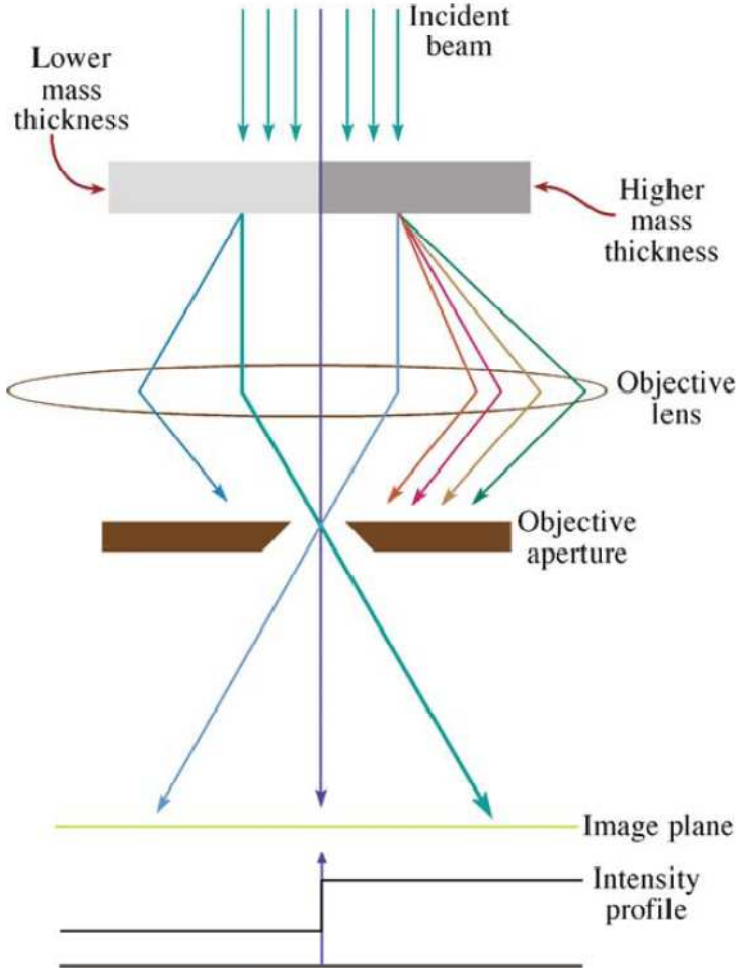
SPI

Contraste de Massa-Espessura

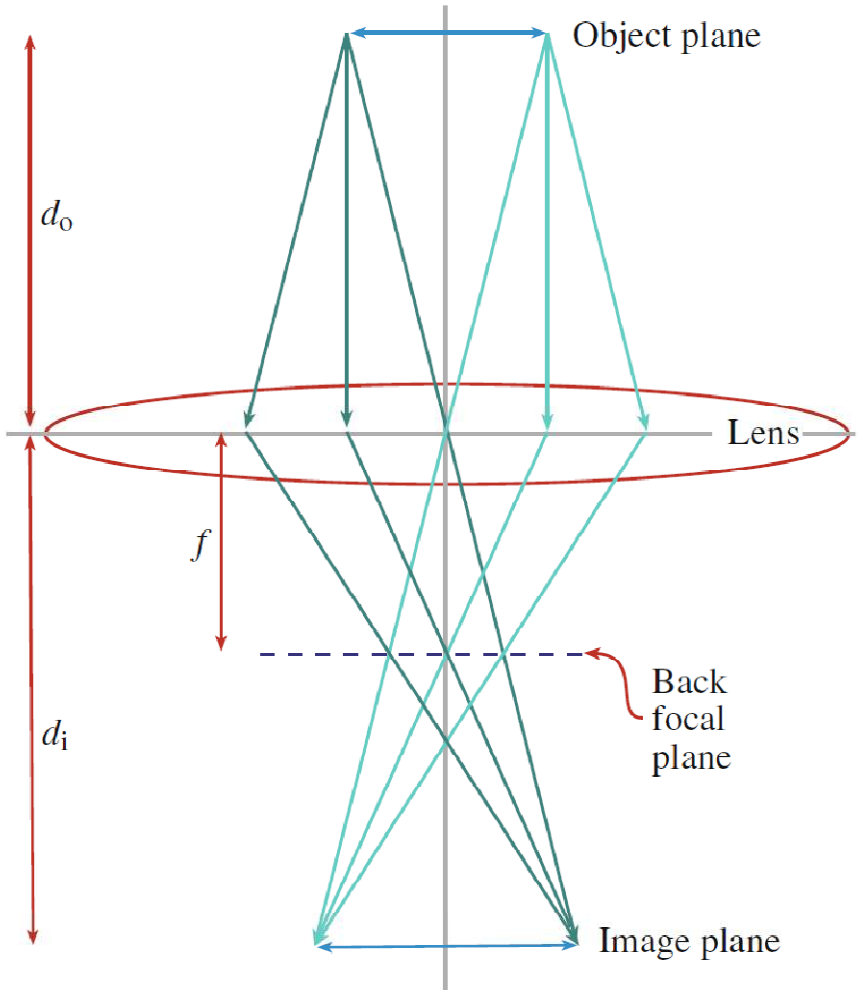
Precipitados em aço CrMo



Williams e Carter, 2009



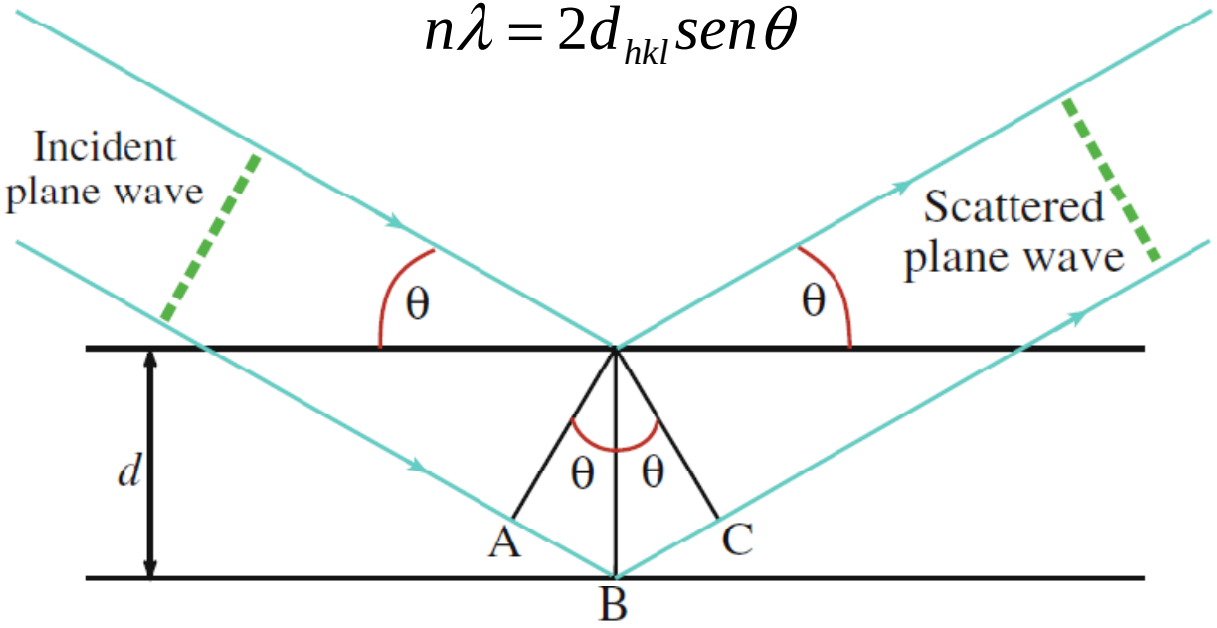
A Lente Objetiva



Williams e Carter, 2009

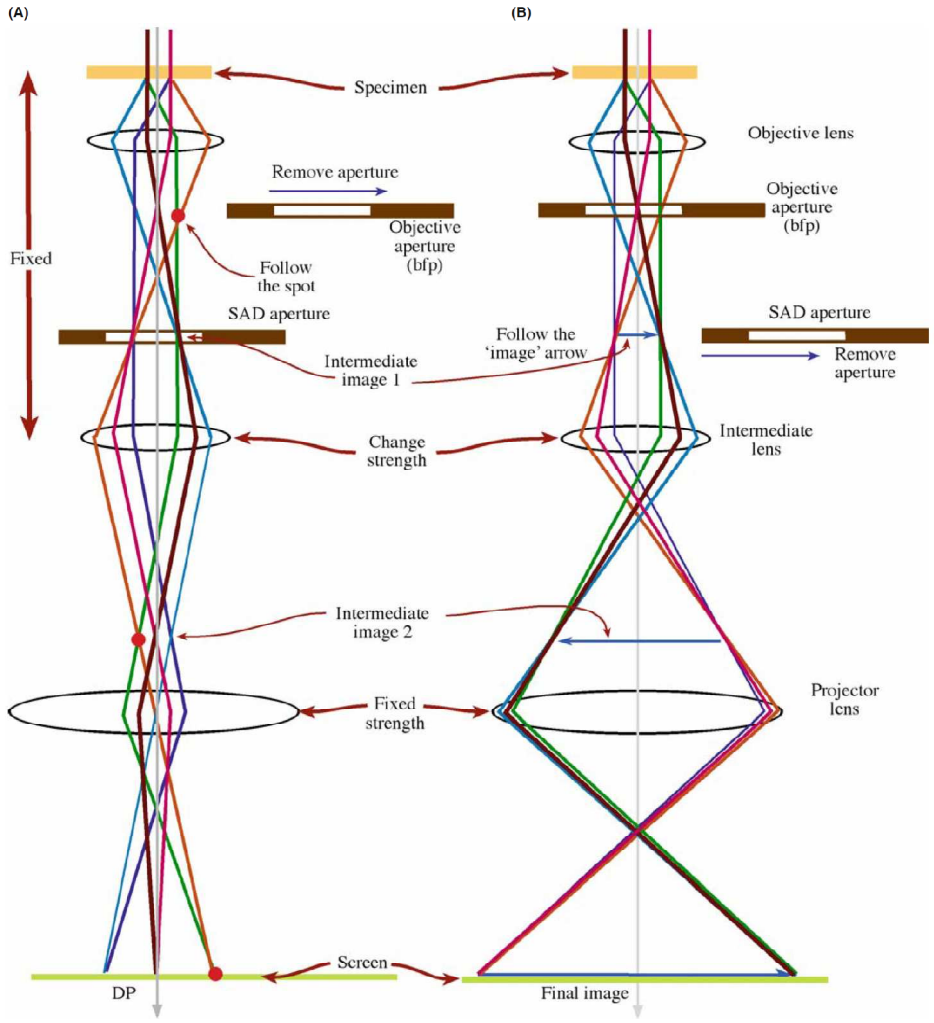
Condição de Bragg

$$n\lambda = 2d_{hkl} sen\theta$$



Williams e Carter, 2009

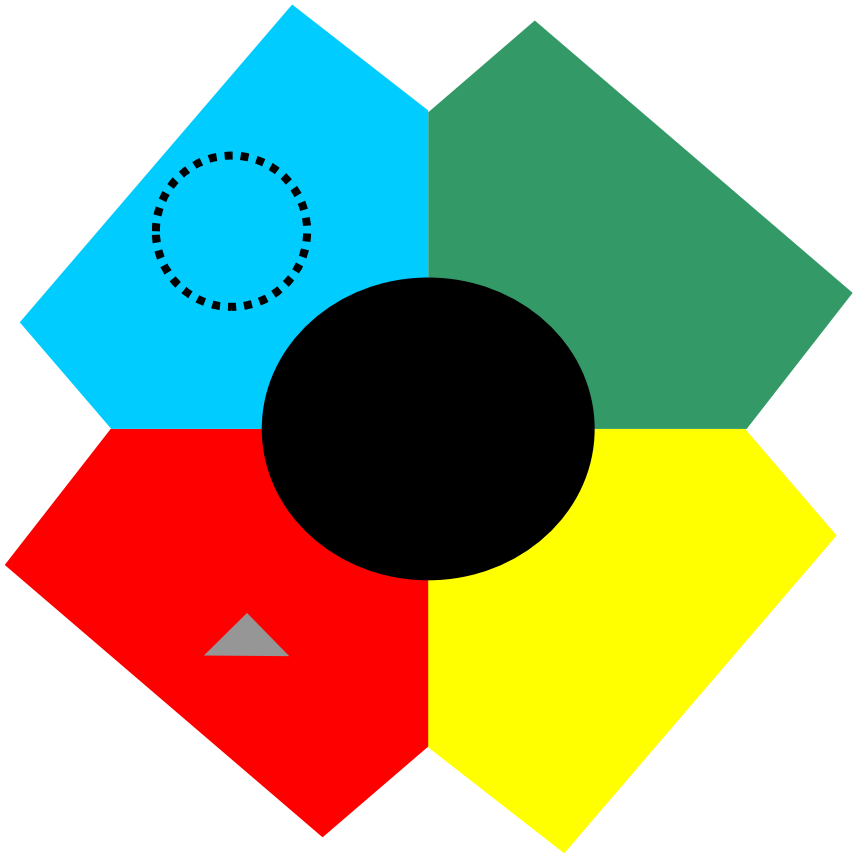
Amostras Cristalinas



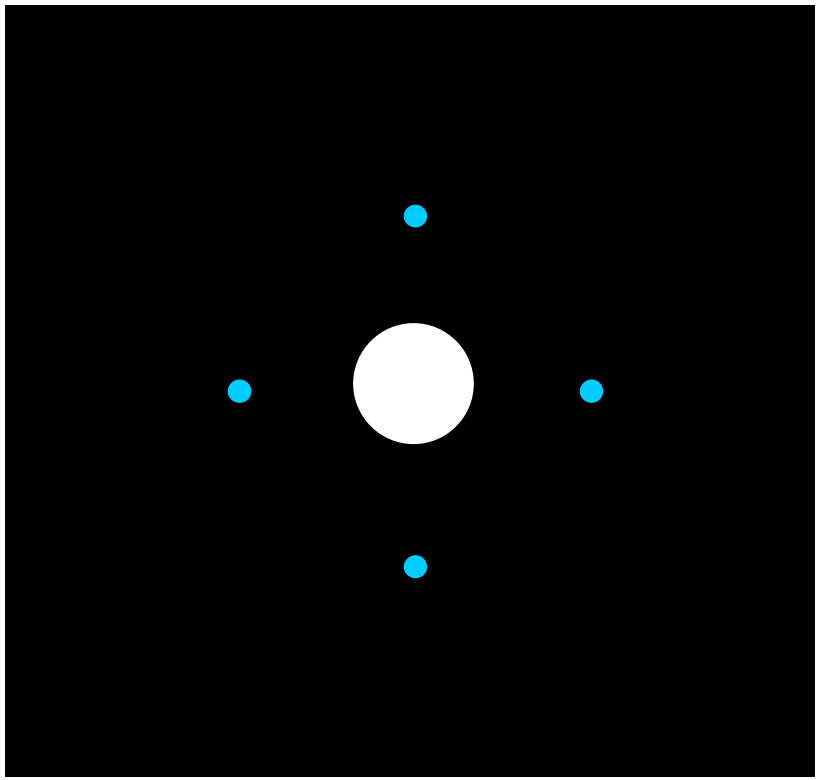
A figura de difração e a formação de imagem.

Williams e Carter, 2009

Experimento Mental

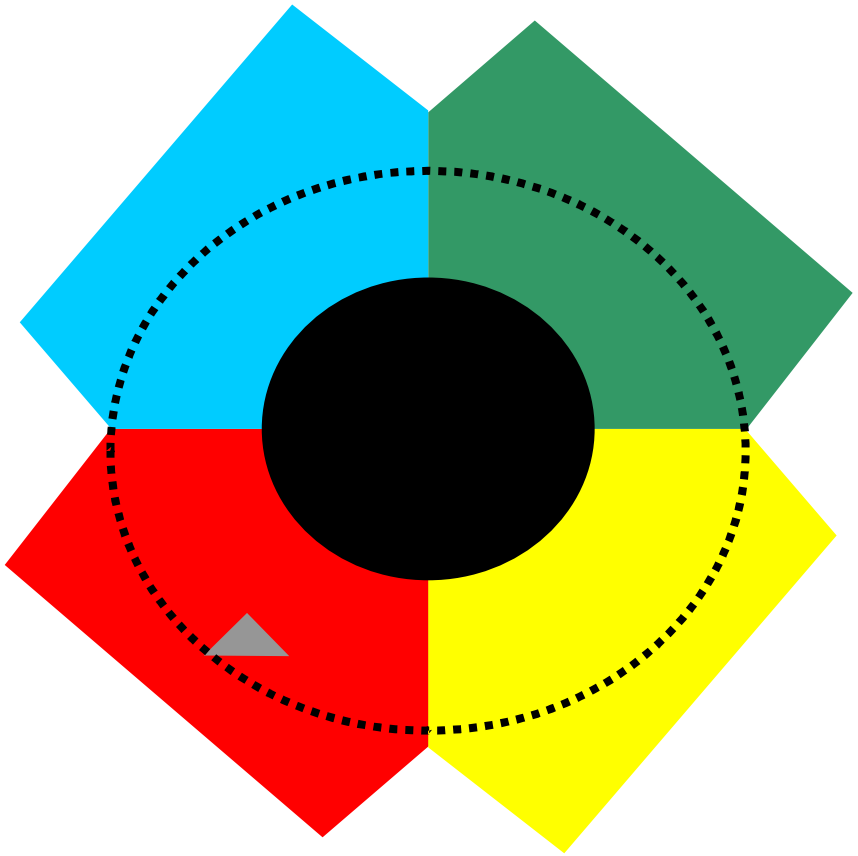


Plano Imagem

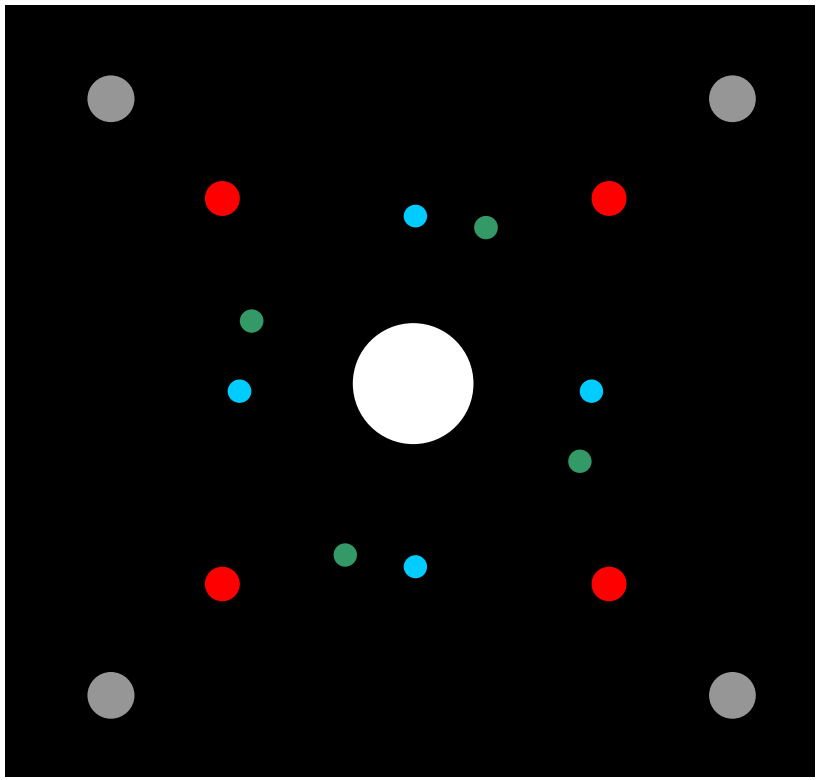


Plano Focal

Experimento Mental

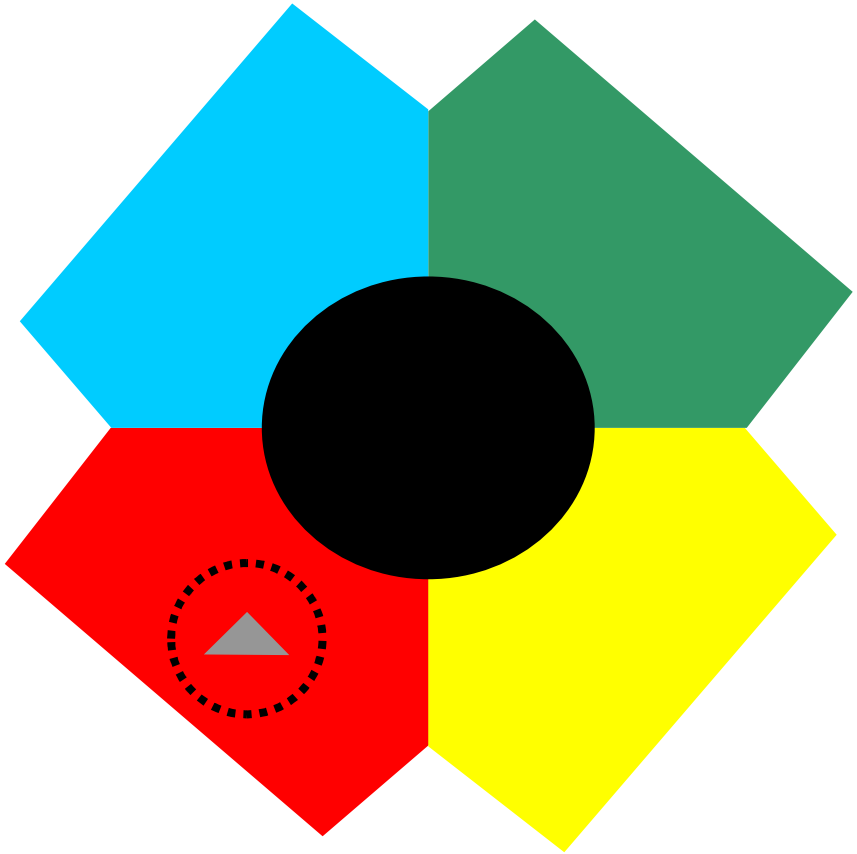


Plano Imagem

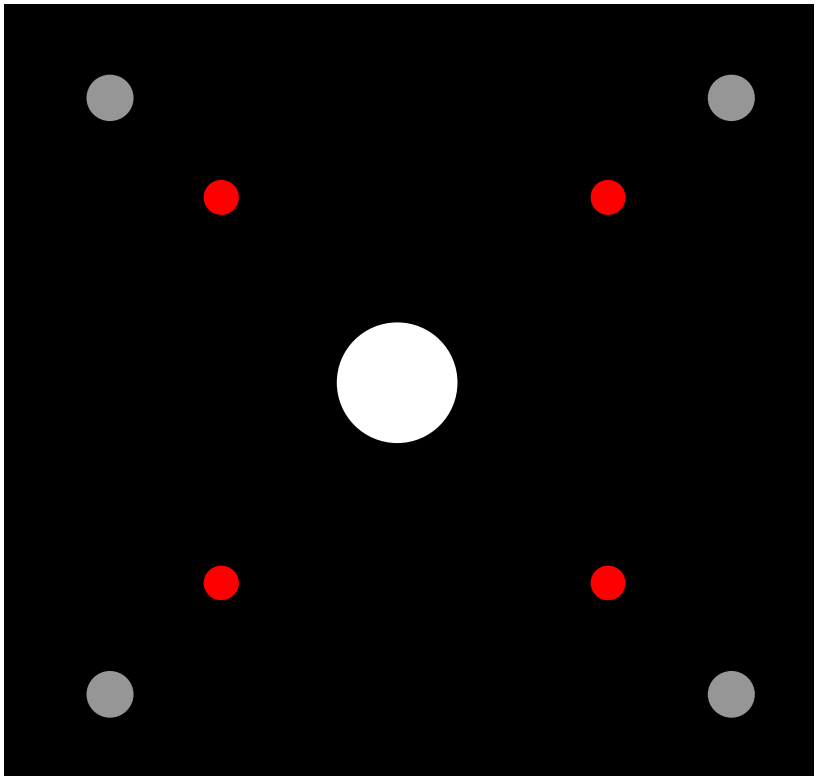


Plano Focal

Experimento Mental

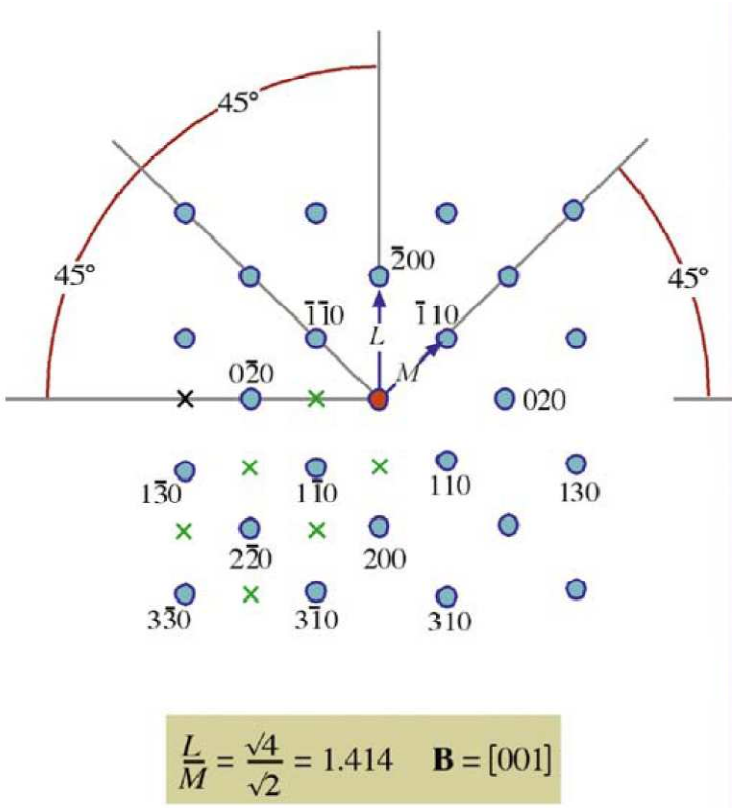


Plano Imagem



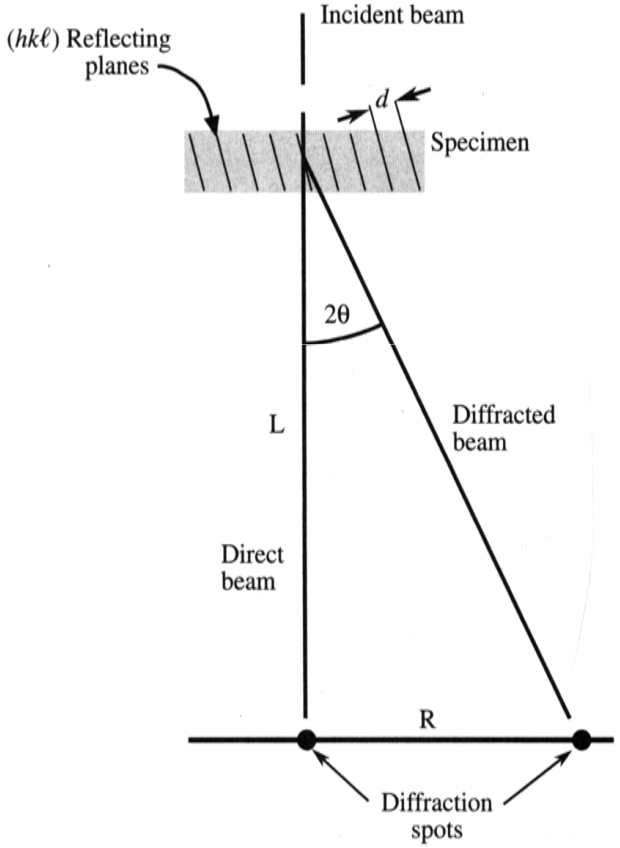
Plano Focal

Identificação da Figura de Difração



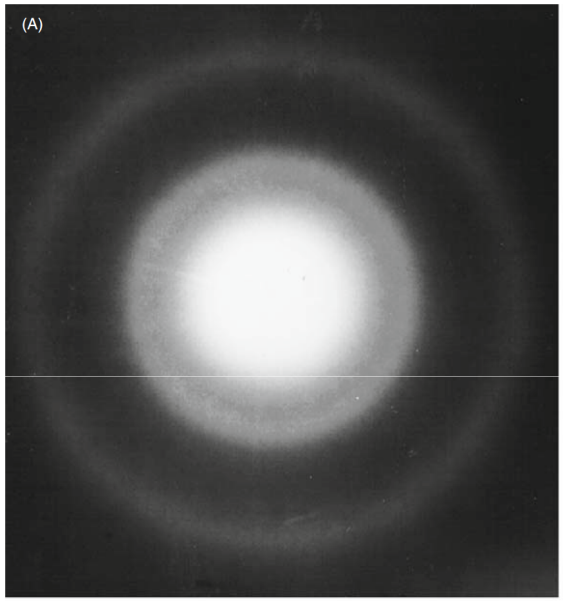
$$\frac{L}{M} = \frac{\sqrt{4}}{\sqrt{2}} = 1.414 \qquad \mathbf{B} = [001]$$

$$Rd = L\lambda$$

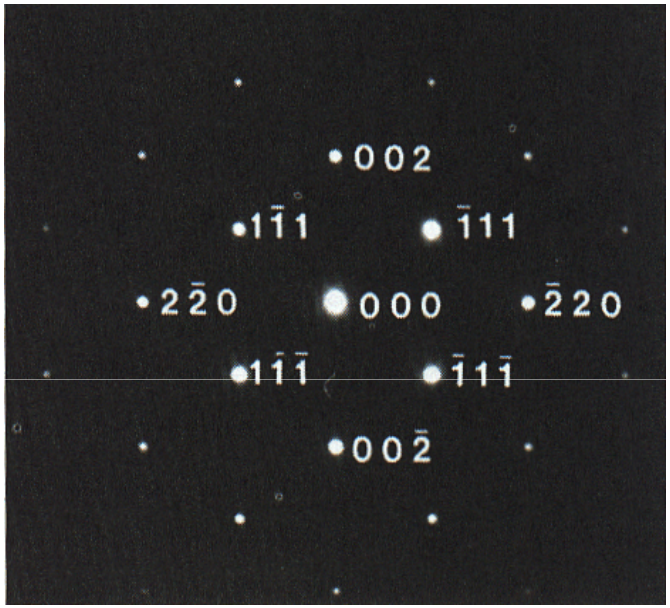


Williams e Carter, 2009

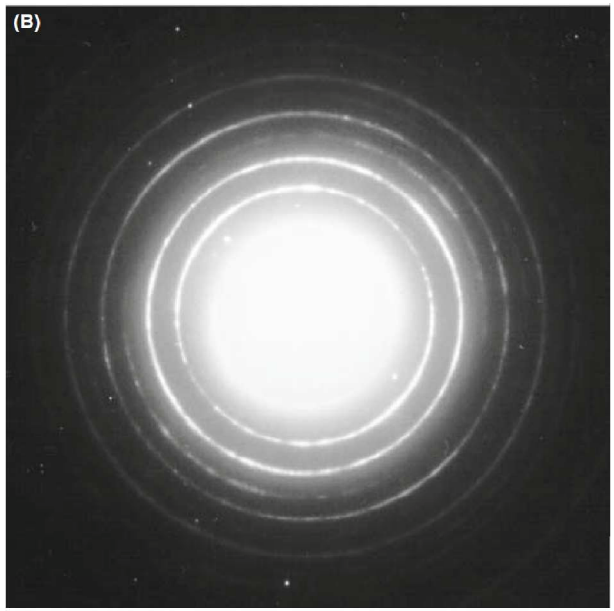
Figura de Difração



Carbono amorfo



Monocristal

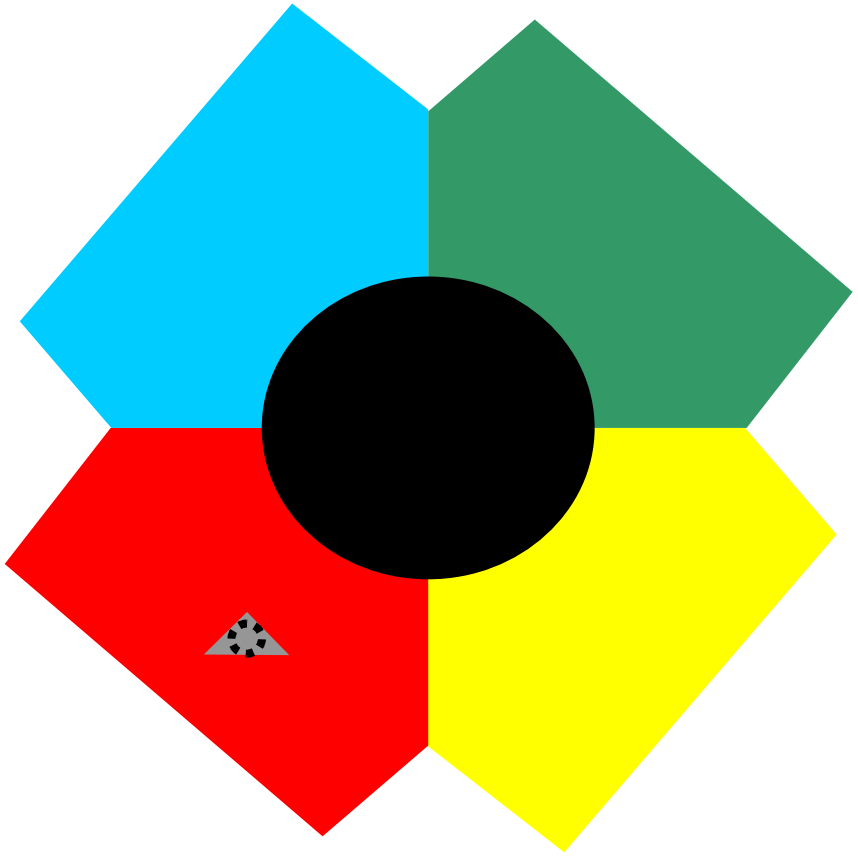


Região policristalina

Williams e Carter, 2009

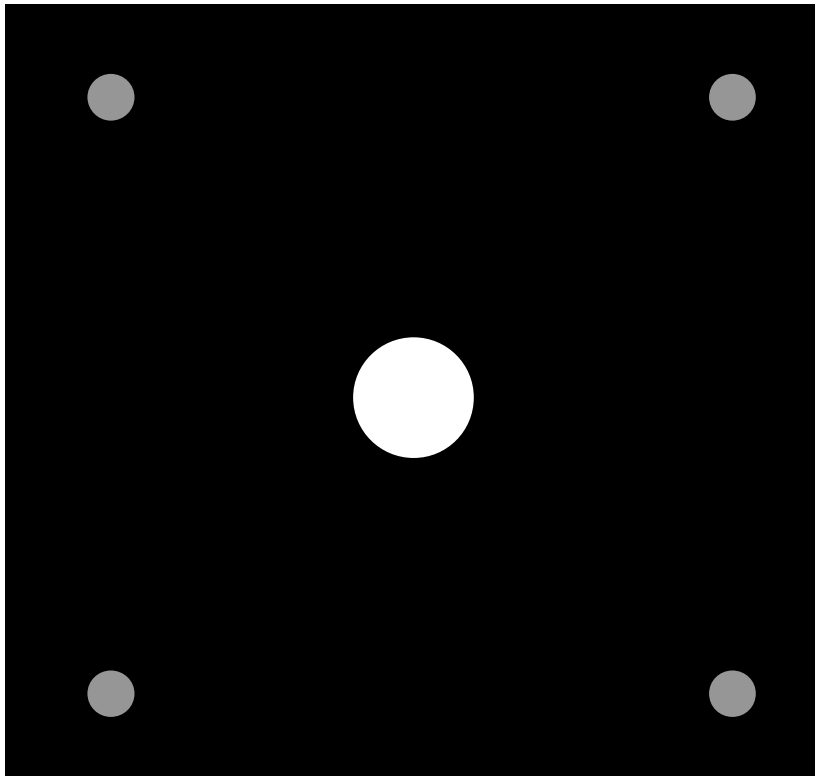
Resolução Espacial

Abertura SAD no plano Imagem
Aumento de aprox. 25x (M)



Plano da Amostra

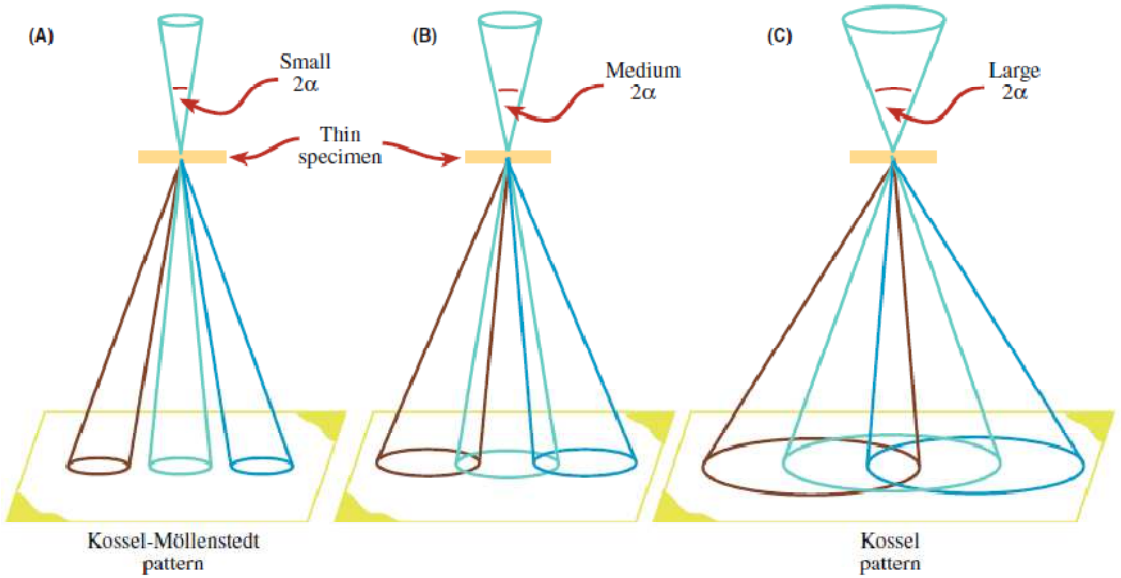
Menor abertura ~ 10 μm
Resolução ~0,5 μm

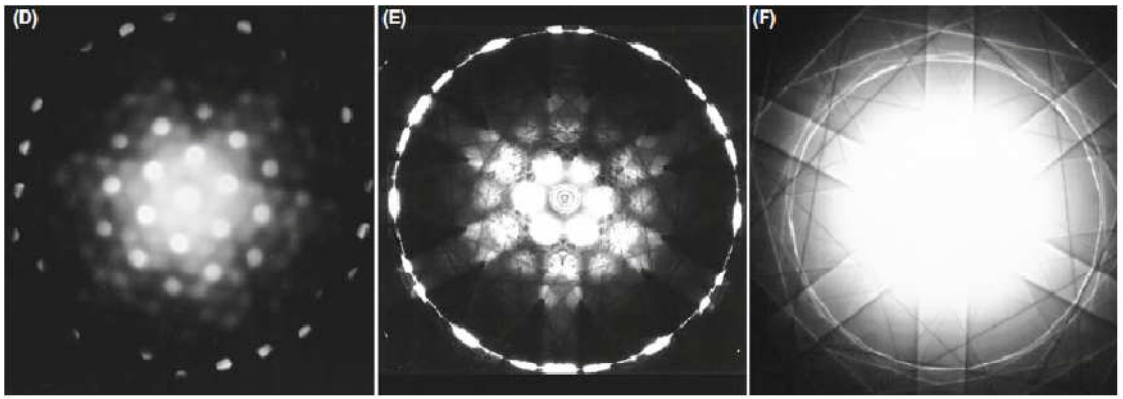


Plano Focal

Feixe Convergente

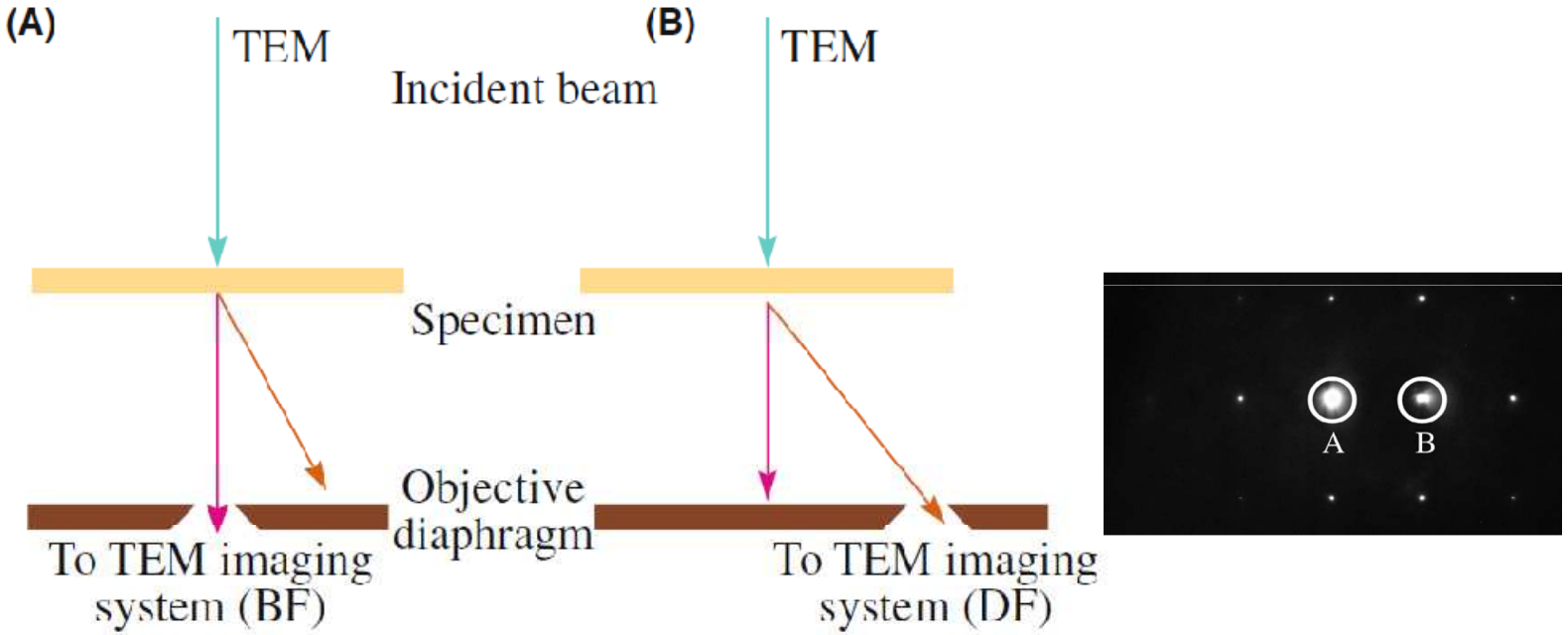
Variação do ângulo de convergência





Williams e Carter, 2009

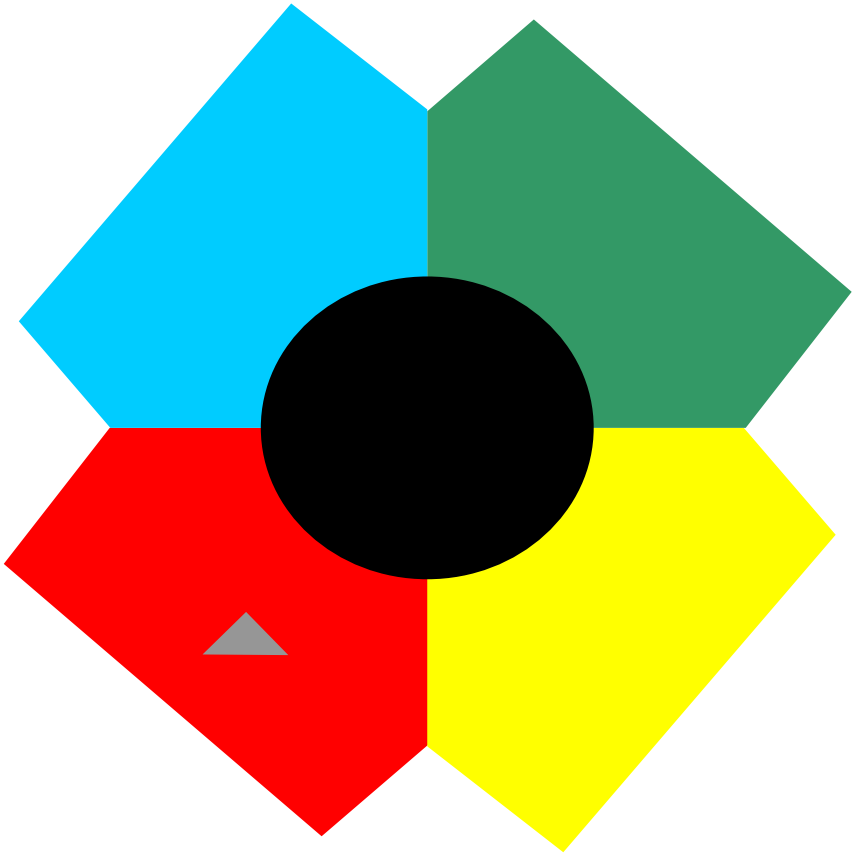
Campo Claro e Campo Escuro



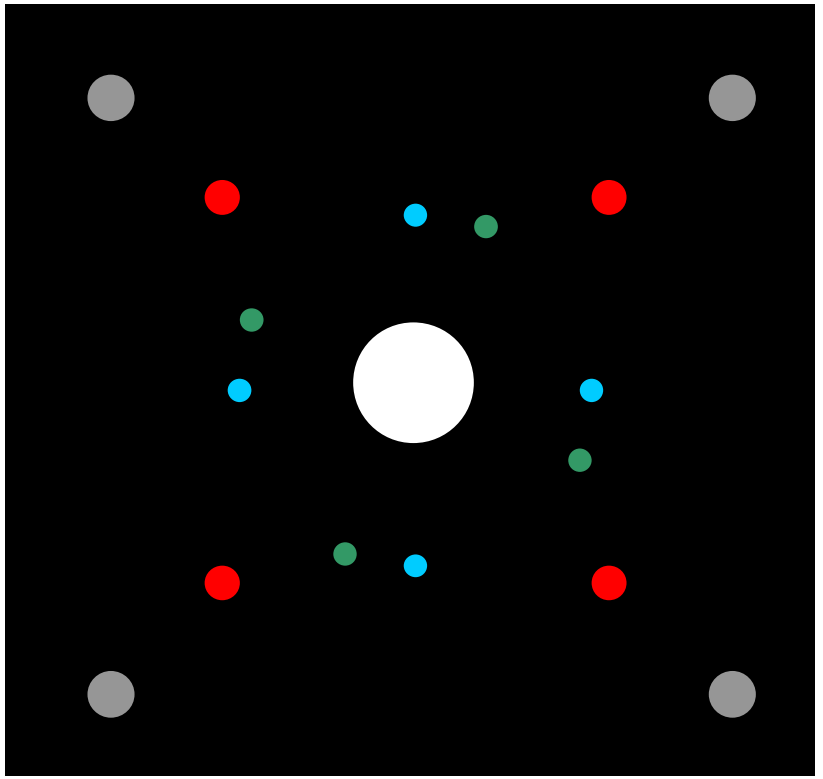
Campo Claro: Toda imagem que inclui o feixe direto
Campo Escuro: Toda imagem que deixa de incluir o feixe direto

Williams e Carter, 2009

Experimento Mental

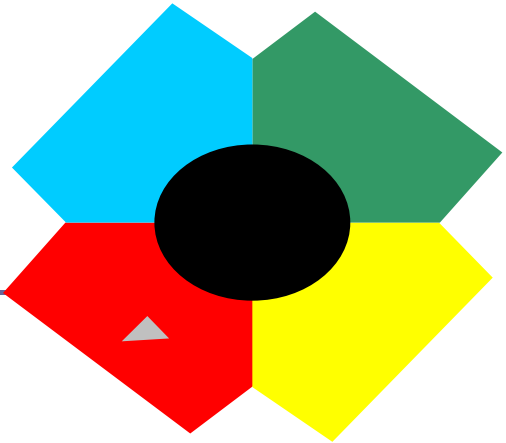


Plano da Amostra

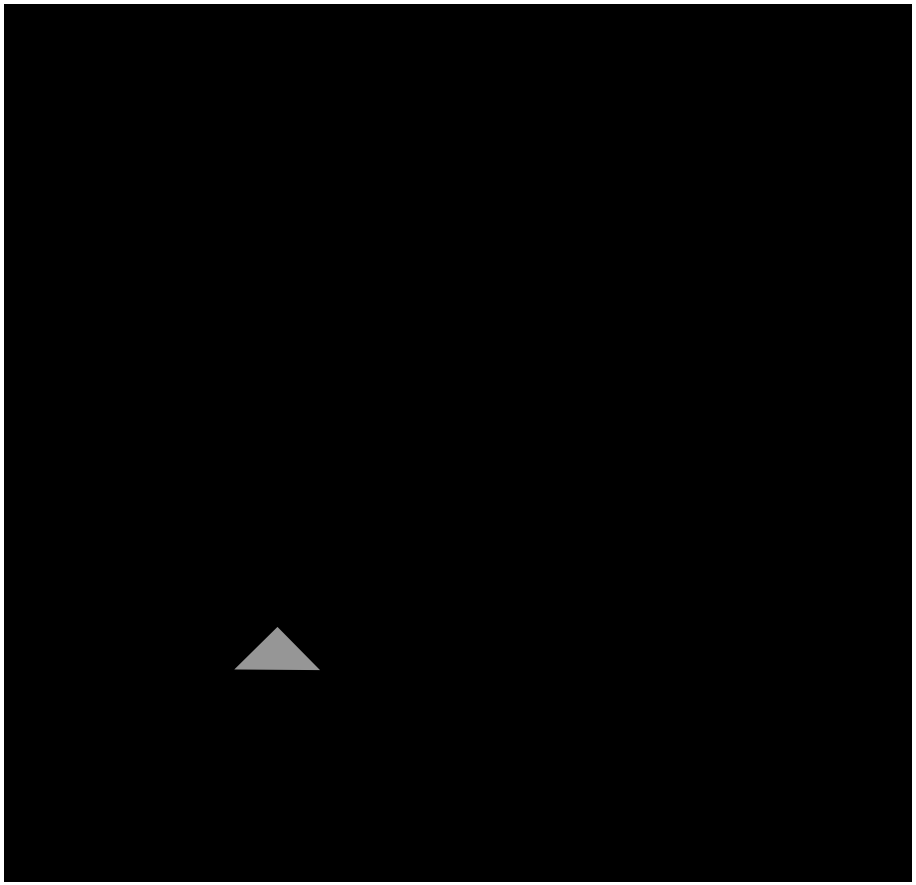


Plano Focal

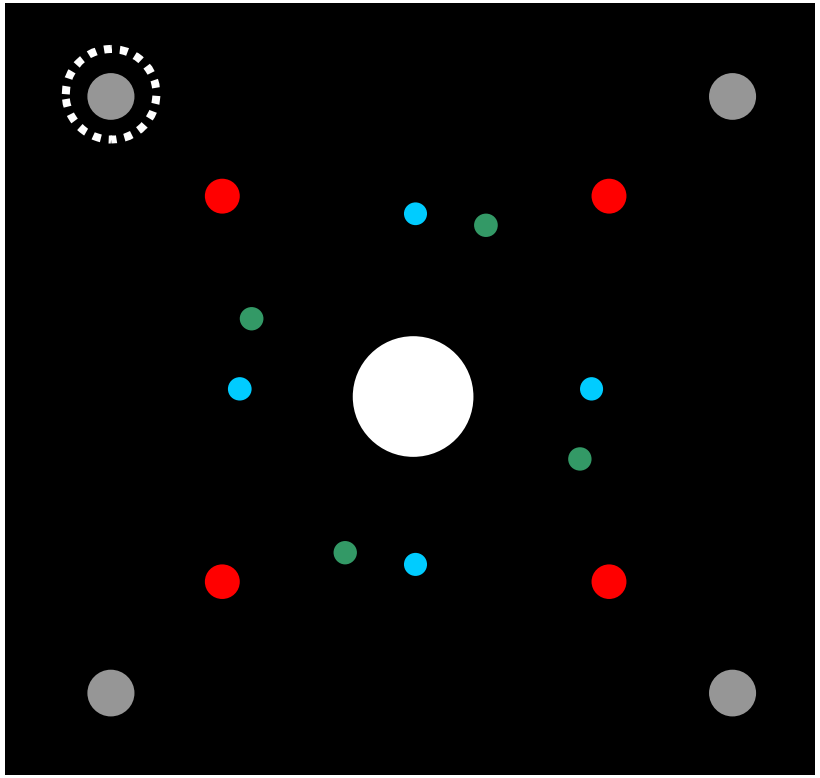
Experimento Mental
Campo Escuro



Plano da Amostra

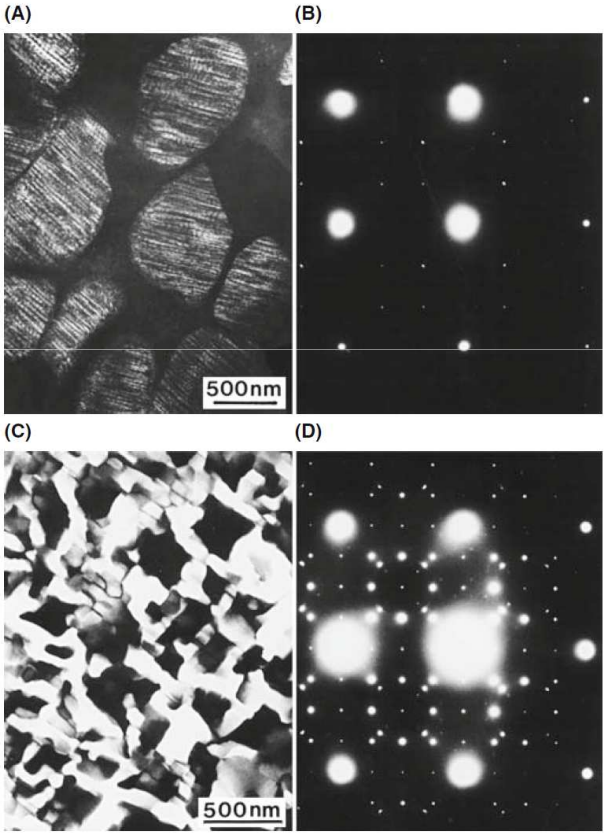


Plano Imagem

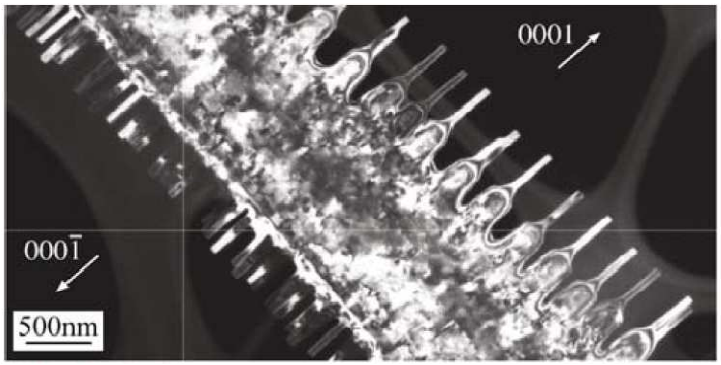


Plano Focal

Campo Escuro



Precipitado V_6C_5 e seu padrão de difração.



Nanoestrutura de ZnO

Precipitado V_8C_7 e seu padrão de difração.

Williams e Carter, 2009

Nanocristais

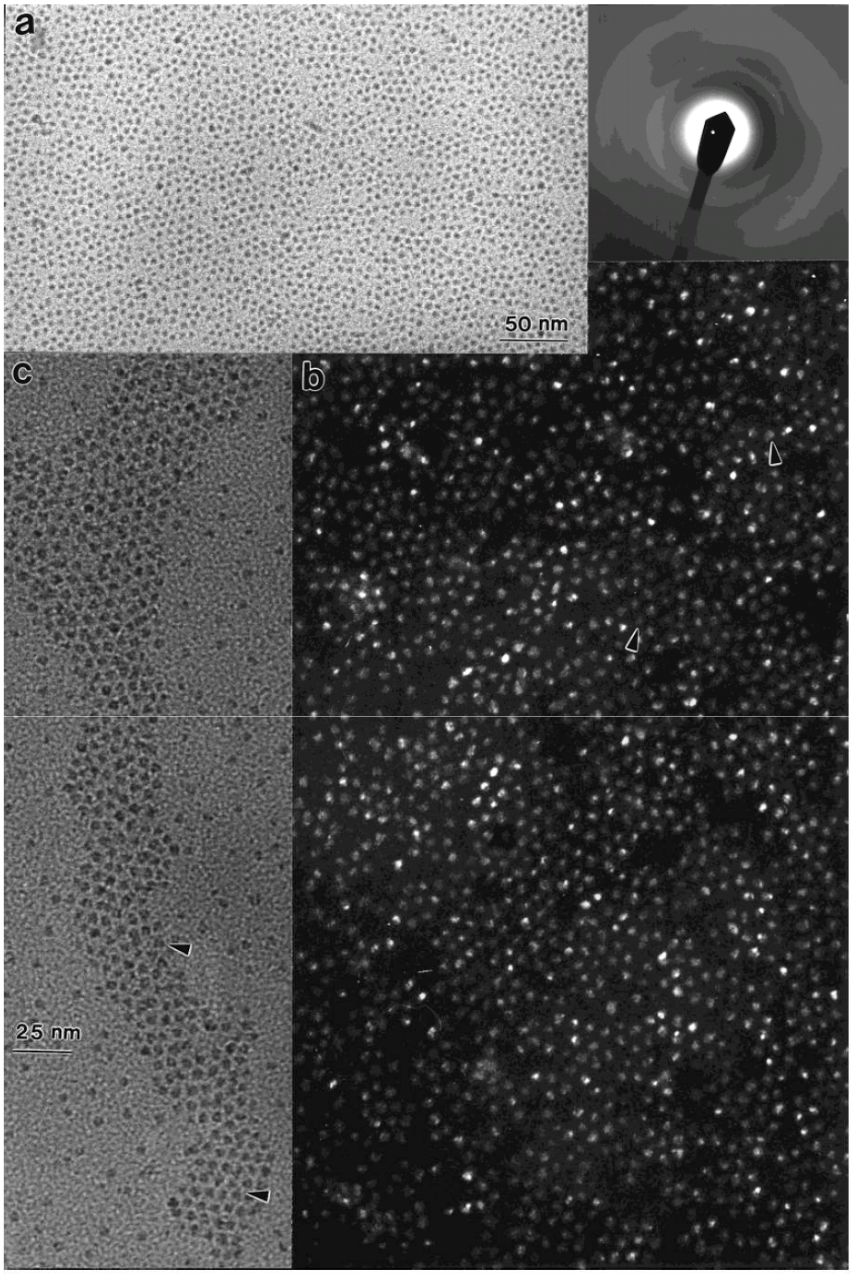


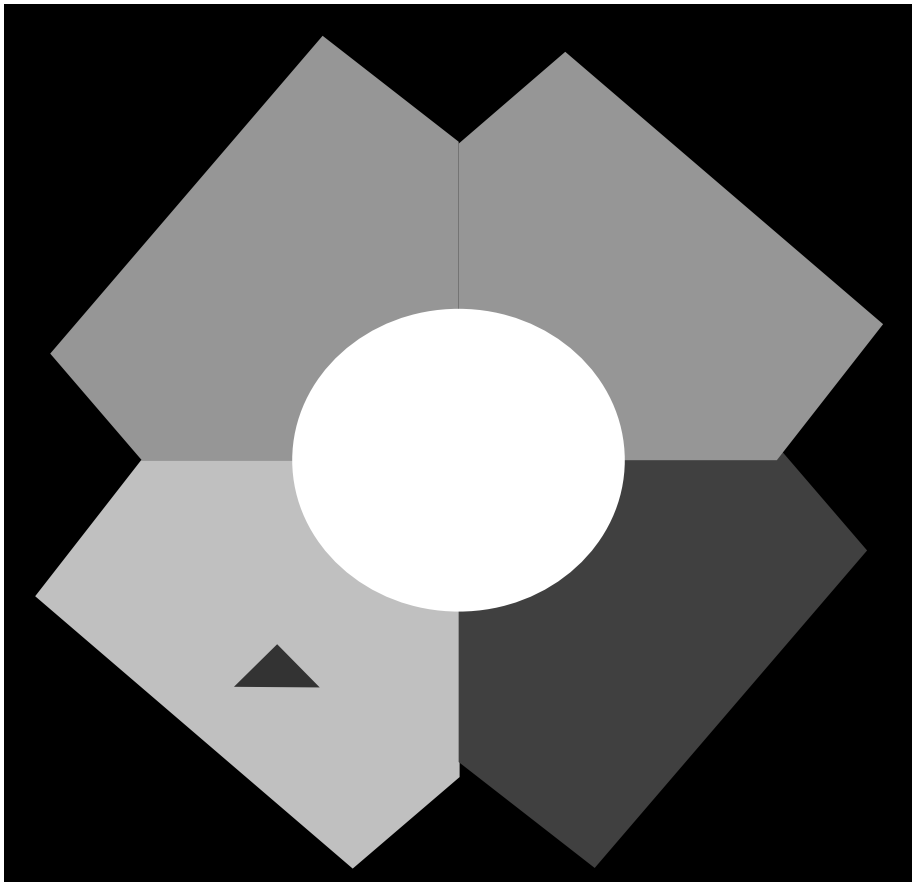
Figure 16. (a, c) Bright-field and (b) dark-field TEM images of monolayer self-assembly of tetrahedral CoO nanocrystals of ~4 nm in size, displaying short-range translational ordering but no orientational order. An electron diffraction pattern from the nanocrystals is shown in the inset, exhibiting broadened rings.

J. Phys. Chem. B, Vol. 104, No. 6, 2000

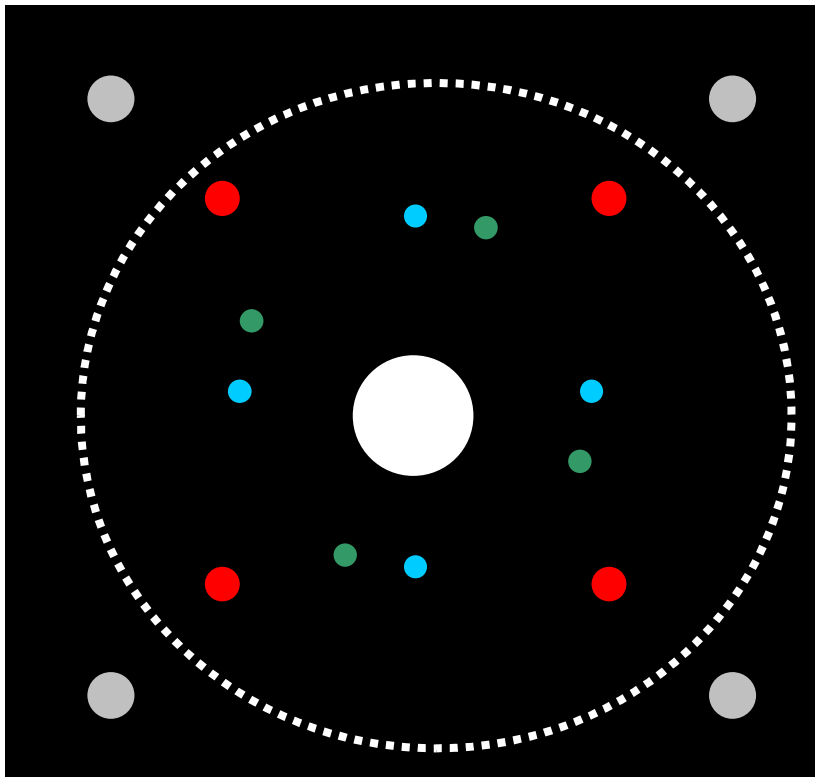
Experimento Mental
Contraste de Difração



Plano da Amostra

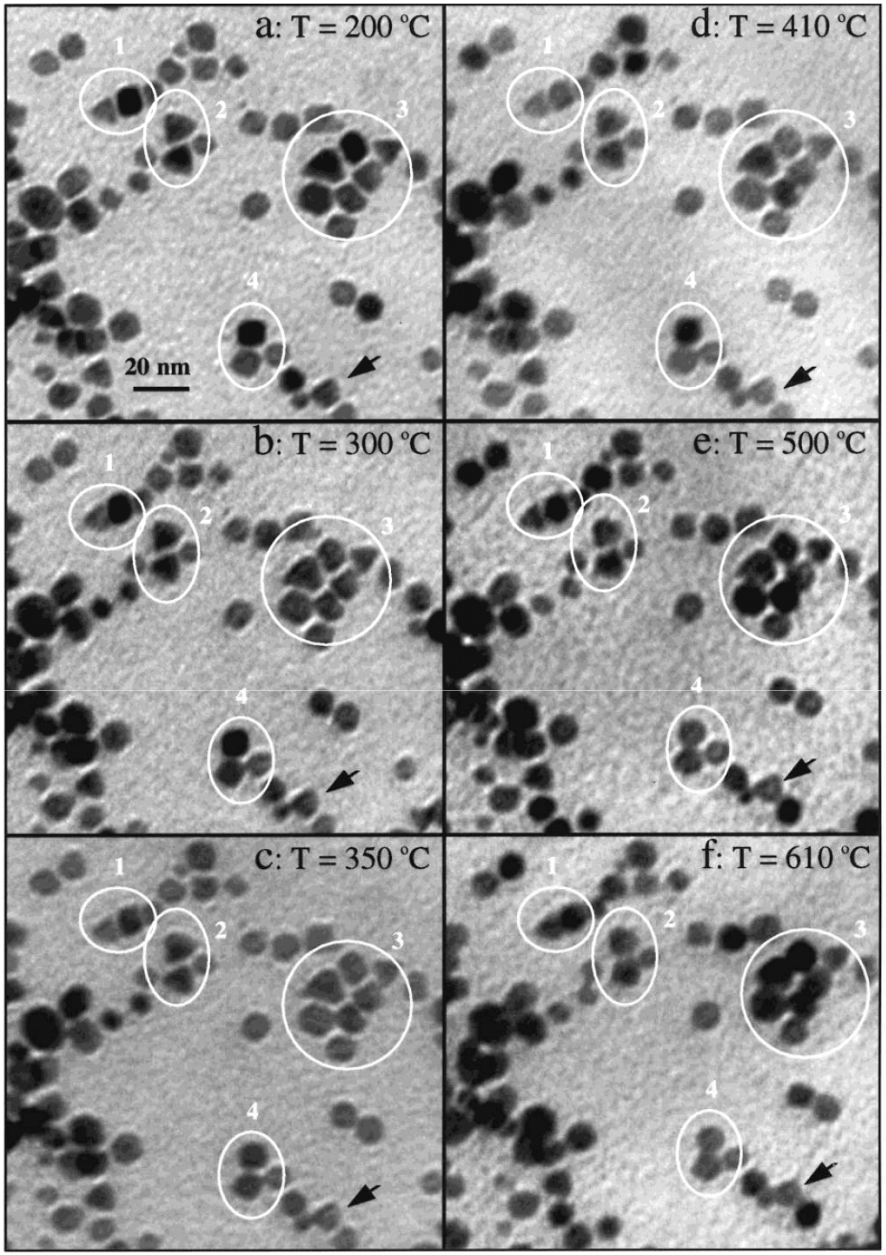


Plano Imagem



Plano Focal

Nanocristais



J. Phys. Chem. B, Vol. 104, No. 6, 2000

Figure 19. A series of TEM images recorded in situ from Pt nanocrystals dispersed on a carbon substrate and being heated to different temperatures, exhibiting the shape transformation as well as surface melting phenomenon of the particles at temperatures much lower than the melting point of the bulk (The Pt nanocrystals were supplied by J. Petroski and M. A. El-Sayed).

Quantum Dots



FIG. 7. Cross-sectional TEM image showing InP SAQDs embedded in $In_{0.49}(Al_{0.6}Ga_{0.4})_{0.51}P$ layers grown at 650 °C for 7.5 MLs on a GaAs (100) substrate.

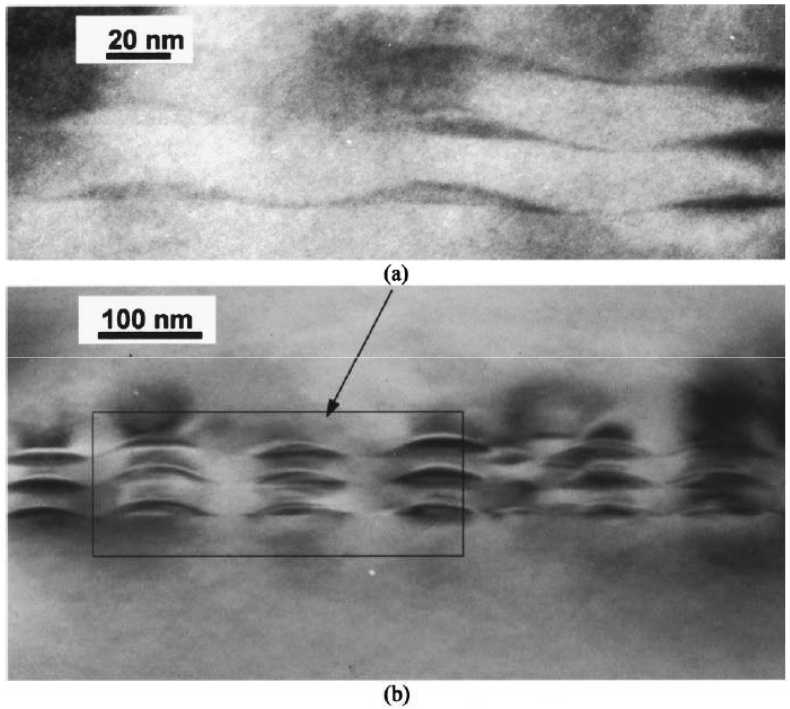
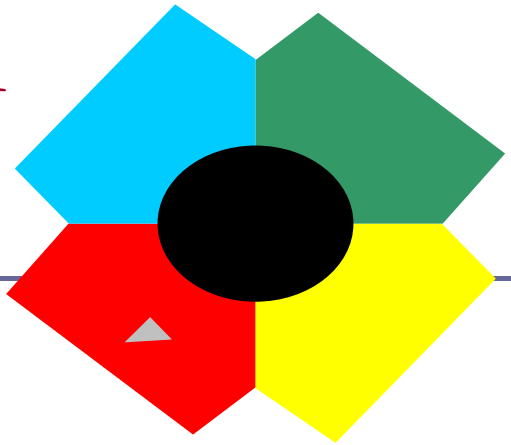


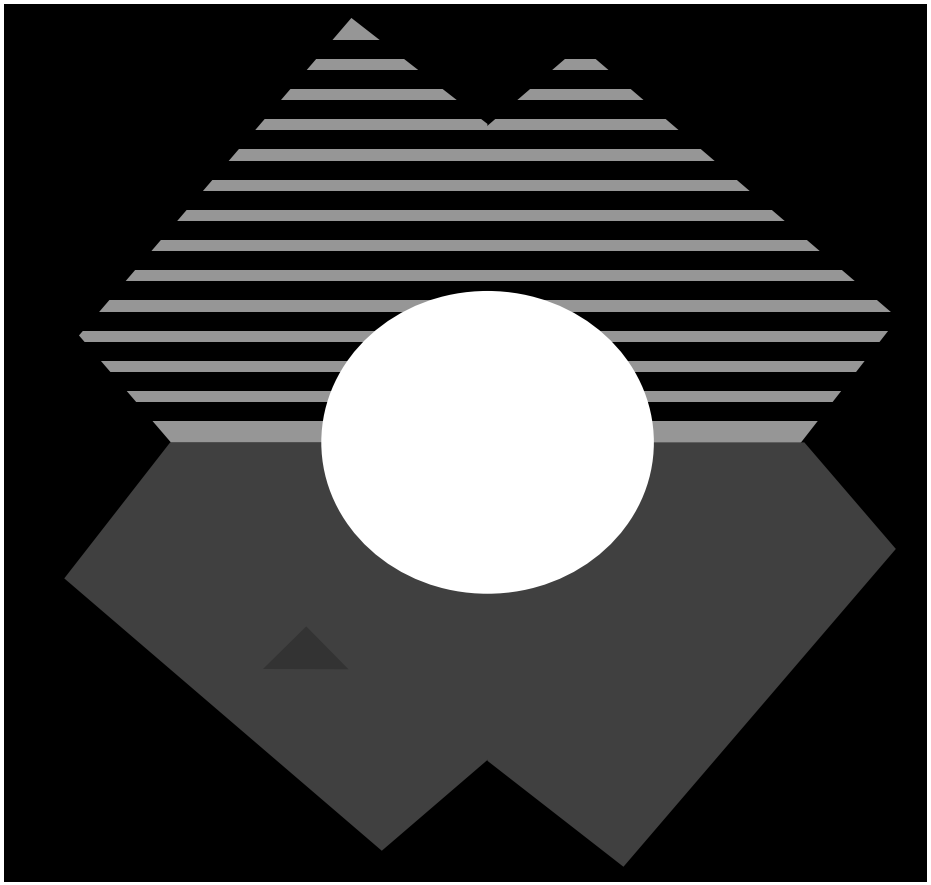
FIG. 8. Cross-sectional TEM image showing three-stacked InP SAQDs embedded in $In_{0.49}(Al_{0.6}Ga_{0.4})_{0.51}P$ layers.

Ryou *et al.* J. Appl. Phys., Vol. 91, No. 8, 15 April 2002

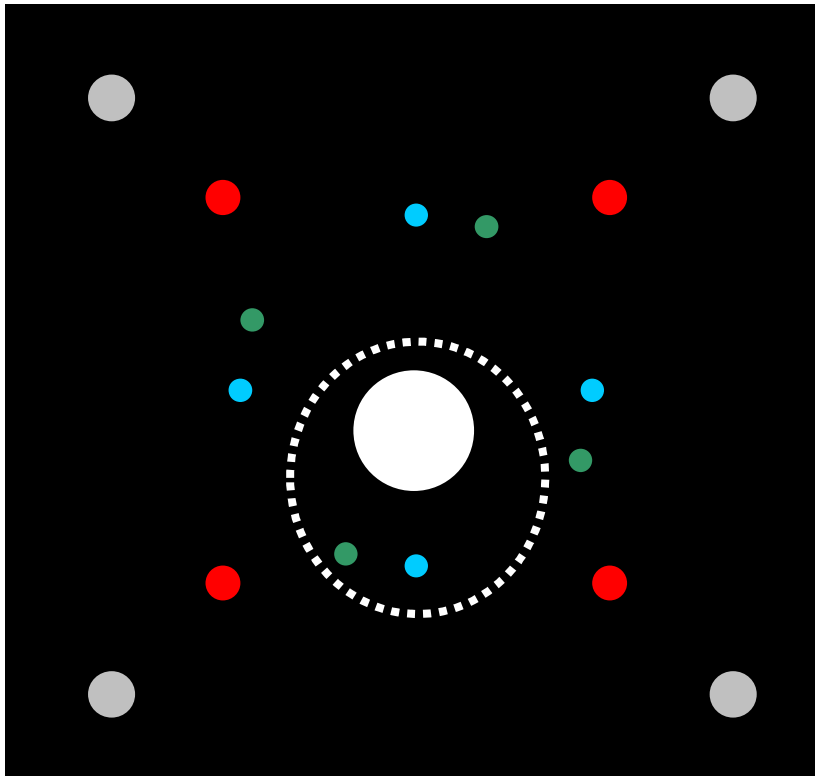
Experimento Mental
Contraste de Fase



Plano da Amostra

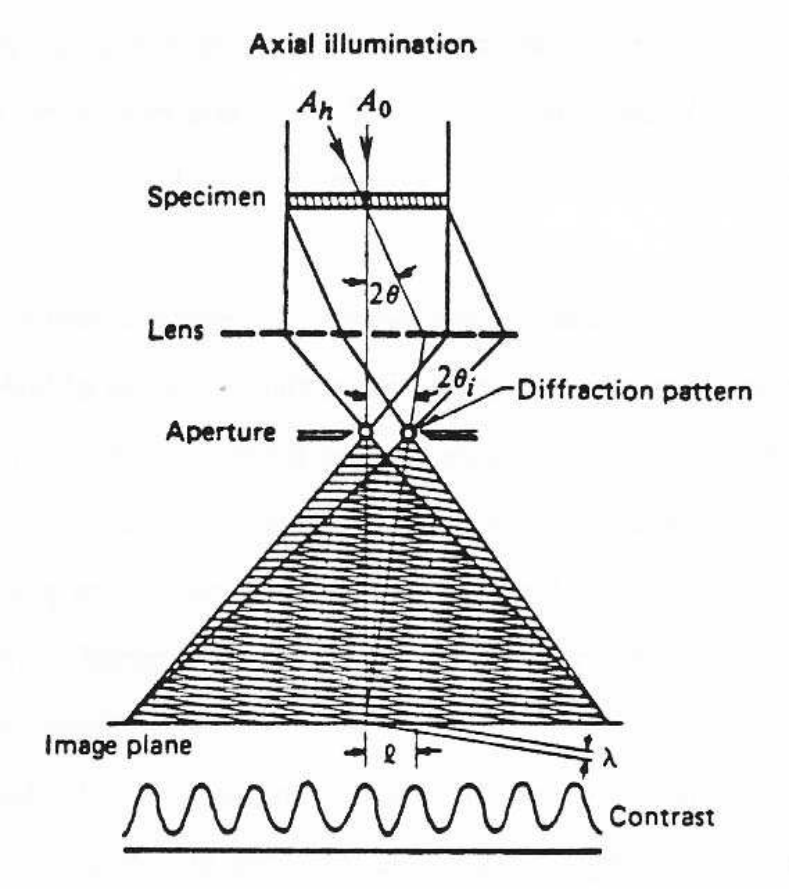


Plano Imagem



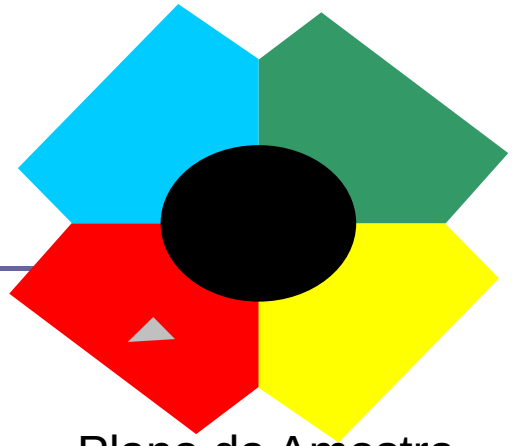
Plano Focal

Contraste de Fase

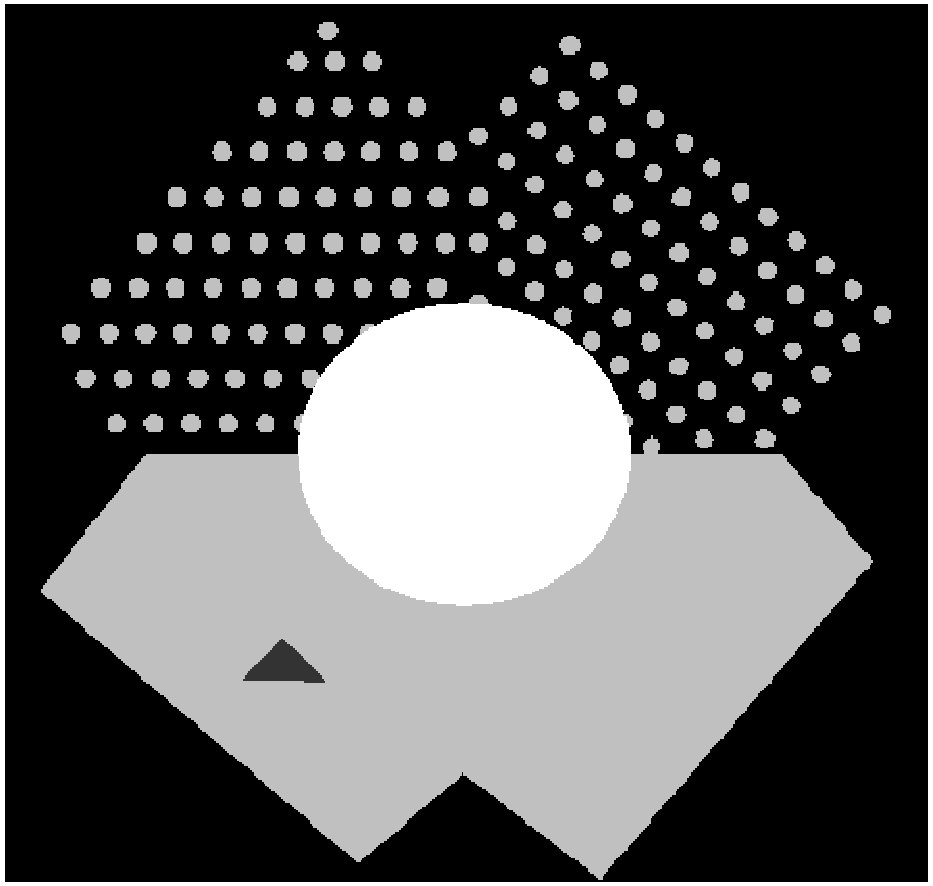


Jeol

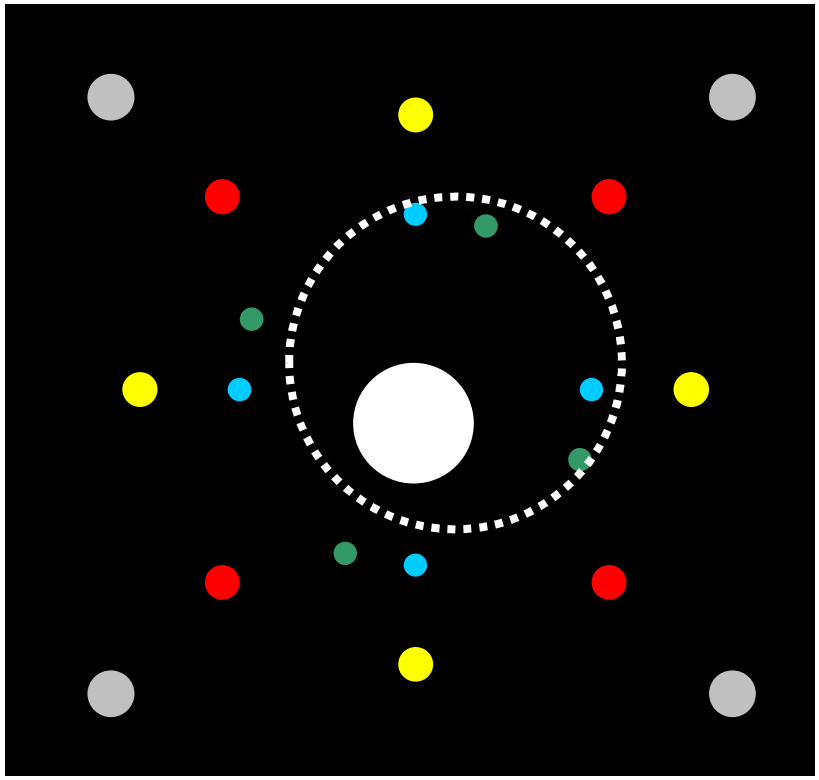
Experimento Mental
Contraste de Fase



Plano da Amostra

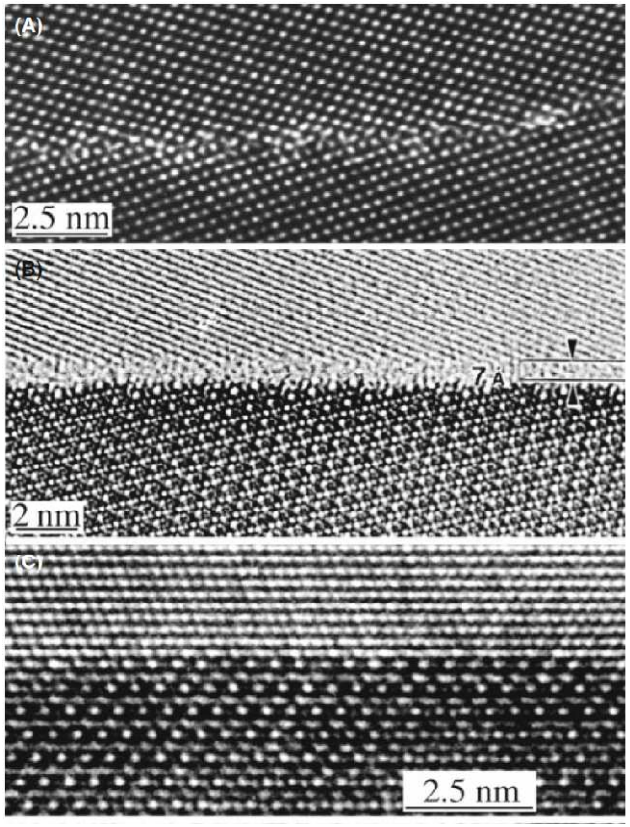


Plano Imagem



Plano Focal

HRTEM



CG em Ge

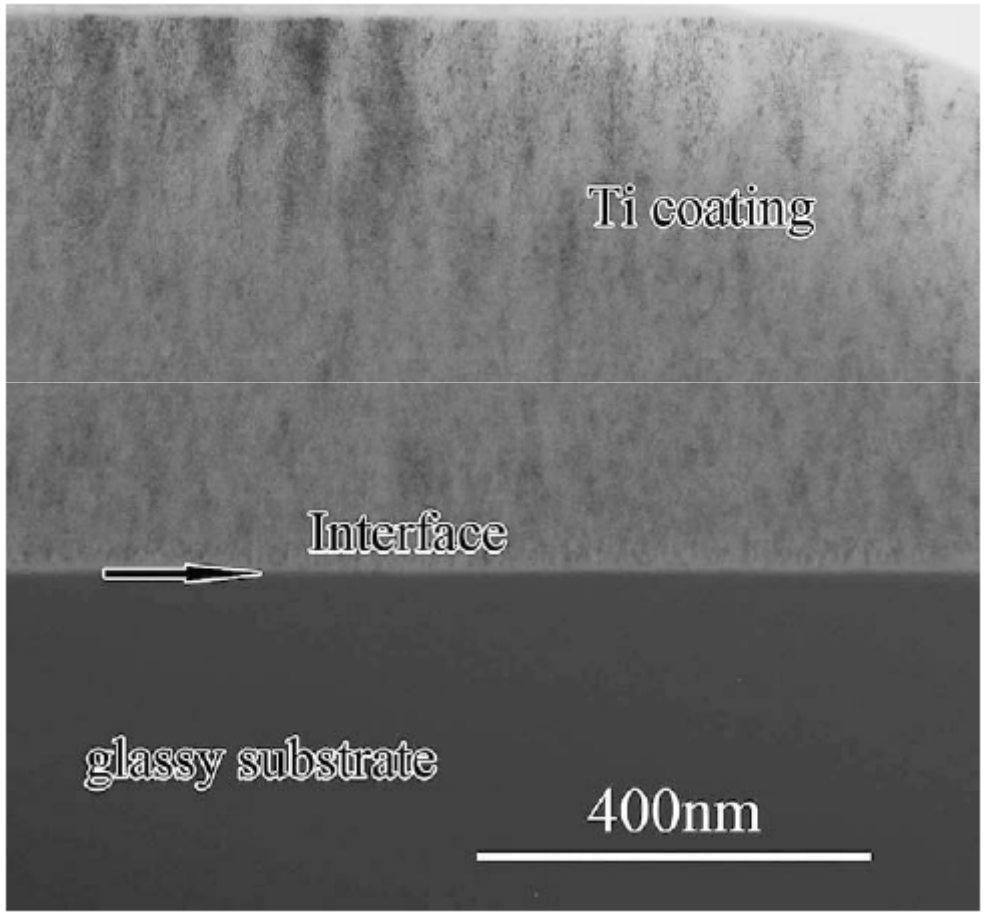
CG em Si_3N_4 com camada amorfa

Interface entre NiO e $NiAl_2O_4$

Williams e Carter, 2009

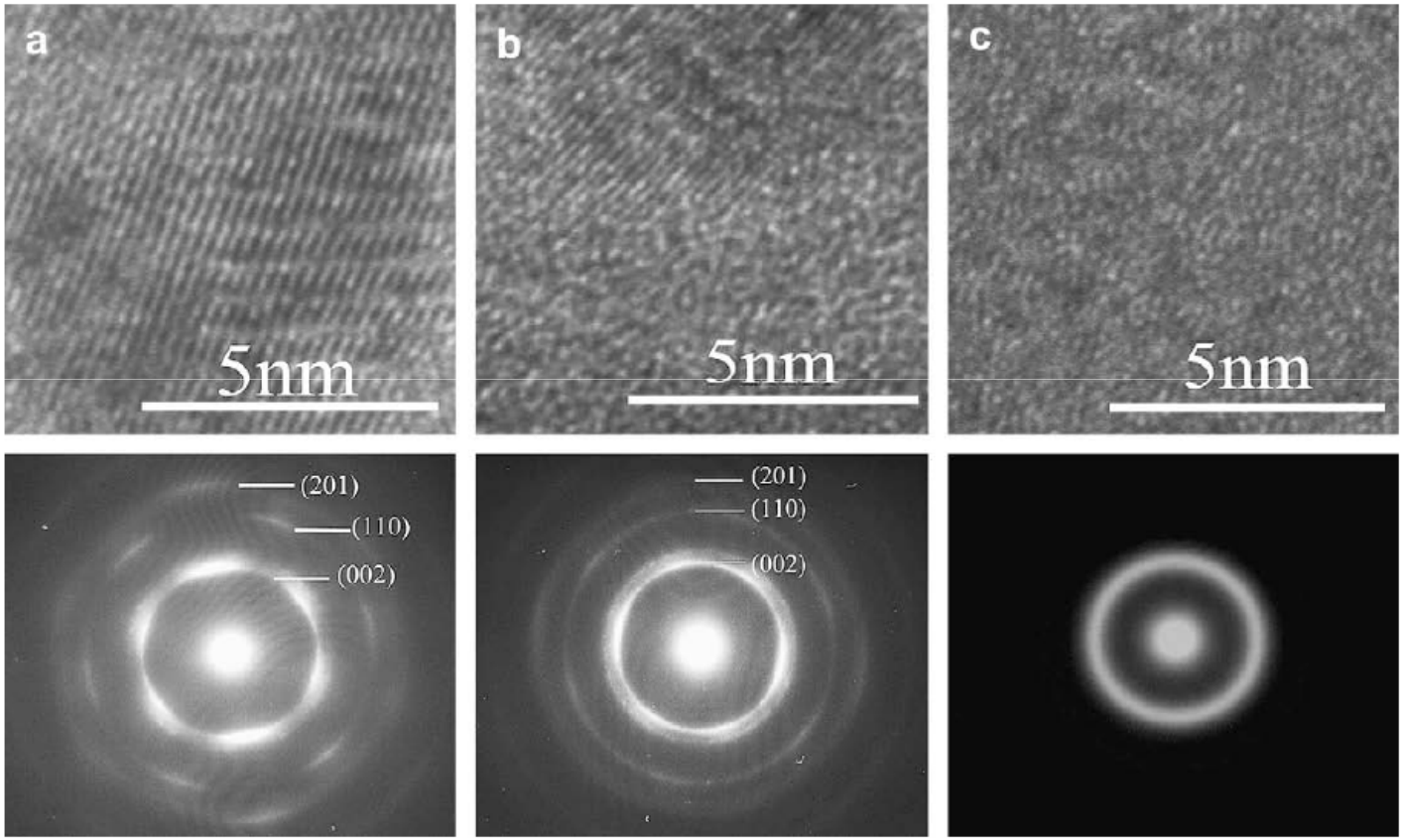
Revestimento de Ti sobre Vidro Metálico Zr10Al5Ni30Cu

Deposição por sputtering a 200ºC



Qin et al. 2009

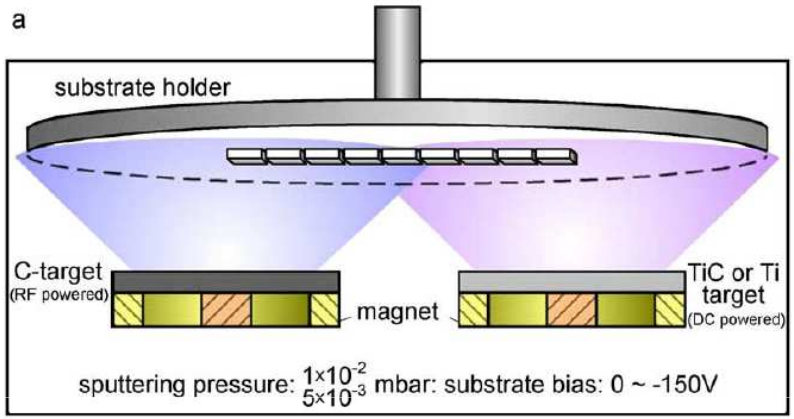
Revestimento de Ti sobre Vidro Metálico Zr10Al5Ni30Cu



Revestimento Interface Vidro

Qin et al. 2009

Revestimento nc-TiC/a-C



Pei et al. (2005)

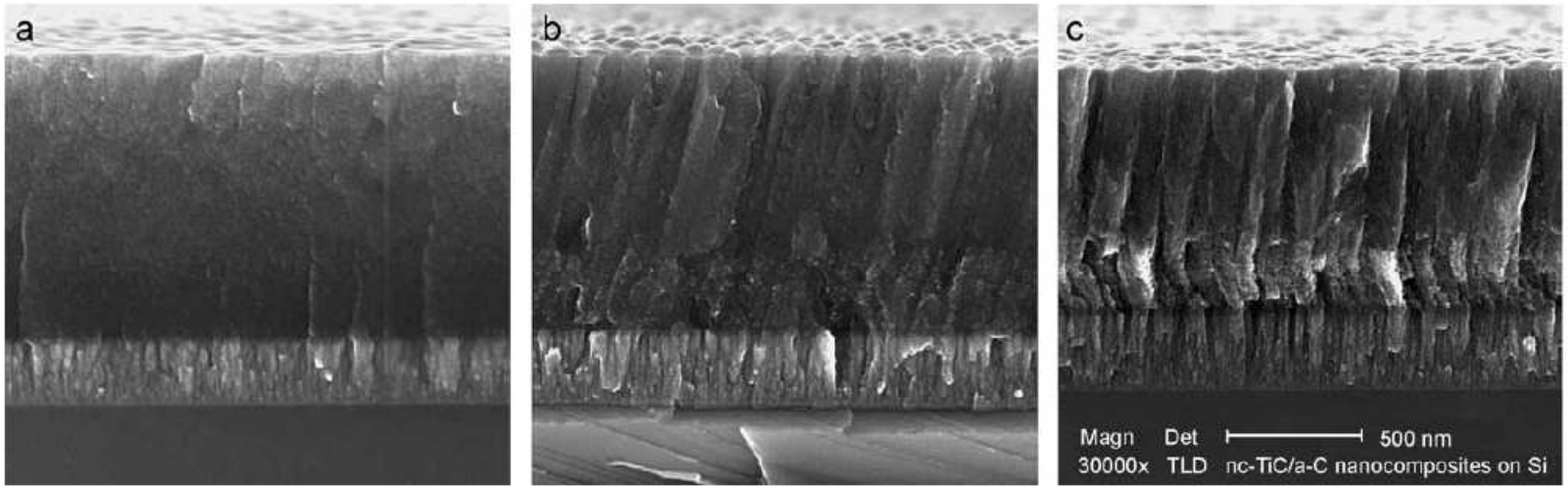


Fig. 2. SEM micrographs of the fractured cross-sections showing the transition from glassy to columnar growth of nc-TiC/a-C coatings with Ti content (at.%) of (a) 10, (b) 17 and (c) 34.

Revestimento nc-TiC/a-C

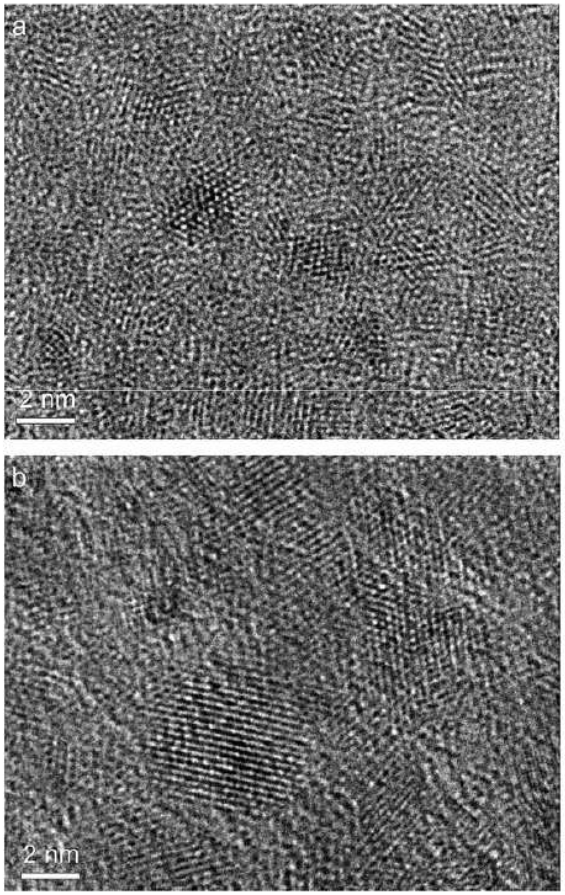
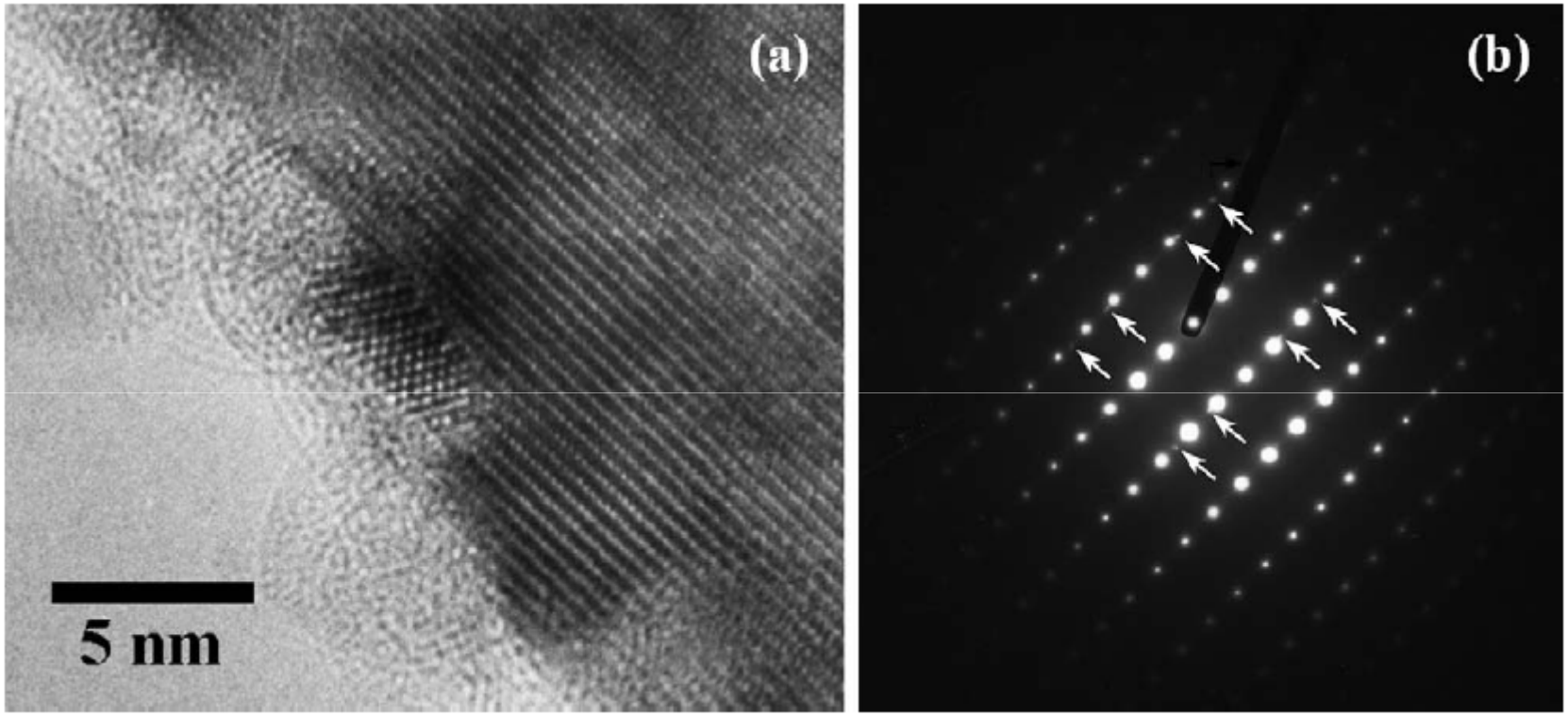


Fig. 4. HRTEM micrographs showing TiC nanocrystallites embedded in a-C:H matrix in nc-TiC/a-C:H nanocomposite: (a) coating HB3 with 17.84 at.% Ti and (b) coating HB5 with 31.75 at.% Ti.

Pei et al. (2005)

Filme de Zircônia Estabilizada ao Ítrio (YSZ)



Partículas de YSZ sobre safira, setas indicam spots de ZrO_2 sobre Al_2O_3 mostrando a relação de epitaxia

normal orientation: $(h\,h\,0)_{YSZ}//(0\,0\,\ell)_{Al_2O_3}$

in-plane orientation: $(1\,1\,3)_{YSZ}//(2\,2\,0)_{Al_2O_3}$

$=>[1\,\bar{1}\,0]_{YSZ}//[\bar{1}\,1\,0]_{Al_2O_3}$.

Thune et al. (2009)

Nanocristais

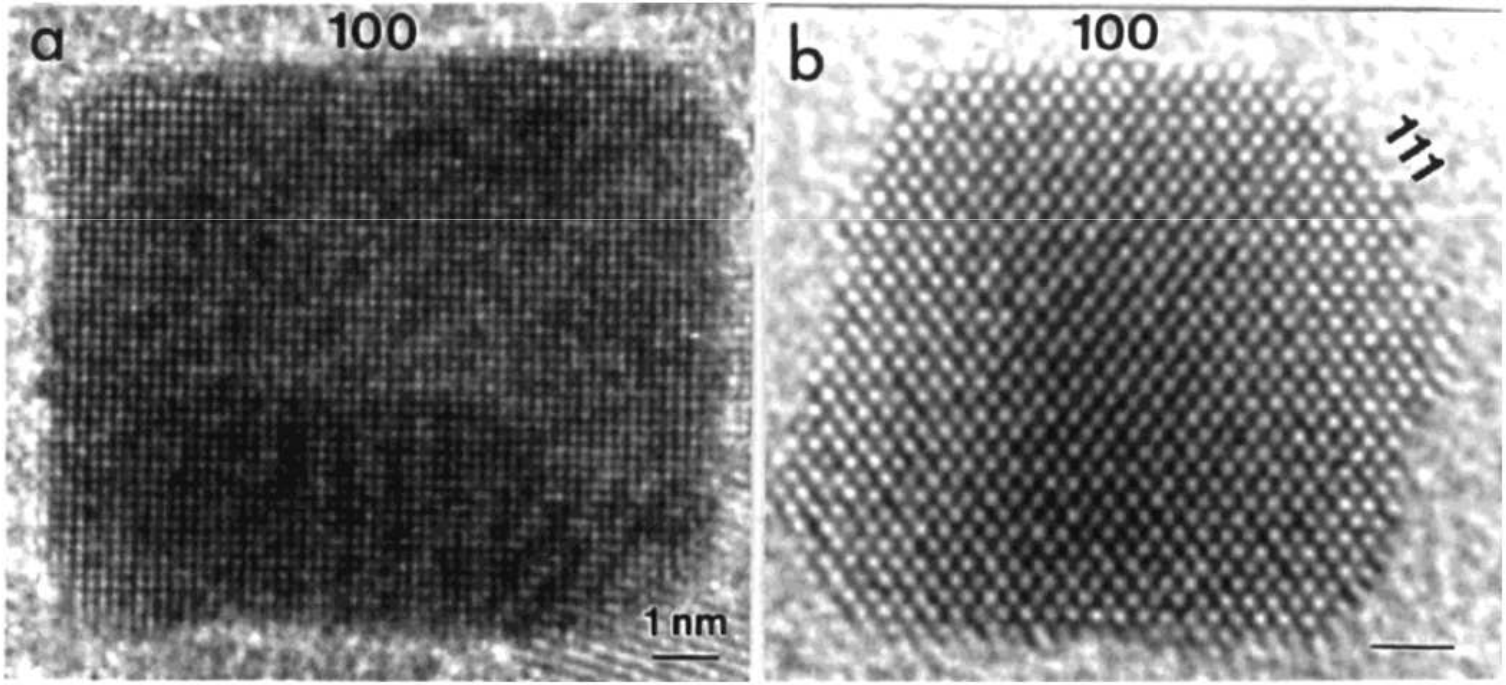


Figure 6. HRTEM images of cubic Pt nanocrystals oriented along (a) [001] and (b) [110], showing surface steps/ledges and the thermodynamically inequilibrium shapes (The Pt nanocrystals were supplied by Prof. M. A. El-Sayed's group).

Nanocristais

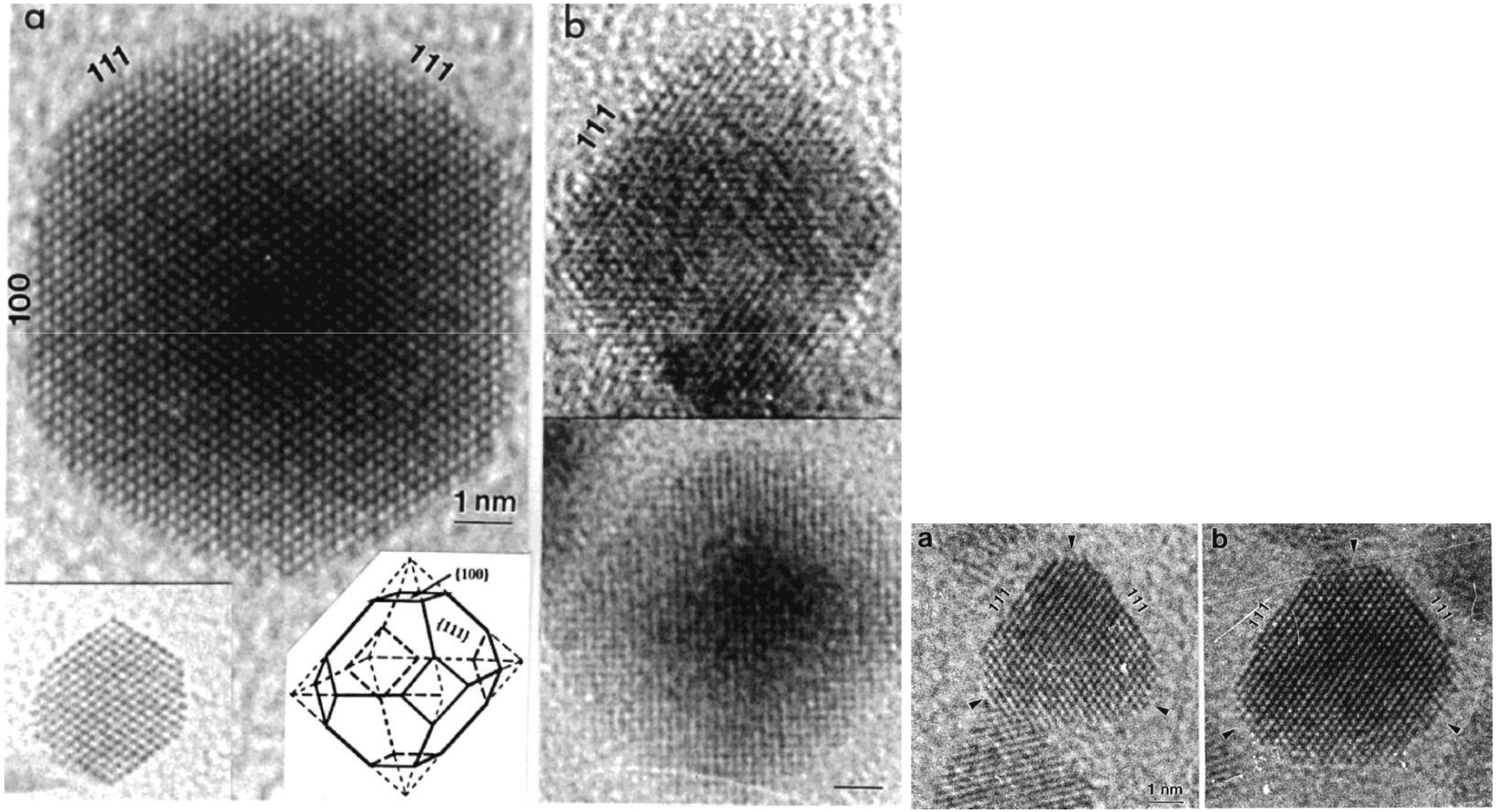
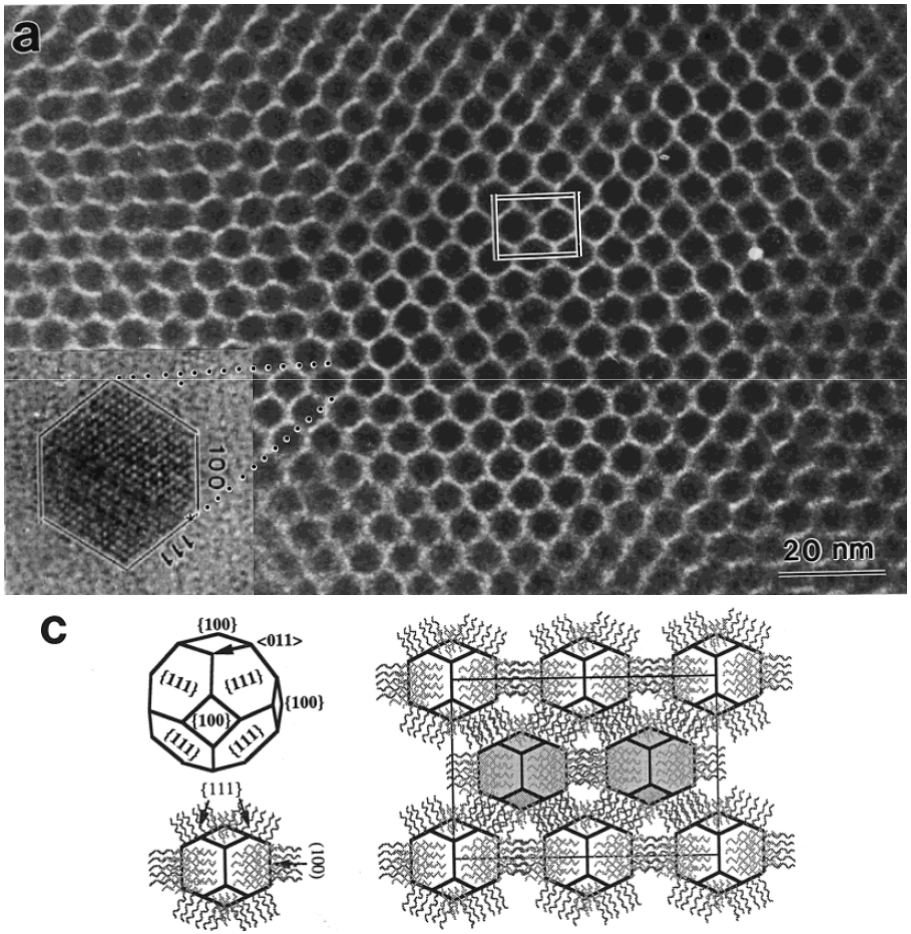


Figure 7. HRTEM images of Pt nanocrystals (a) with a truncated octahedral shape and oriented along [110] and (b) with a octahedral shape and oriented along [110] and [001]. The inset in (a) is a model of the particle shape (The Pt nanocrystals were supplied by Prof. M. A. El-Sayed's group).

J. Phys. Chem. B, Vol. 104, No. 6, 2000

Nanocristais



TEM image of a face-centered cubic packed Ag nanocrystals whose shape is dominated by truncated octahedral (TO)

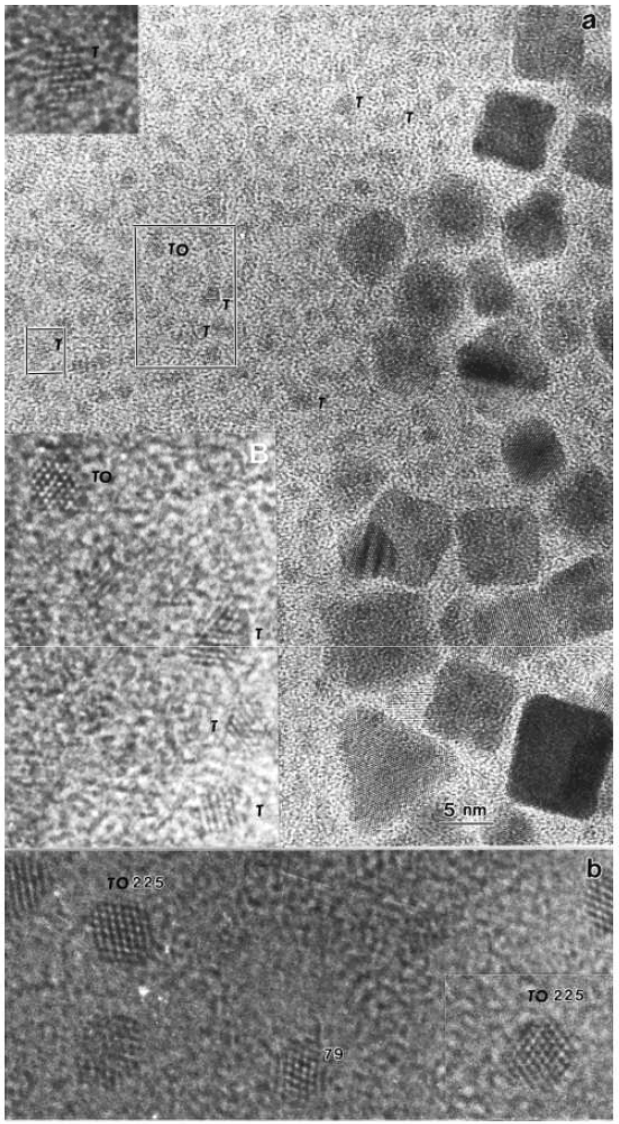


Figure 12. HRTEM image of Pt nanocrystals whose shapes were dominated by tetrahedra when they are small, but a transformation to cubic shape occurred as they grow larger. (b) The possible "smallest" nanocrystals whose shape still can be identified by HRTEM. The numbers represents the possible of numbers of atoms in the particles if they are perfect truncated octahedra without point defects.

Nanofios metálicos

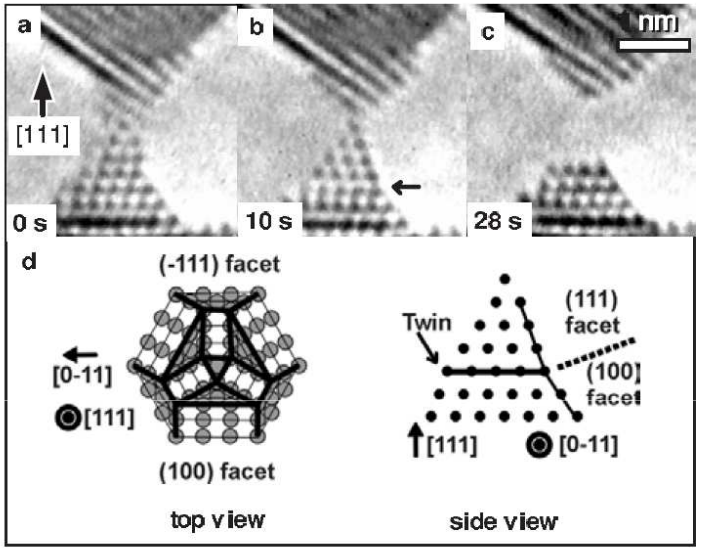


Figure 1. (a)–(c) HRTEM snapshots of a time evolution of a platinum NW formed along the [111] axis. In (b) the arrow indicates the formation of a twin at the fifth layer, counting from the one-atom tip. After rupture, the pyramid rearranges, yielding the structure in (c). Atomic positions appear dark. (d) Top and side view of the proposed atomic arrangement for the tip twinned at the fifth layer.

INSTITUTE OF PHYSICS PUBLISHING — NANOTECHNOLOGY

Nanotechnology **13** (2002) 404–408 — PII: S0957-4484(02)32287-6

Metal nanowires: atomic arrangement and electrical transport properties

Varlei Rodrigues[1,2] **and Daniel Ugarte**[1]

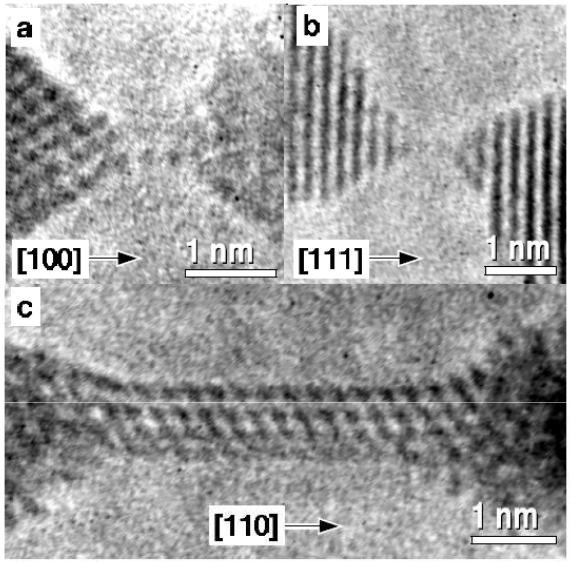


Figure 2. Atomic resolution images of the three kinds of experimentally observed gold NWs: (a) [100] NW, (b) [111] NW and (c) [110] NW. The [100] and [111] NW form bi-pyramidal contacts, while the [110] displays a rod-like neck. Also, [100] NW in (a) shows an example of the suspended atom chain structure formed by two atoms.

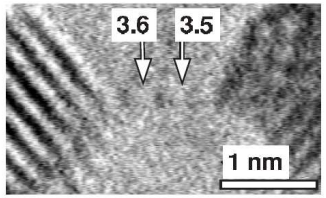
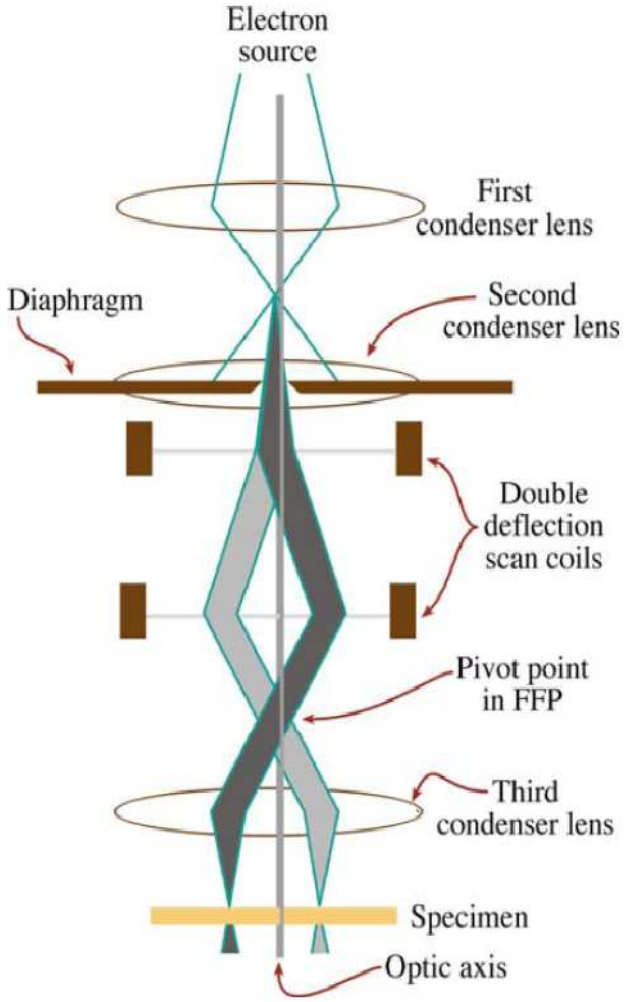


Figure 3. Atomic resolved image of an atom chain formed by three atoms. The distances are marked in Å (∓0.2 Å).

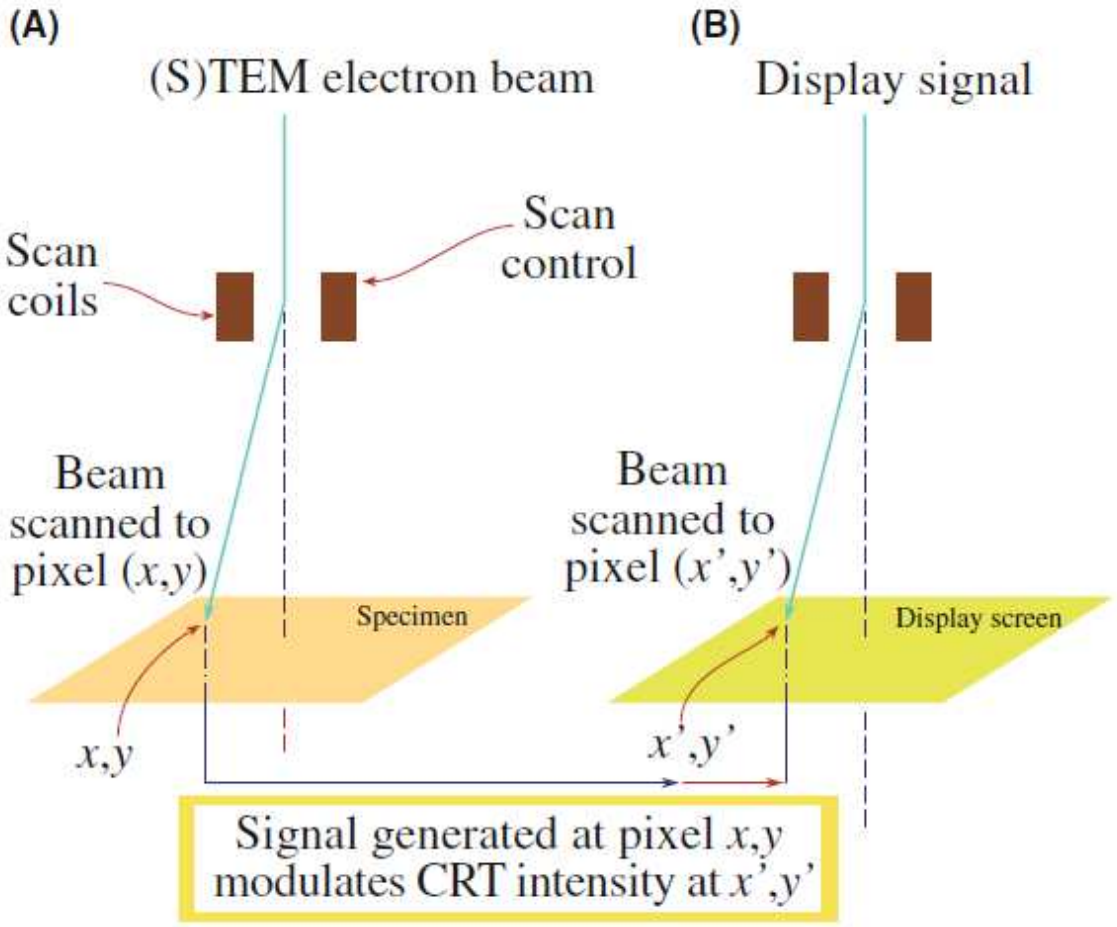
STEM

No STEM, um feixe convergente tão pequeno quanto possível varre a amostra sem variação de inclinação simulando a incidência paralela de um TEM.



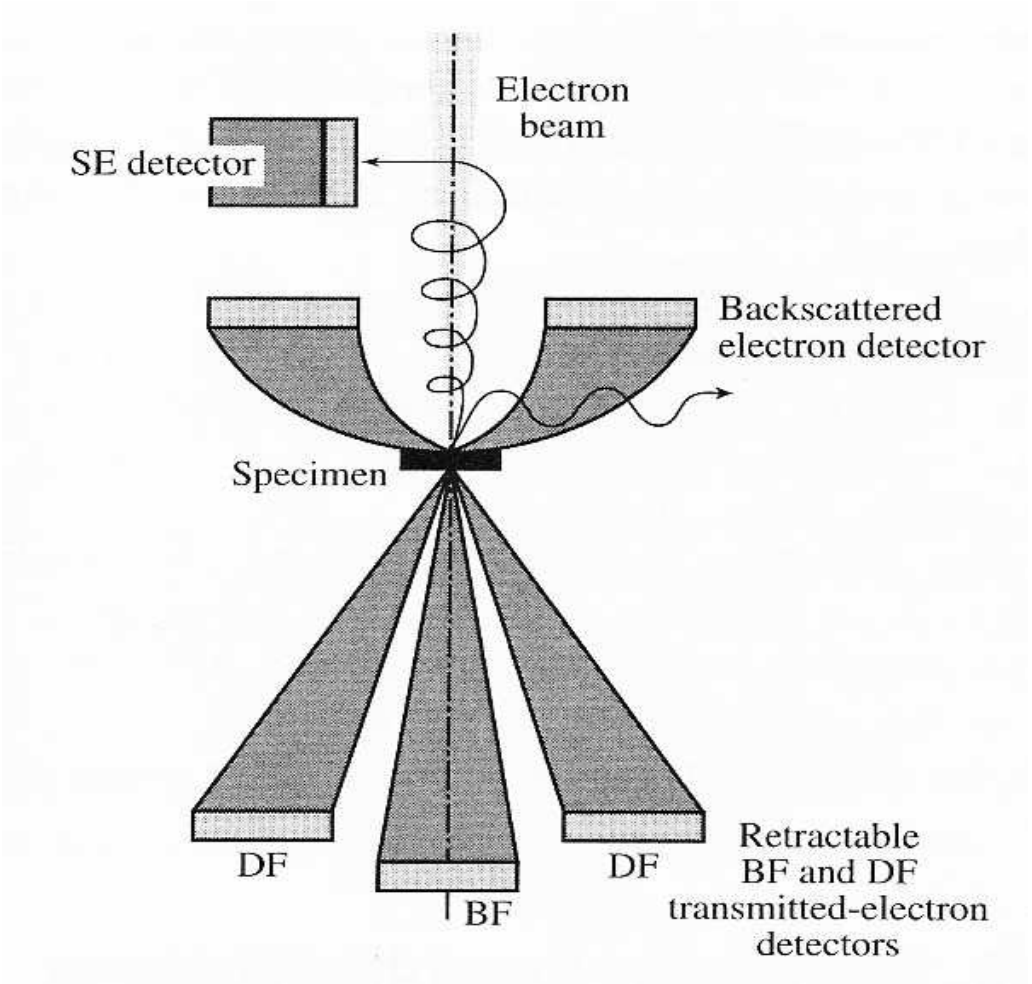
Williams e Carter, 2009

Imagem por Varredura



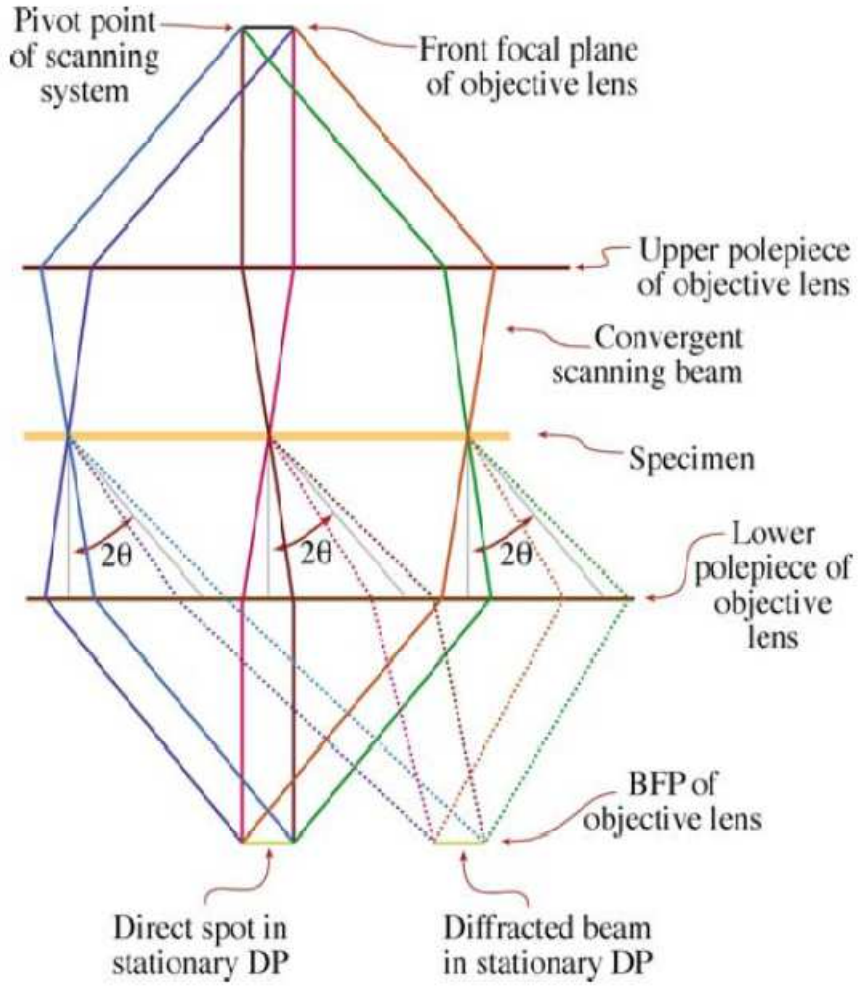
Williams e Carter, 2009

Detectores de Elétrons



STEM

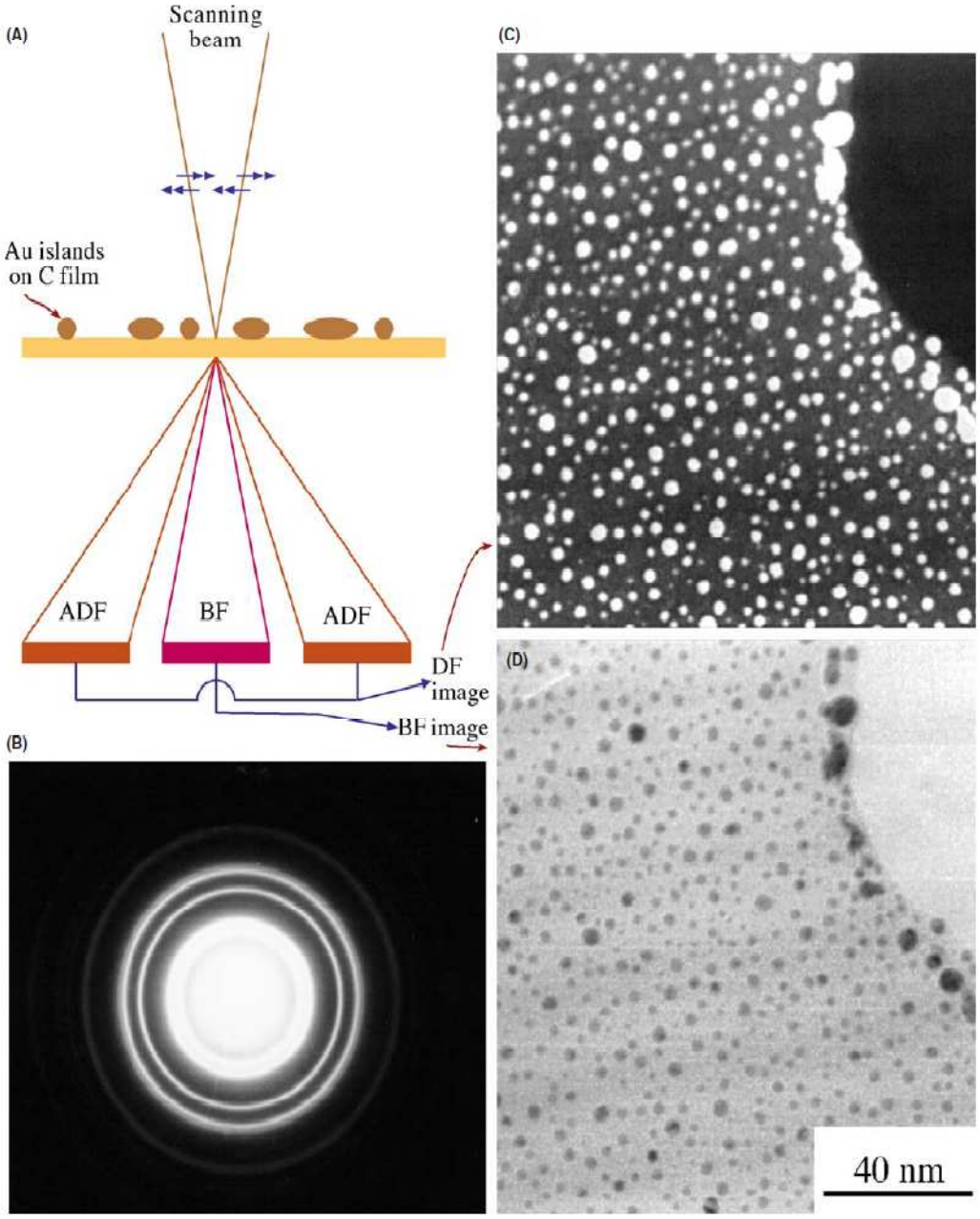
Um detector de elétrons pode ser colocado no plano focal posterior ou em algum de seus planos conjugados se o equipamento for operar como um TEM/STEM.



Williams e Carter, 2009

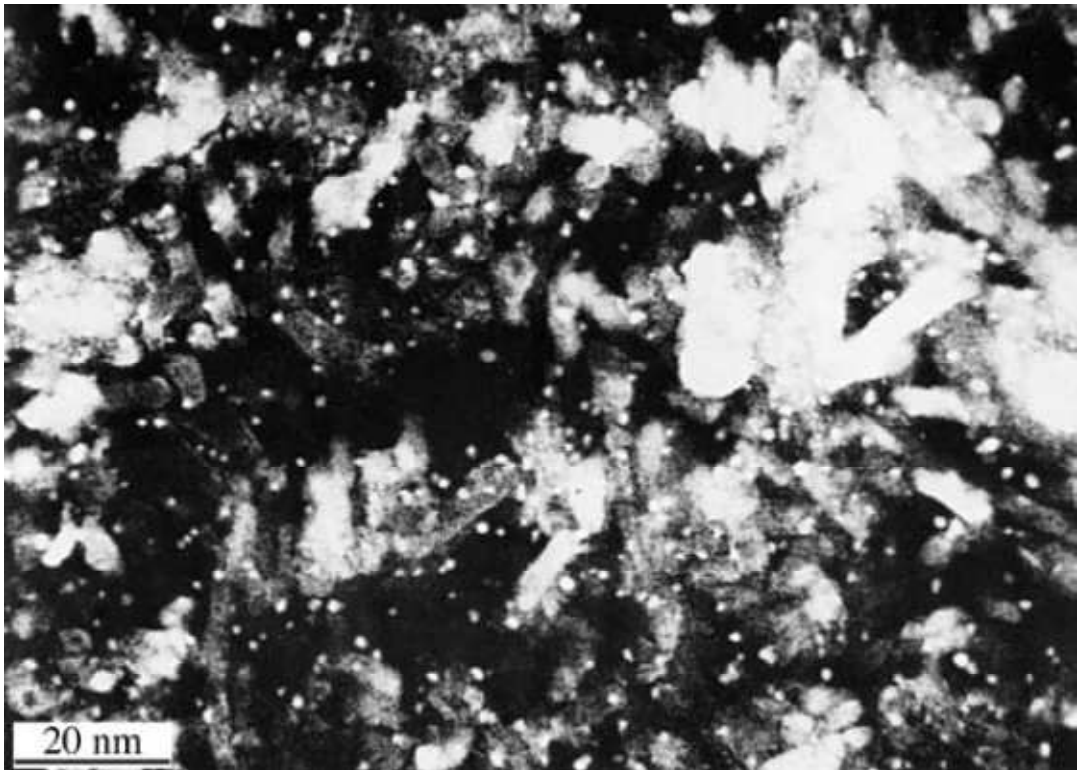
STEM

A realização de figura de campo claro ou escuro depende apenas da seleção do sinal de interesse.

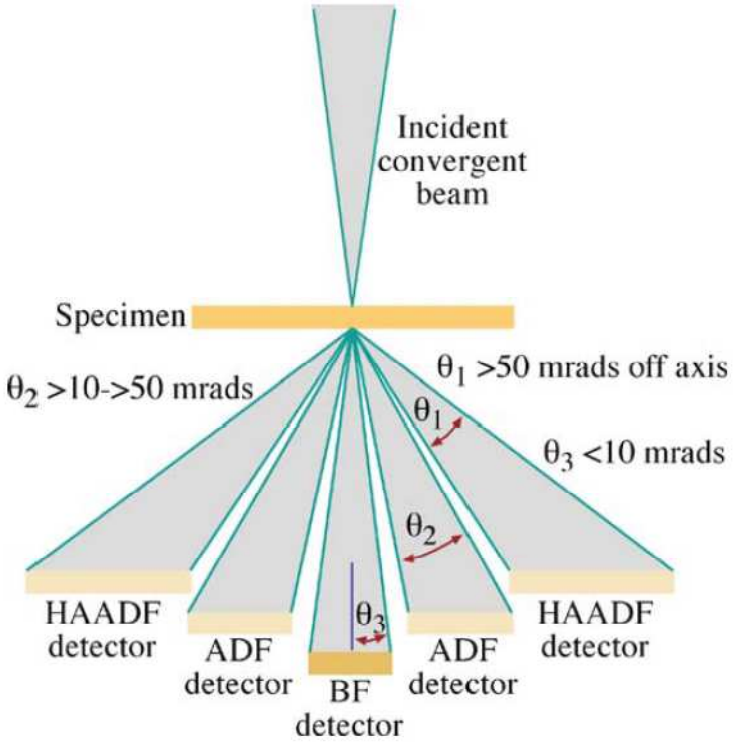


Williams e Carter, 2009

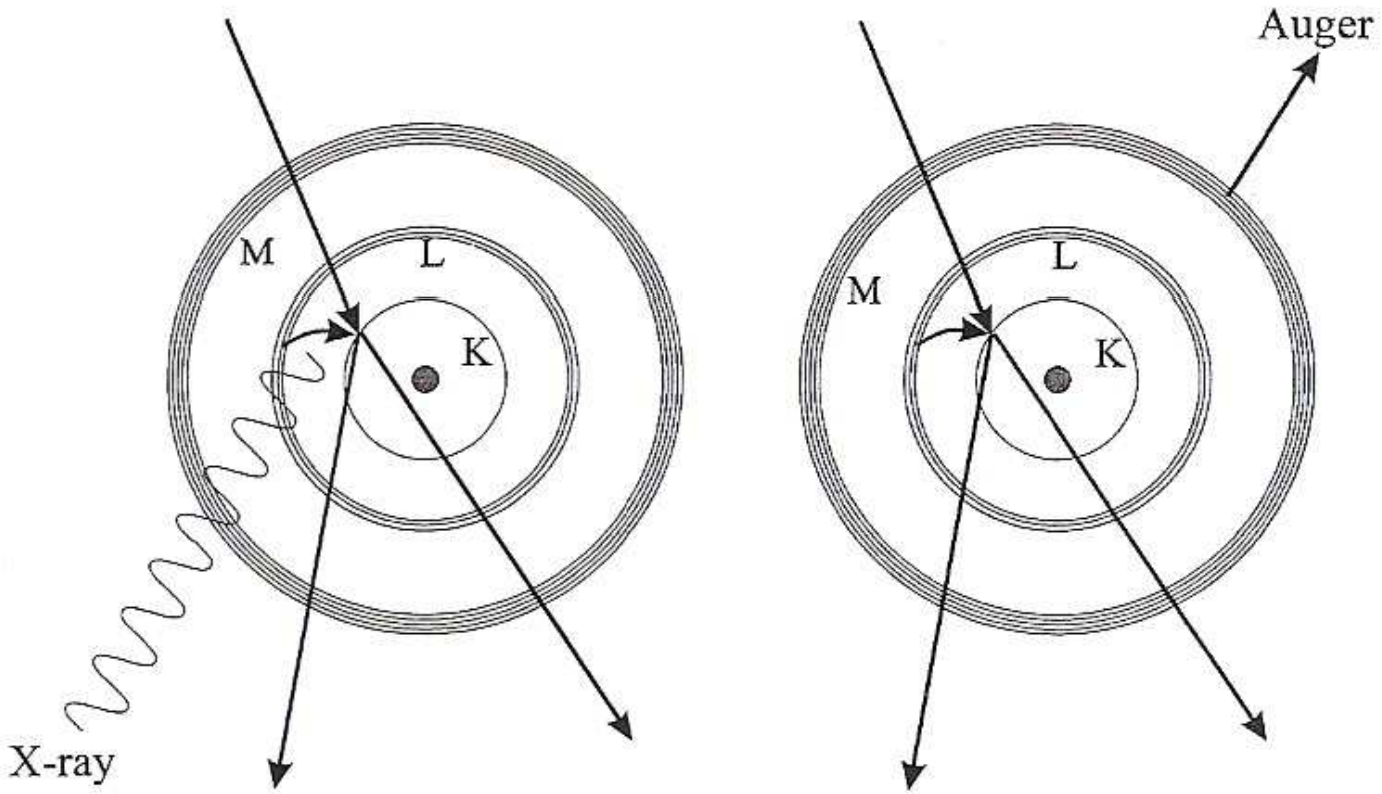
STEM



Pt em filme policristalino de Al_2O_3



Geração de Raios-X

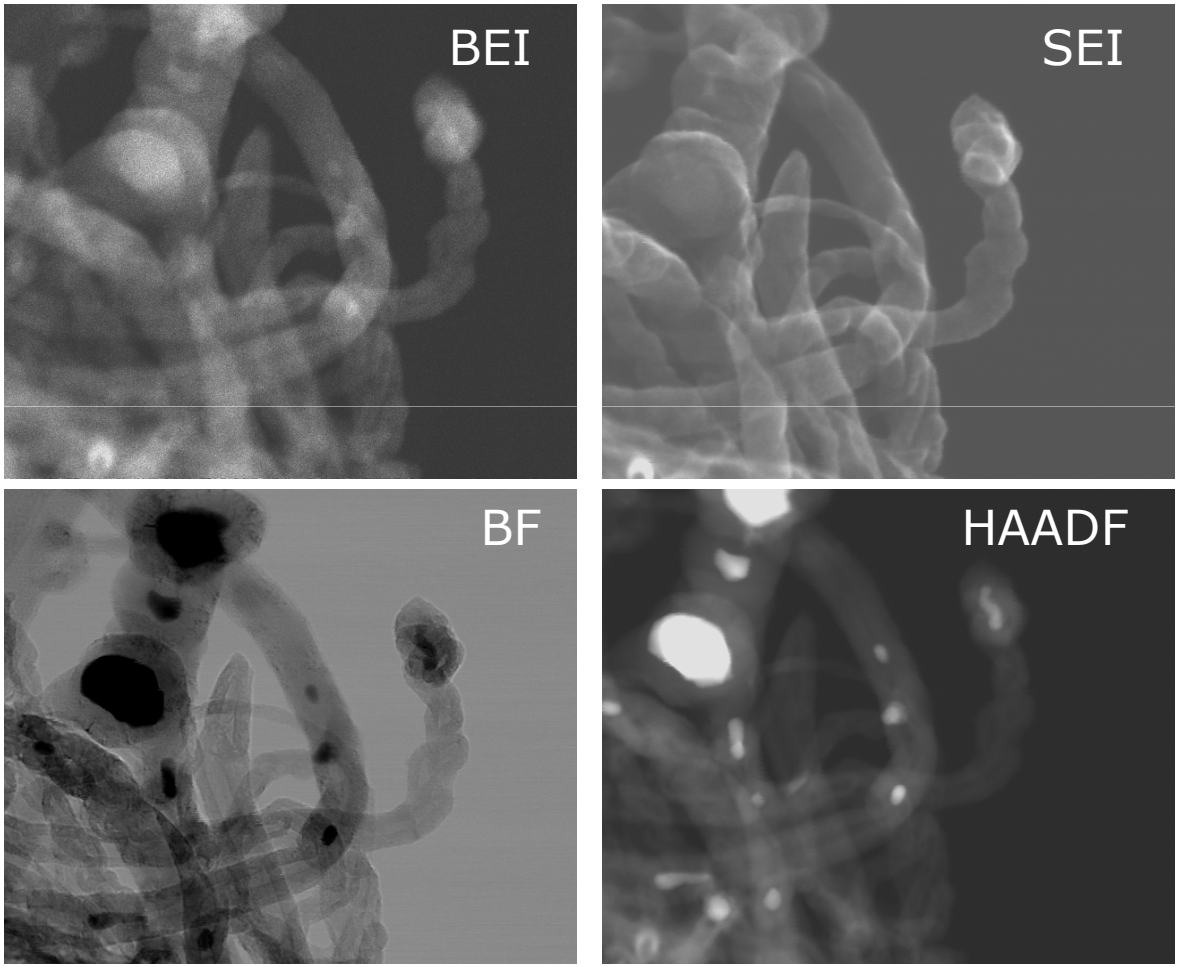


Goodhew, 2001

Detectores de Elétrons Alta Energia

Surface morphology with composition signal

Transmission



Surface morphology

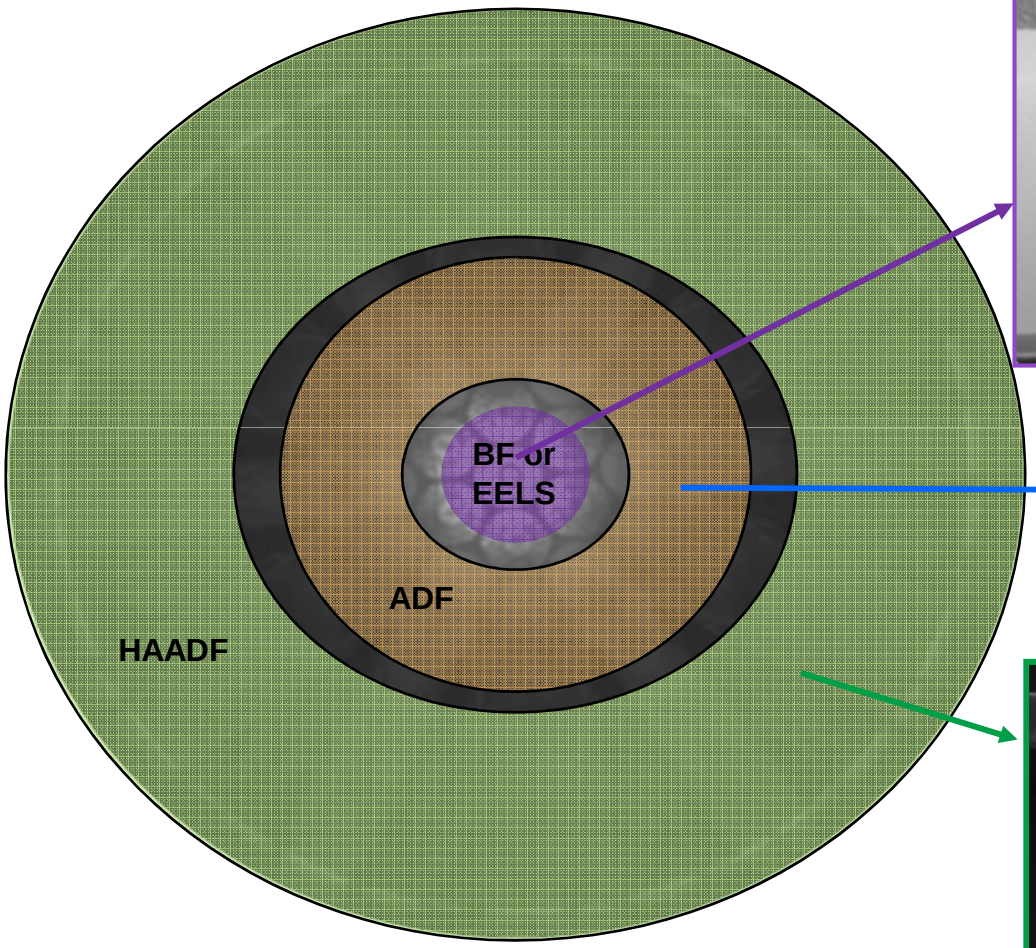
Z-contrast

Specimen: Catalyst in the carbon nanotube

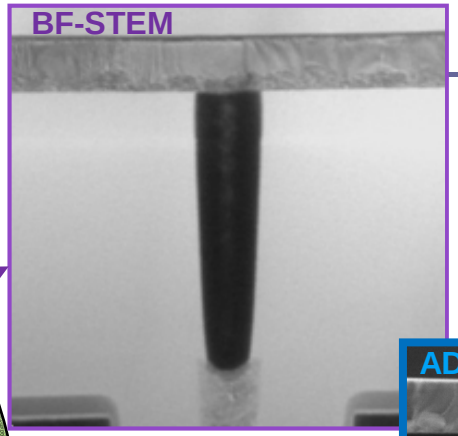
50 nm

Jeol

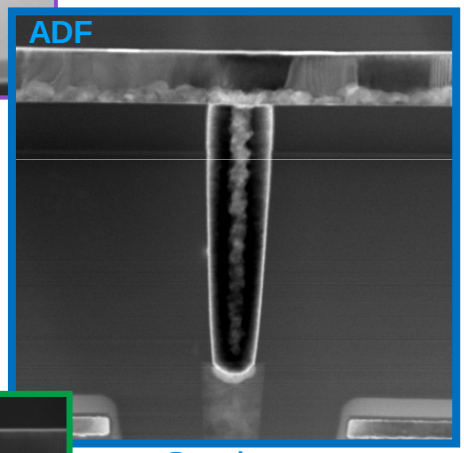
STEM



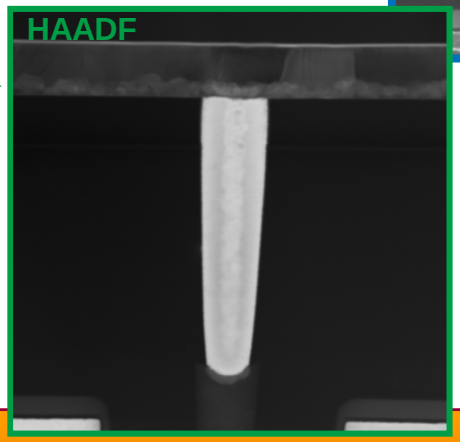
Gatan



Diffraction contrast & phase contrast

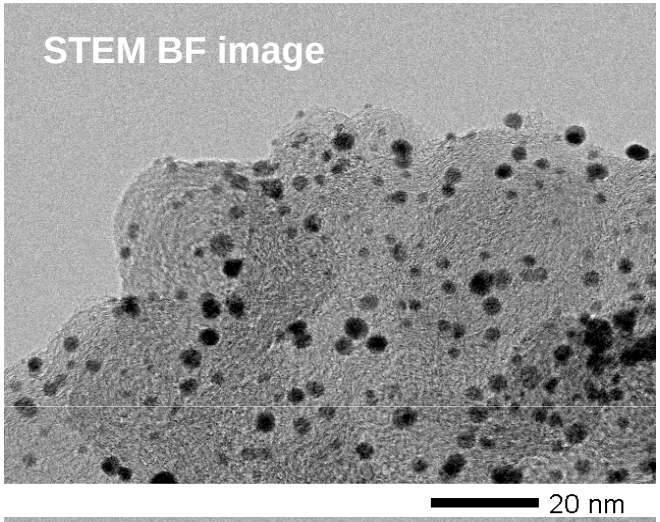


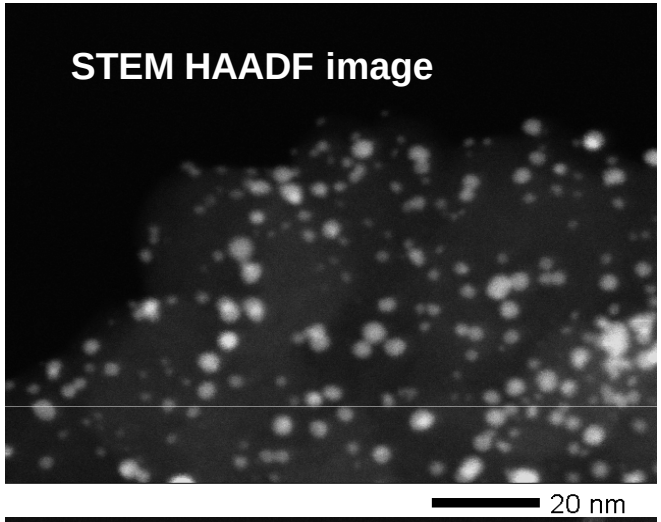
Strain contrast sensitive

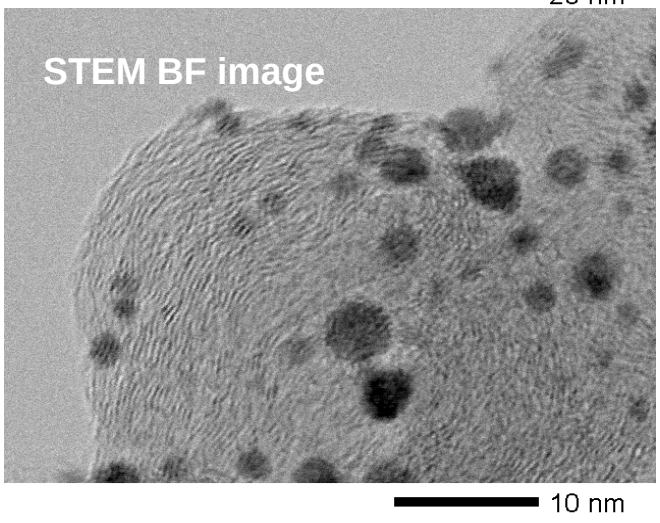


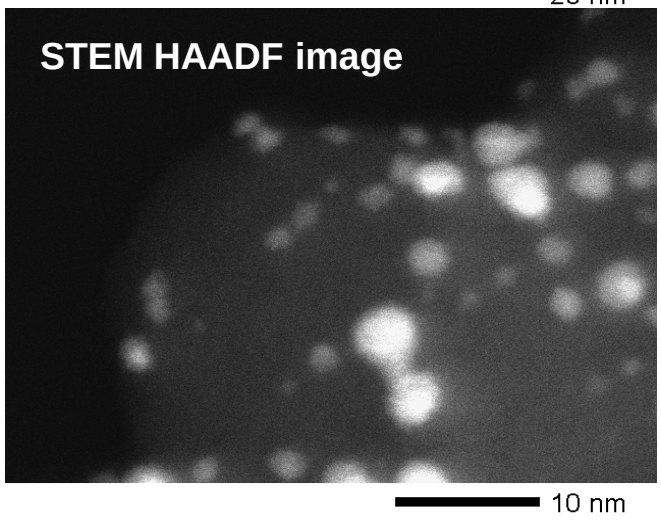
"Z" contrast

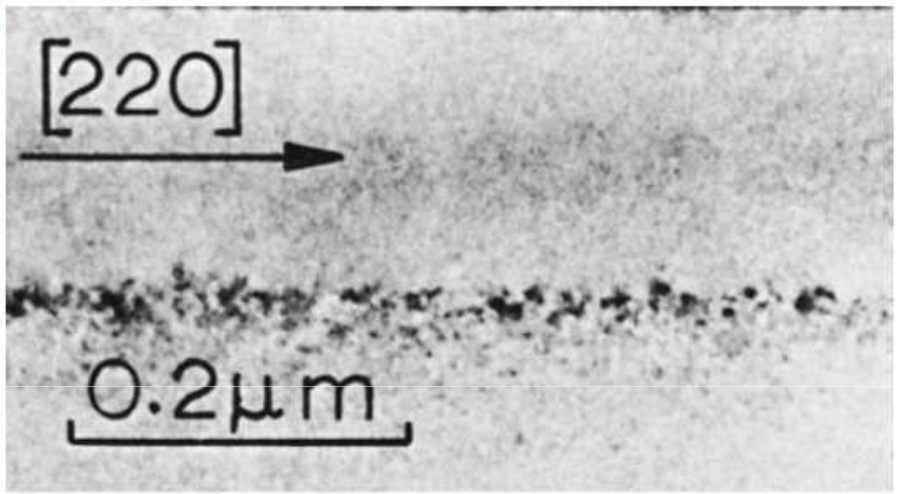
STEM Images of 20% Pt-C Catalyst











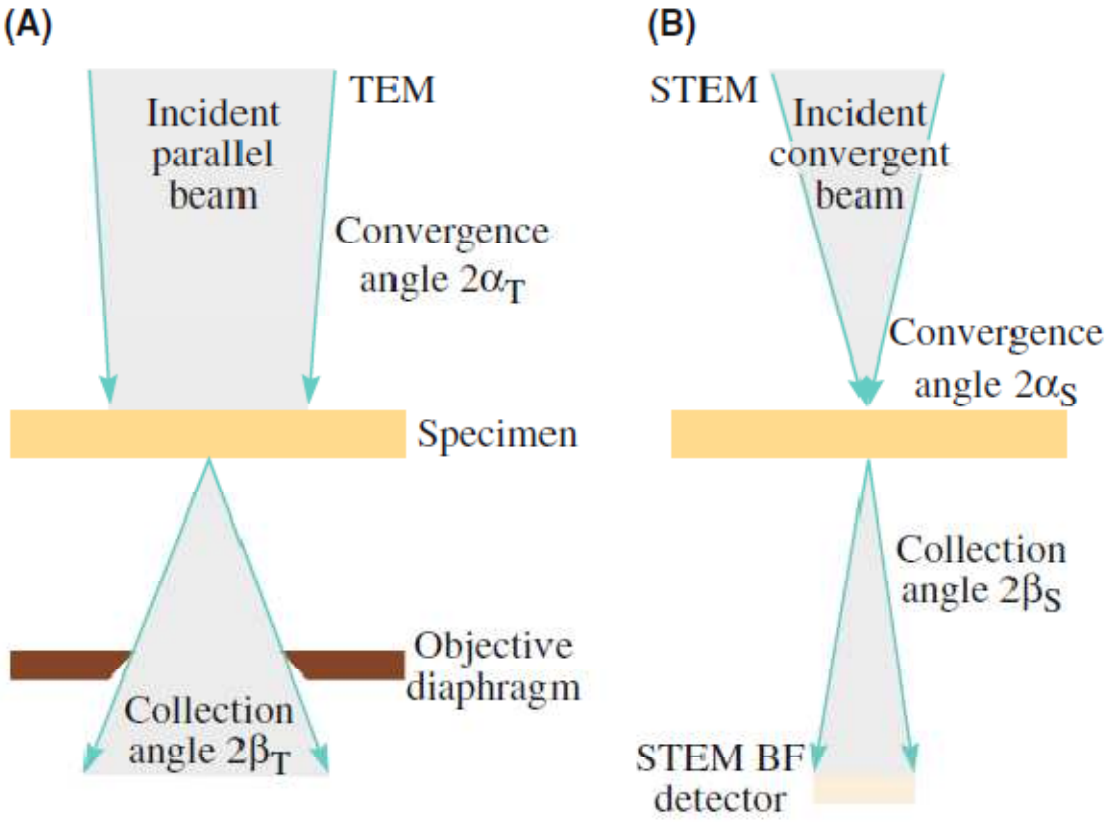


TEM – Contraste de difração
Defeitos em Si com Bi implantado

STEM – Contraste de Z
Claro na região com Bi implantado

Williams e Carter, 2009

STEM

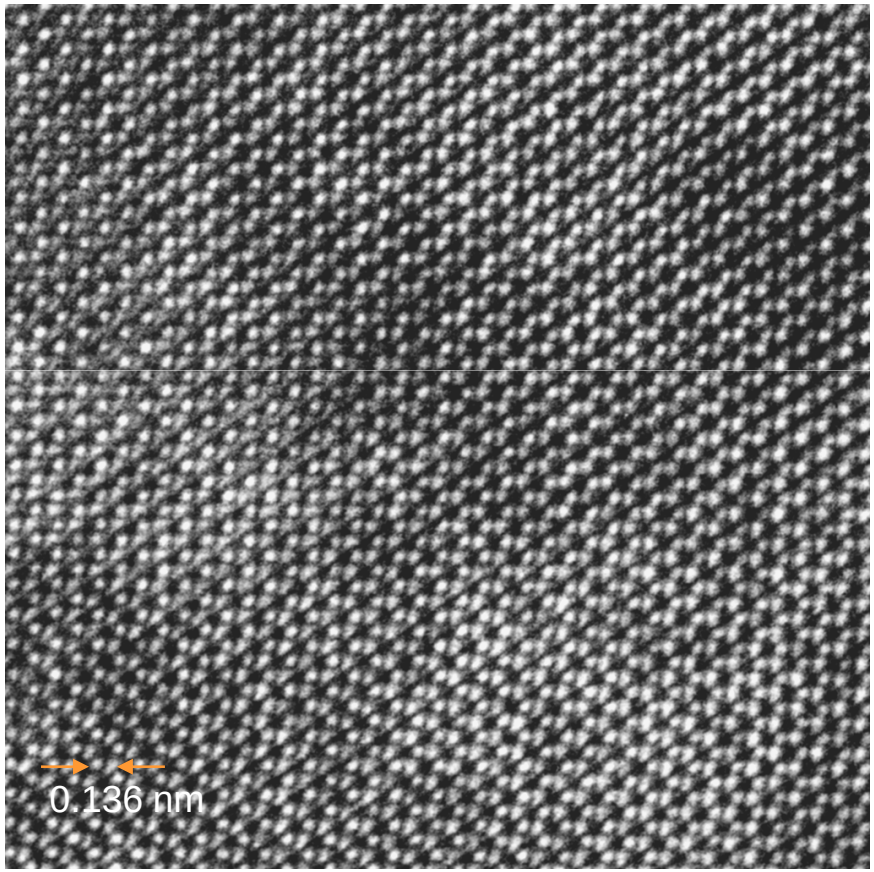


Williams e Carter, 2009

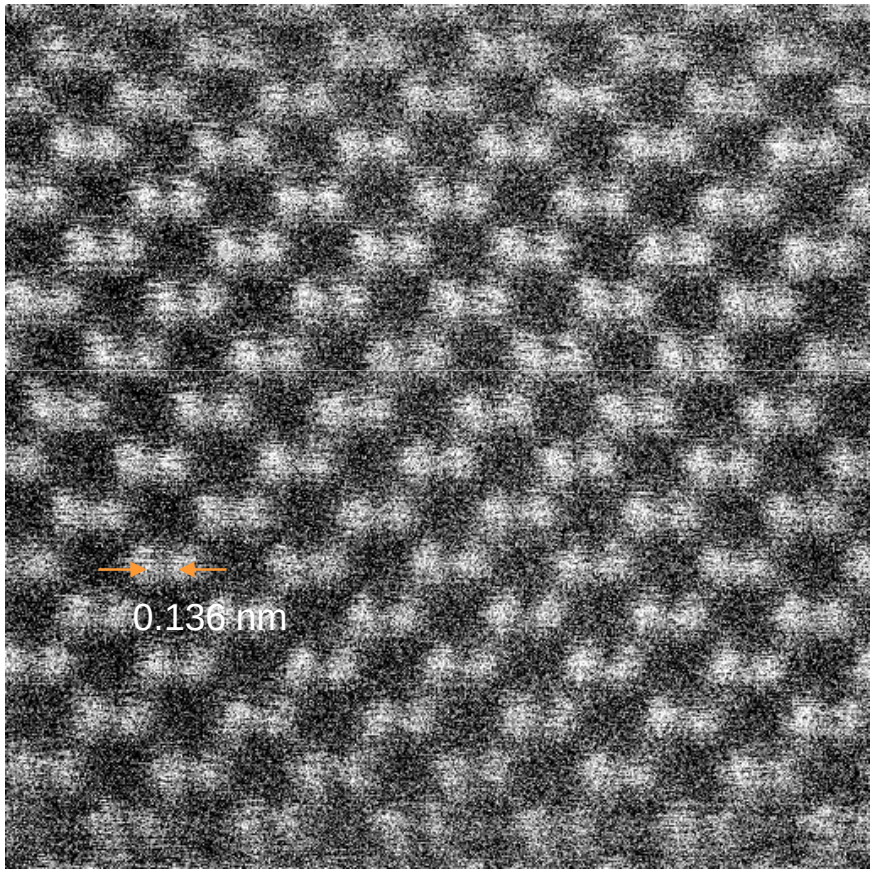
Se:
$\alpha_T = \alpha_S$ e $\beta_T = \beta_S$
as condições de operação em TEM e STEM seriam idênticas. Como isso é impossível, faz-se:
$\alpha_S = \beta_T$ e $\beta_S = \alpha_T$

Através do princípio da reciprocidade, sabe-se que se os caminhos dos raios contêm ângulos equivalentes em algum ponto de um sistema ótico, o contraste da imagem será idêntico.

Si [110] Dumbbell



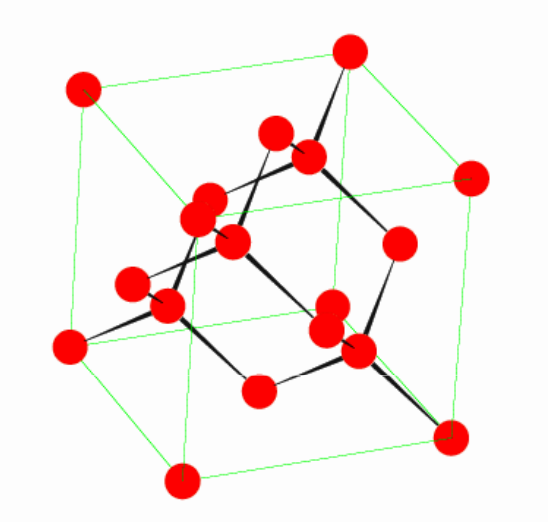
TEM

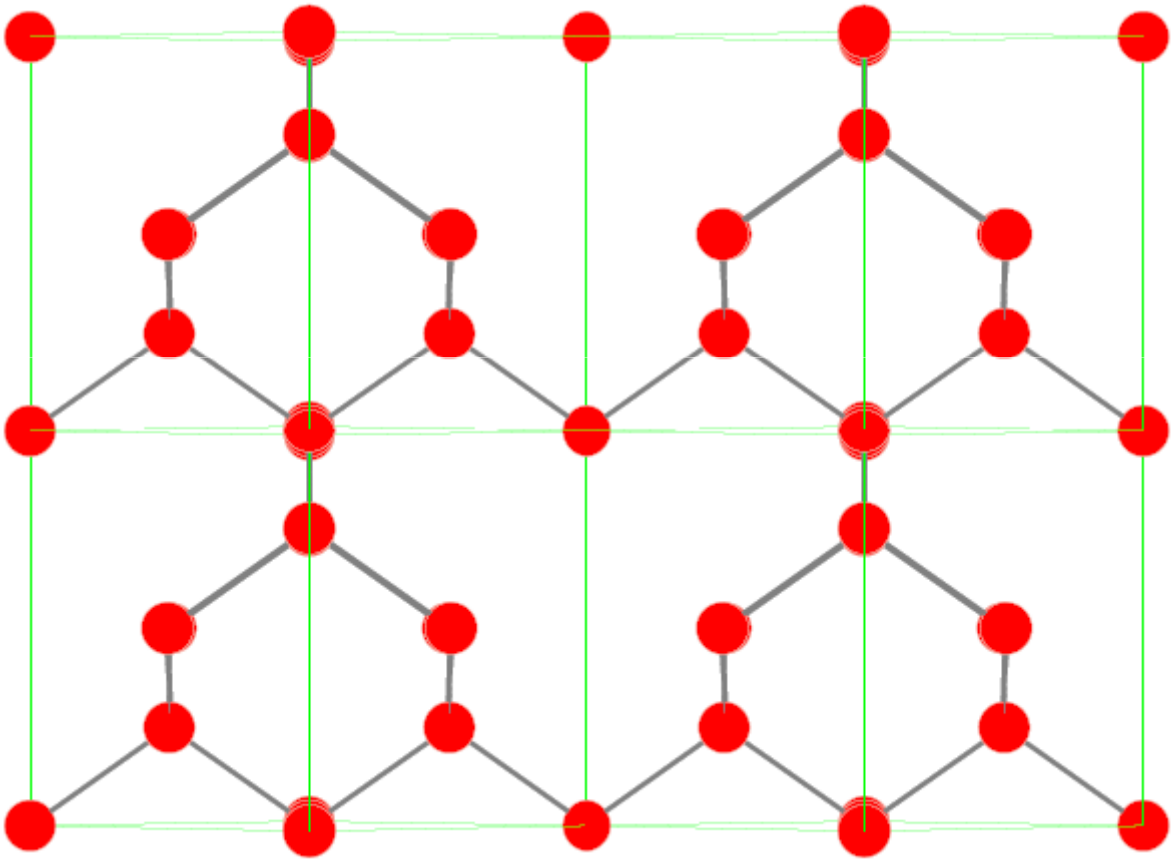


STEM

Jeol

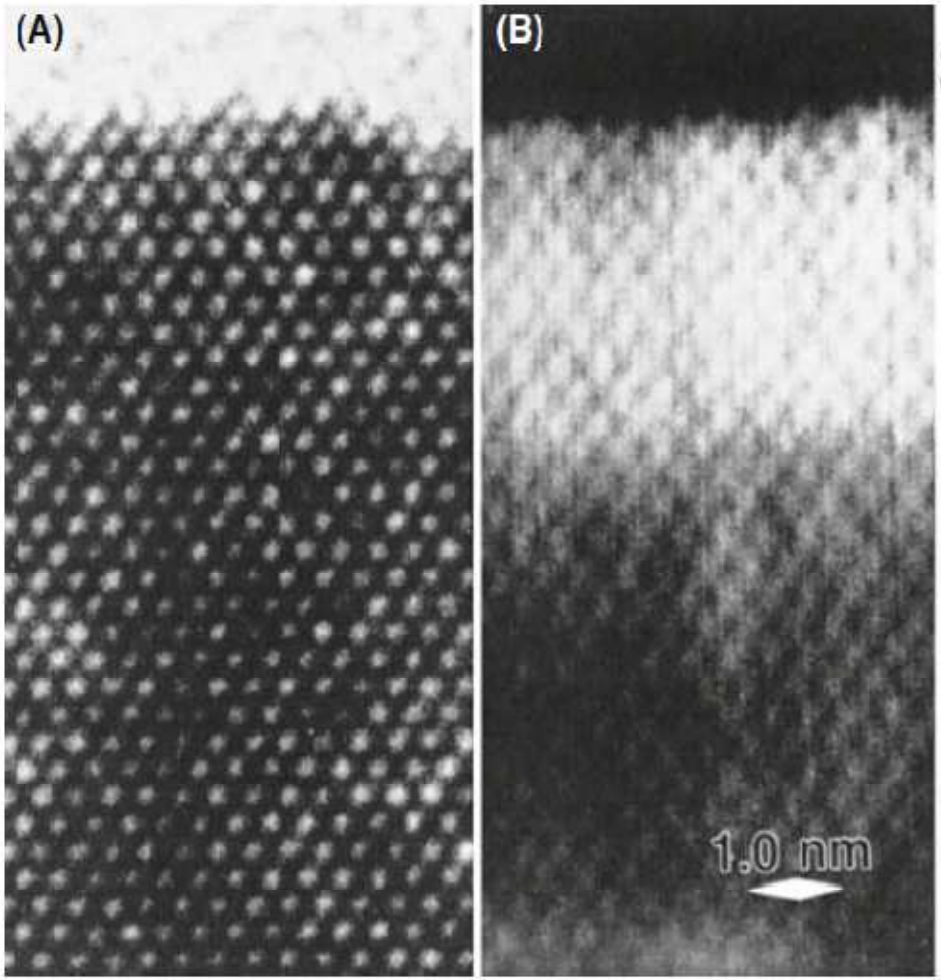
Si [110] Dumbbell





STEM

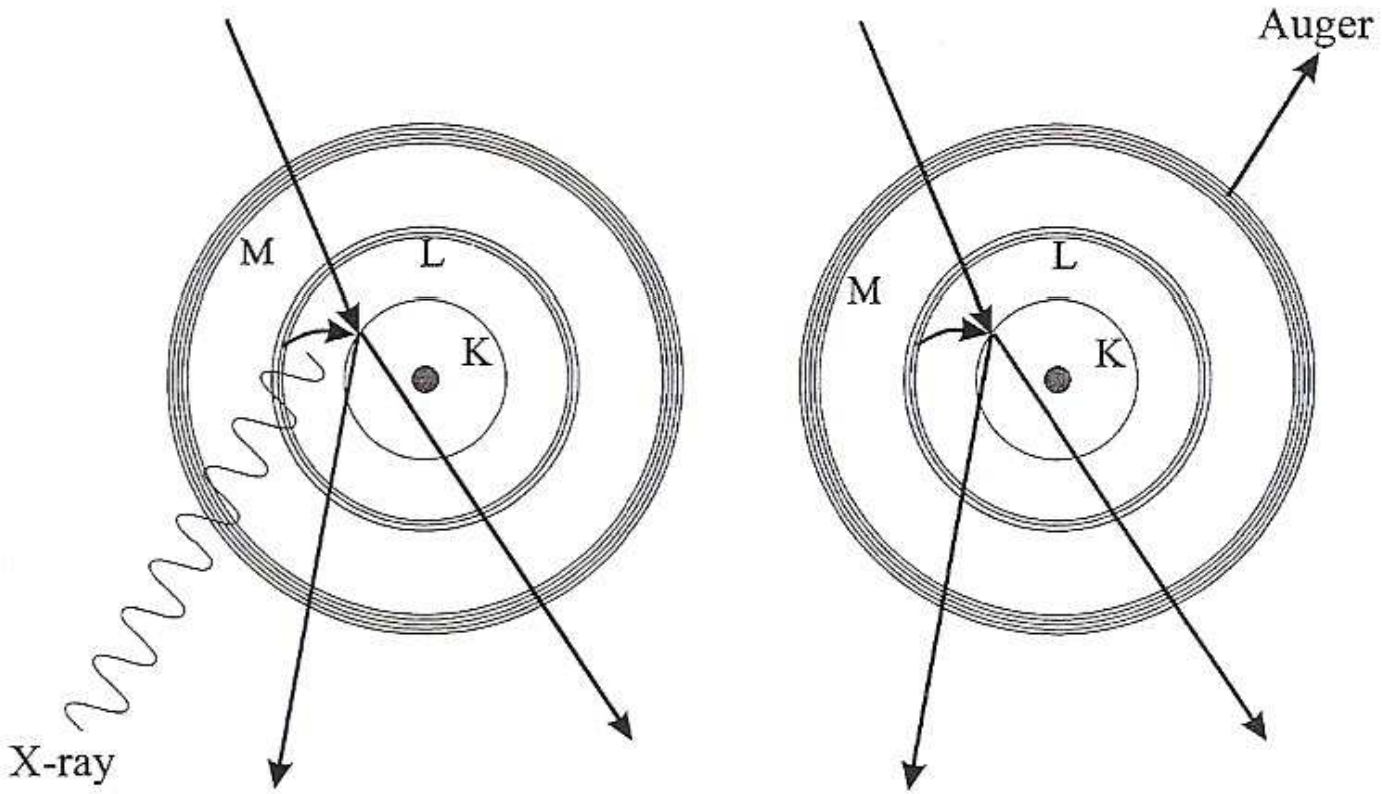
TEM
Contraste de fase



STEM
Contraste de Z

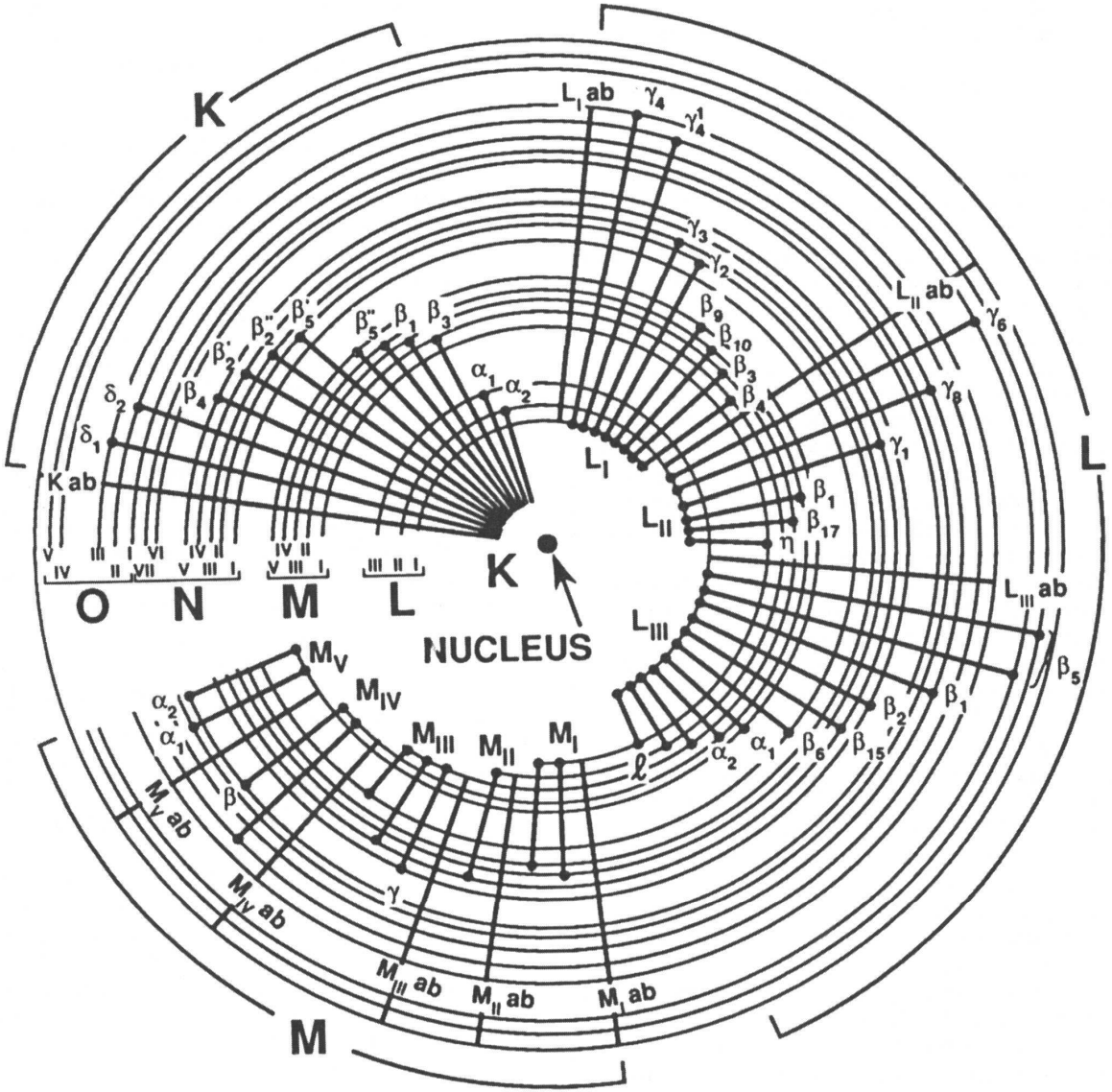
Williams e Carter, 2009

Geração de Raios-X



Goodhew, 2001

Raios-X Característicos



Jeol

Energy Table

element	Kα	Kβ1	Kab	Lα1	Lβ1	Lβ2	Lγ1	Llab	Lllab	Llllab	Mα1
1 H											
2 He											
3 Li											
4 Be											
5 B	0.183		0.192								
6 C	0.277		0.284								
7 N	0.392		0.400								
8 O	0.525		0.532								
9 F	0.677		0.687								
10 Ne	0.849		0.867								
11 Na	1.041	1.067	1.072								
12 Mg	1.254	1.296	1.303								
13 Al	1.487	1.553	1.560								
14 Si	1.740	1.829	1.840								
15 P	2.013	2.136	2.144								
16 S	2.308	2.464	2.471								
17 Cl	2.622	2.816	2.820								
18 Ar	2.957	3.191	3.203								
19 K	3.313	3.590	3.608								
20 Ca	3.691	4.013	4.038	0.341	0.345				0.353	0.349	
21 Sc	4.089	4.461	4.489	0.396	0.400						
22 Ti	4.509	4.932	4.965	0.452	0.458						
23 V	4.950	5.428	5.464	0.511	0.519						
24 Cr	5.412	5.947	5.989	0.573	0.583			0.742	0.693	0.599	
25 Mn	5.895	6.491	6.538	0.638	0.649						
26 Fe	6.400	7.058	7.111	0.705	0.718				0.721	0.708	
27 Co	6.925	7.650	7.710	0.776	0.791				0.794	0.779	
28 Ni	7.473	8.265	8.332	0.852	0.869				0.871	0.854	
29 Cu	8.042	8.906	8.981	0.930	0.950				0.953	0.933	
30 Zn	8.632	9.572	9.661	1.012	1.035			1.198	1.045	1.022	
31 Ga	9.243	10.265	10.368	1.098	1.125			1.303	1.145	1.117	
32 Ge	9.876	10.983	11.104	1.188	1.219			1.413	1.249	1.217	
33 As	10.532	11.727	11.865	1.282	1.317			1.529	1.359	1.324	
34 Se	11.209	12.496	12.655	1.379	1.419			1.653	1.475	1.434	
35 Br	11.909	13.292	13.471	1.481	1.526			1.782	1.599	1.553	
36 Kr	12.634	14.113	14.325	1.586	1.637			1.916	1.730	1.677	
37 Rb	13.376	14.961	15.204	1.694	1.752			2.064	1.866	1.807	
38 Sr	14.142	15.837	16.108	1.807	1.872			2.217	2.009	1.941	
39 Y	14.934	16.739	17.038	1.923	1.996			2.377	2.154	2.080	
40 Zr	15.748	17.669	18.000	2.042	2.125	2.219	2.303	2.541	2.305	2.222	
41 Nb	16.584	18.622	18.987	2.166	2.257	2.367	2.462	2.710	2.464	2.371	
42 Mo	17.446	19.609	20.004	2.293	2.395	2.518	2.624	2.881	2.627	2.524	
43 Tc	18.327	20.620	21.047	2.424	2.537			3.055	2.795	2.678	
44 Ru	19.237	21.657	22.120	2.559	2.683	2.836	2.965	3.233	2.966	2.838	
45 Rh	20.170	22.725	23.218	2.697	2.835	3.001	3.144	3.417	3.145	3.002	
46 Pd	21.125	23.820	24.349	2.839	2.990	3.172	3.329	3.608	3.330	3.173	
47 Ag	22.105	24.942	25.517	2.984	3.151	3.348	3.520	3.807	3.526	3.351	
48 Cd	23.110	26.097	26.715	3.134	3.317	3.528	3.717	4.019	3.728	3.538	
49 In	24.140	27.279	27.943	3.287	3.487	3.714	3.921	4.237	3.939	3.730	
50 Sn	25.195	28.489	29.194	3.444	3.663	3.905	4.131	4.465	4.157	3.929	
51 Sb	26.279	29.725	30.486	3.605	3.844	4.101	4.348	4.699	4.382	4.132	
52 Te	27.382	30.996	31.816	3.770	4.030	4.302	4.571	4.940	4.613	4.342	
53 I	28.515	32.296	33.169	3.938	4.221	4.508	4.801	5.192	4.854	4.599	
54 Xe	29.669	33.628	34.594	4.110				5.453	5.104	4.782	

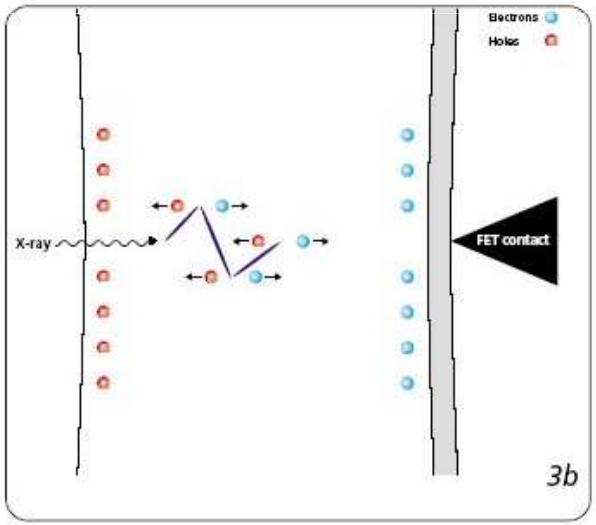
element	Kα	Kβ1	Kab	Lα1	Lβ1	Lβ2	Lγ1	Llab	Lllab	Llllab	Mα1
55 Cs	30.857	34.985	35.990	4.287	4.620	4.936	5.281	5.721	5.358	5.012	
56 Ba	32.071	36.381	37.458	4.466	4.828	5.157	5.531	5.996	5.623	5.247	
57 La	33.302	37.800	38.940	4.651	5.042	5.384	5.789	6.268	5.889	5.484	0.833
58 Ce	34.575	39.261	40.452	4.840	5.262	5.613	6.052	6.548	6.161	5.724	0.883
59 Pr	35.865	40.744	42.000	5.034	5.489	5.850	6.322	6.835	6.439	5.963	0.929
60 Nd	37.188	42.272	43.580	5.231	5.722	6.090	6.602	7.130	6.724	6.210	0.978
61 Pm	38.541	43.826	45.201	5.433	5.962	6.339	6.892	7.436	7.014	6.461	
62 Sm	39.918	45.416	46.858	5.636	6.205	6.587	7.178	7.748	7.314	6.718	1.081
63 Eu	41.328	47.035	48.526	5.846	6.457	6.843	7.481	8.061	7.620	6.981	1.131
64 Gd	42.768	48.698	50.237	6.058	6.714	7.103	7.786	8.386	7.932	7.243	1.185
65 Tb	44.233	50.380	52.007	6.273	6.978	7.367	8.102	8.717	8.253	7.516	1.240
66 Dy	45.734	52.116	53.790	6.495	7.248	7.636	8.419	9.055	8.583	7.790	1.293
67 Ho	47.268	53.883	55.624	6.720	7.526	7.912	8.747	9.400	8.917	8.068	1.348
68 Er	48.813	55.674	57.480	6.949	7.811	8.189	9.089	9.758	9.262	8.358	1.406
69 Tm	50.421	57.507	59.380	7.180	8.102	8.469	9.426	10.121	9.617	8.650	1.462
70 Yb	52.051	59.380	61.318	7.416	8.402	8.759	9.780	10.491	9.976	8.944	1.522
71 Lu	53.696	61.288	63.290	7.656	8.709	9.049	10.144	10.874	10.345	9.249	1.581
72 Hf	55.400	63.225	65.324	7.899	9.023	9.348	10.516	11.274	10.737	9.558	1.645
73 Ta	57.110	65.221	67.420	8.146	9.343	9.652	10.896	11.682	11.133	9.877	1.710
74 W	58.872	67.237	69.498	8.398	9.673	9.962	11.286	12.100	11.539	10.200	1.776
75 Re	60.658	69.304	71.668	8.653	10.010	10.276	11.686	12.531	11.955	10.531	1.843
76 Os	62.492	71.420	73.845	8.912	10.355	10.599	12.096	12.972	12.381	10.868	1.914
77 Ir	64.341	73.582	76.111	9.175	10.709	10.921	12.512	13.424	12.820	11.212	1.980
78 Pt	66.267	75.739	78.372	9.443	11.071	11.251	12.942	13.883	13.273	11.563	2.050
79 Au	68.199	77.978	80.719	9.714	11.443	11.585	13.382	14.353	13.736	11.922	2.123
80 Hg	70.167	80.249	83.100	9.989	11.823	11.924	13.830	14.843	14.215	12.287	2.195
81 Tl	72.168	82.602	85.507	10.269	12.214	12.272	14.292	15.343	14.701	12.661	2.271
82 Pb	74.243	84.921	87.995	10.552	12.614	12.623	14.765	15.855	15.205	13.041	2.346
83 Bi	76.345	87.313	90.566	10.839	13.024	12.980	15.248	16.376	15.720	13.427	2.423
84 Po	78.472	89.779		11.131	13.447	13.340	15.744				
85 At	80.614	92.319		11.427	13.876		16.252				
86 Rn	82.878	94.862		11.728	14.315		16.771				
87 Fr	85.096	97.473		12.032	14.771	14.450	17.304				
88 Ra	87.437	100.149		12.341	15.235	14.841	17.850				
89 Ac	89.779	102.807		12.653	15.714		18.409				
90 Th	92.182	105.609	109.624	12.969	16.203	15.625	18.984	20.463	19.683	16.299	2.996
91 Pa	94.645	108.473		13.292	16.703	16.025	19.568	21.172	20.362	16.768	3.083
92 U	97.167	111.297	115.658	13.616	17.220	16.428	20.167	21.771	20.947	17.165	3.171
93 Np	99.427	113.748		13.945	17.750	16.841	20.785				
94 Pu											
95 Am											
96 Cm											
97 Bk											
98 Cf											
99 Es											
100 Fm											
101 Md											
102 No											
103 Lr											

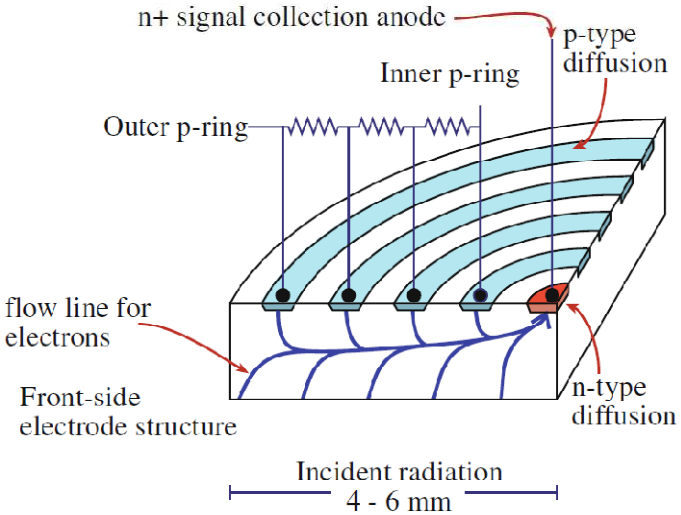
SHIMADZU
Solutions for Science
since 1875

Silicon Drift Detector (SDD)

- Resolução de 123 eV
- 100.000 cts

Williams e Carter, 2009



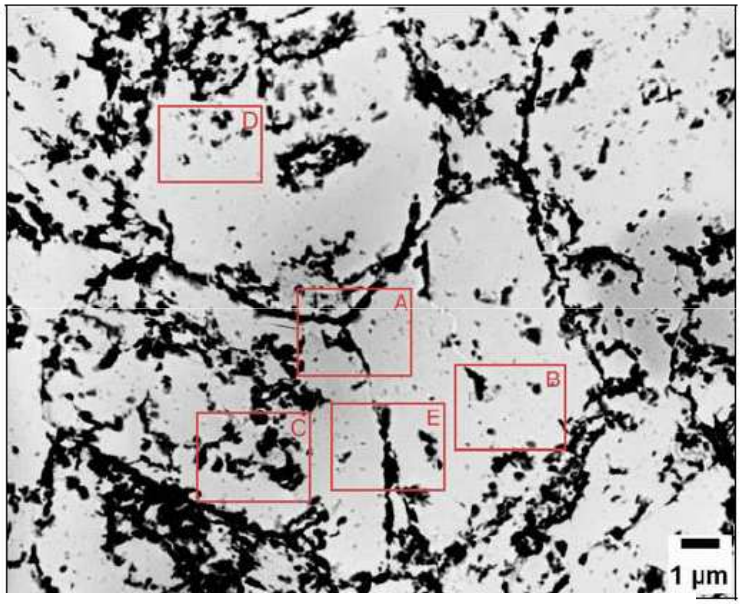


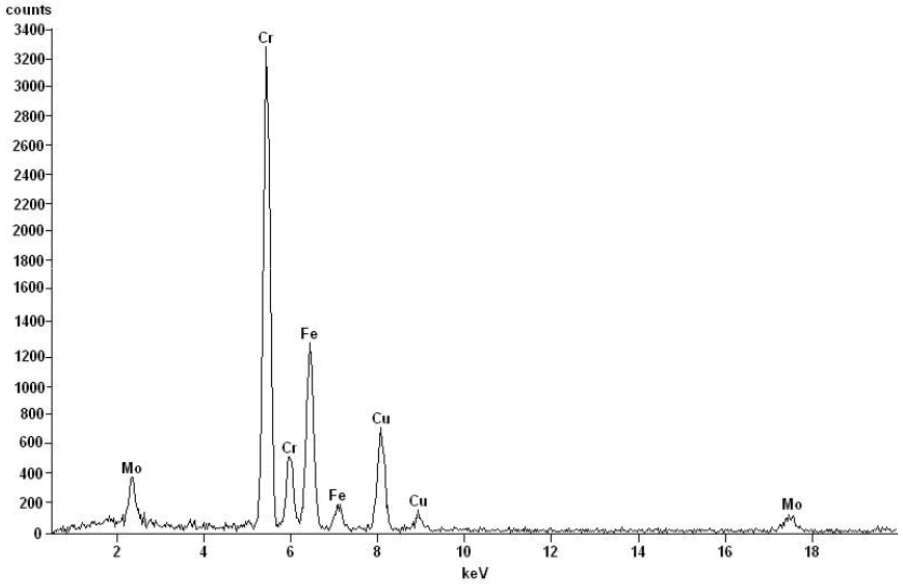


Bruker

X-Ray Energy Dispersive Spectroscopy (EDS)

Réplica de uma amostra de aço 2 1/4Cr 1 Mo com precipitados de M_7C_3.





Engineering Failure Analysis 16 (2009) 1493–1500

Contents lists available at ScienceDirect

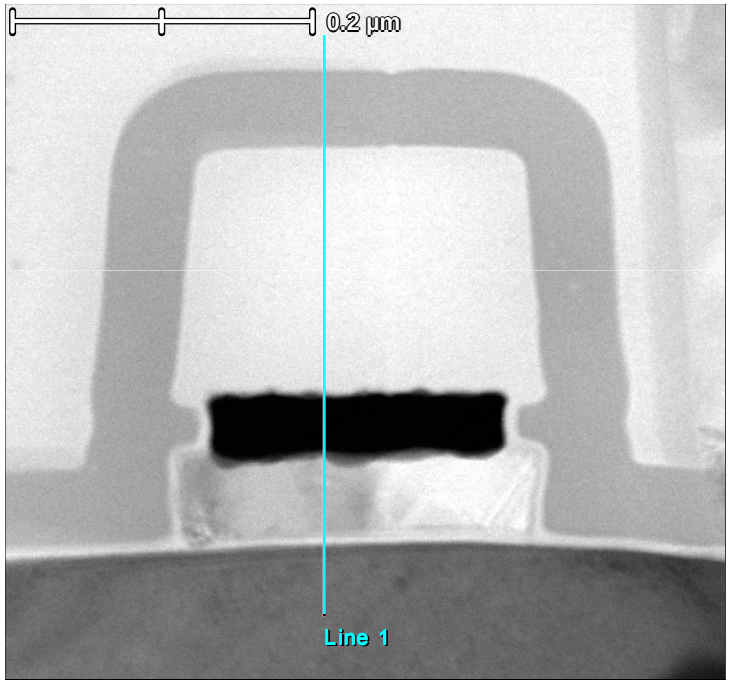
Engineering Failure Analysis

journal homepage: www.elsevier.com/locate/engfailanal

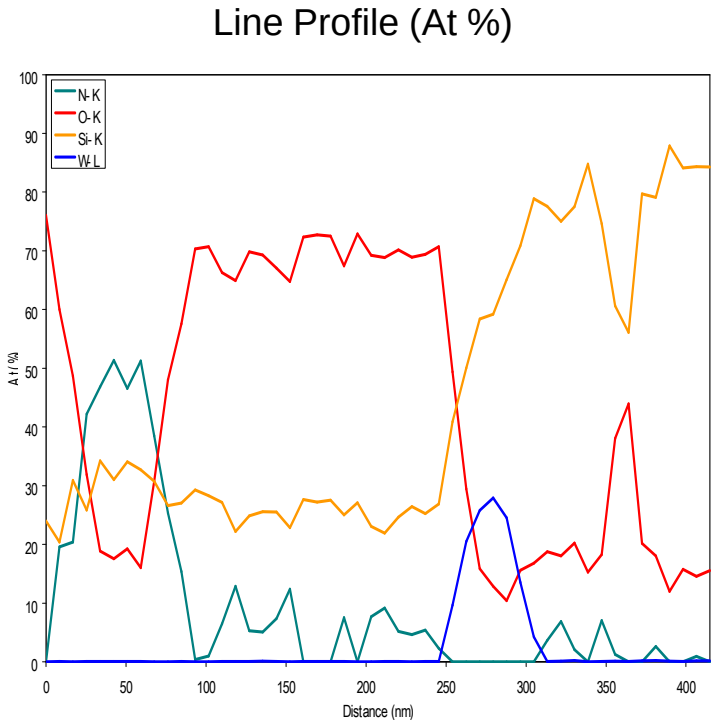
Quantitative observations of precipitation in 2.25Cr–1Mo steel exposed to different creep conditions in a power station

C.R. de Lima[a], A.L. Pinto[a], H.C. Furtado[b], L.H. de Almeida[c,*], M.F.P. de Souza[c], I. Le May[d]

Perfil de Linha



STEM BF image

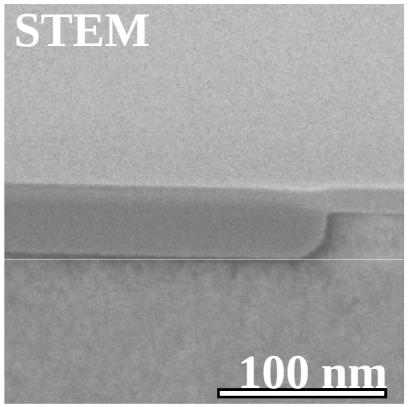


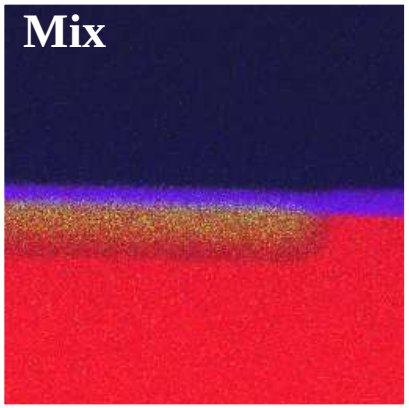
Specimen : 64MB DRAM

Jeol

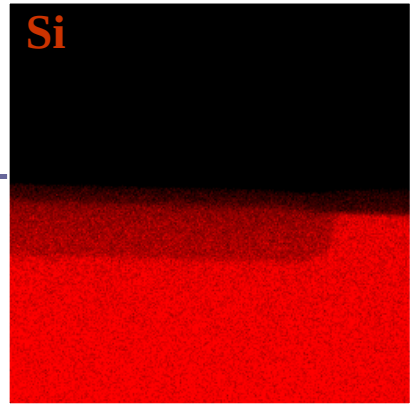
Mapeamento

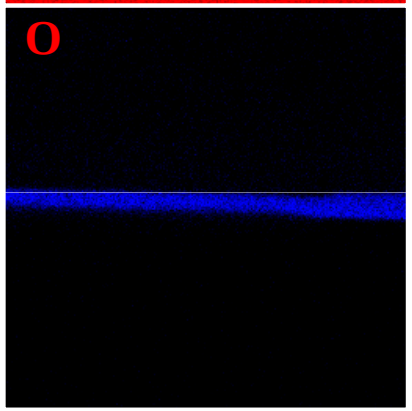
As doping:
25keV, $5e^{15}/cm^2$
No annealing process
256x256, x 300,000, 60 min

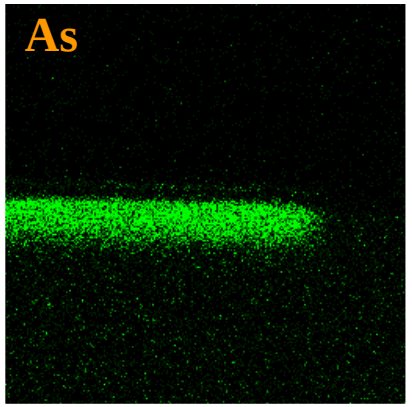




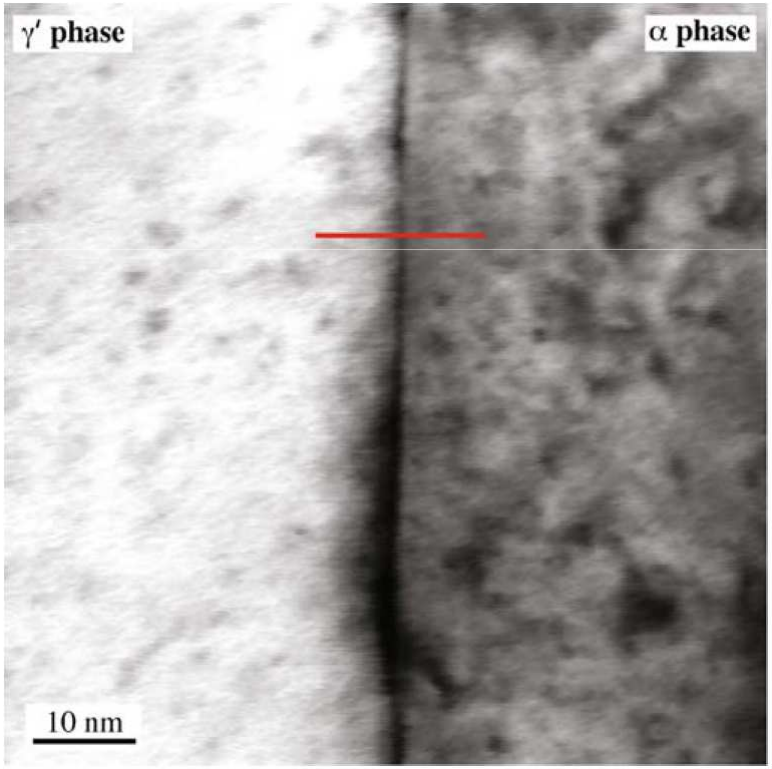
Jeol

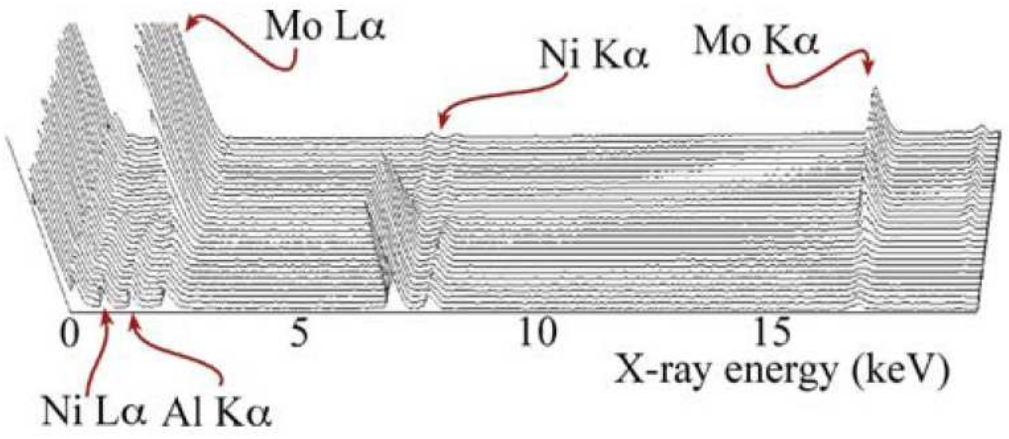






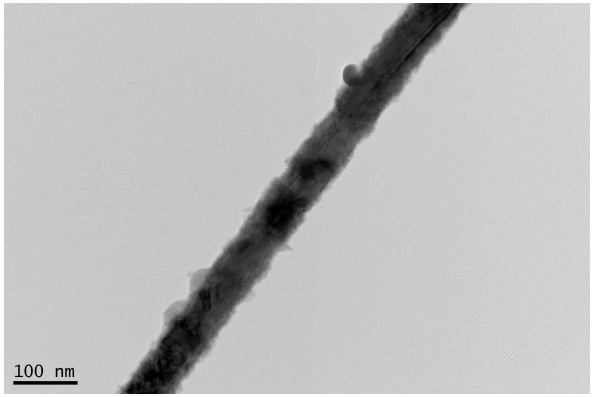
Coleta de Data Cube

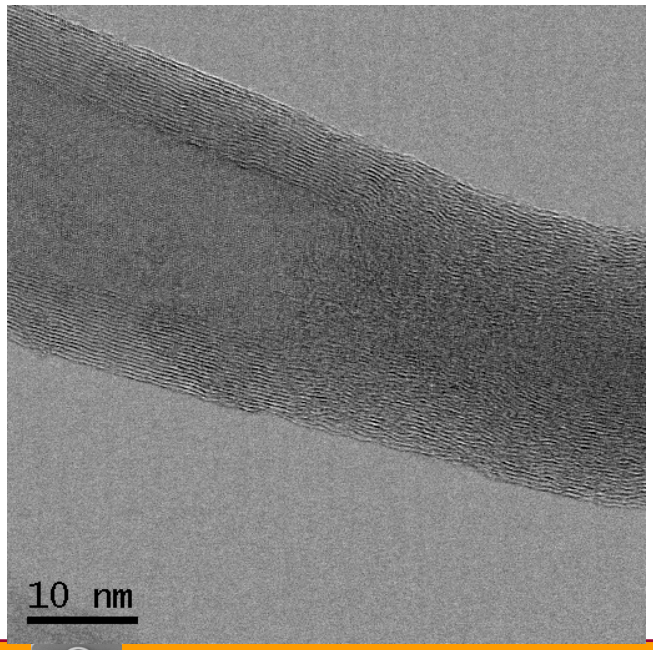


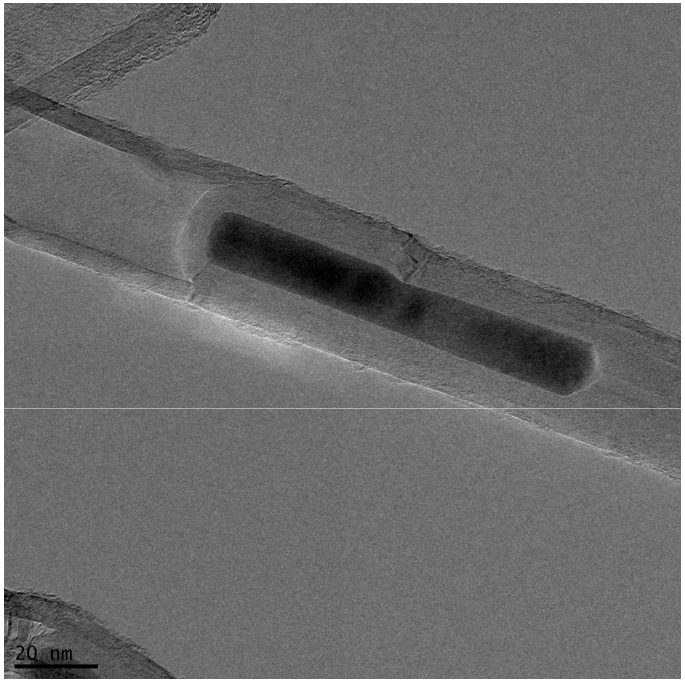


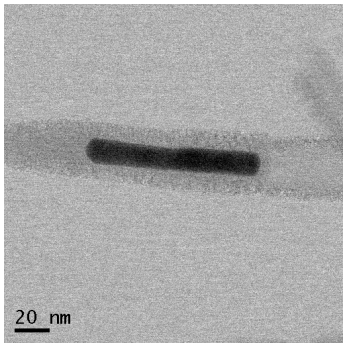
Williams e Carter, 2009

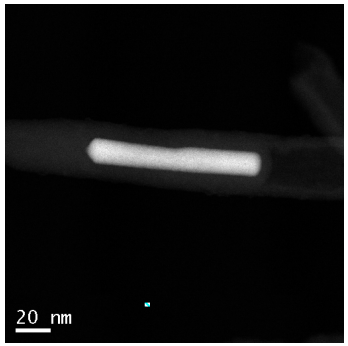
Nanotubos de C dopados com P





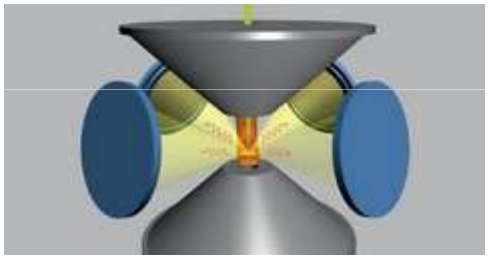


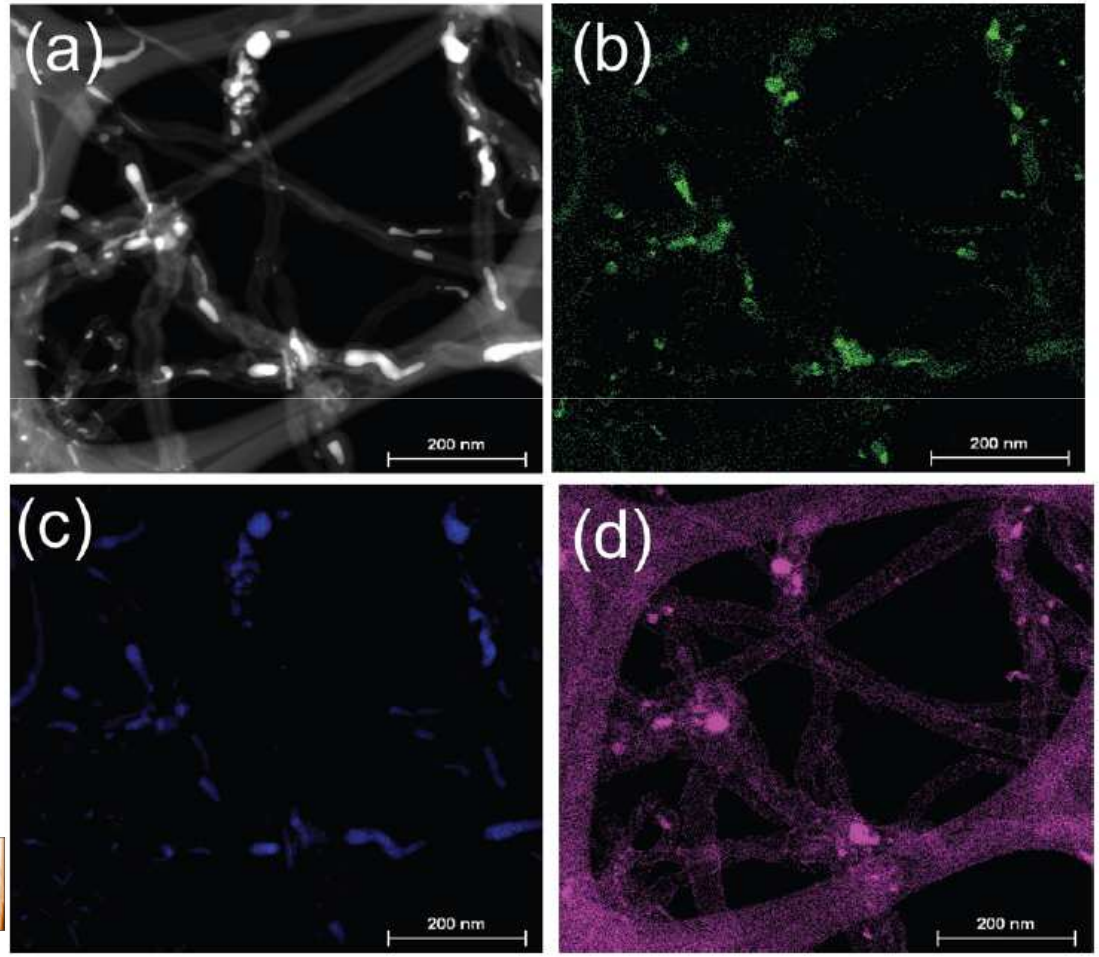




Mapeamento por EDS
Nanotubos de C dopados com P

Equipamento:
FEI Titan G2 com tecnologia ChemiSTEM





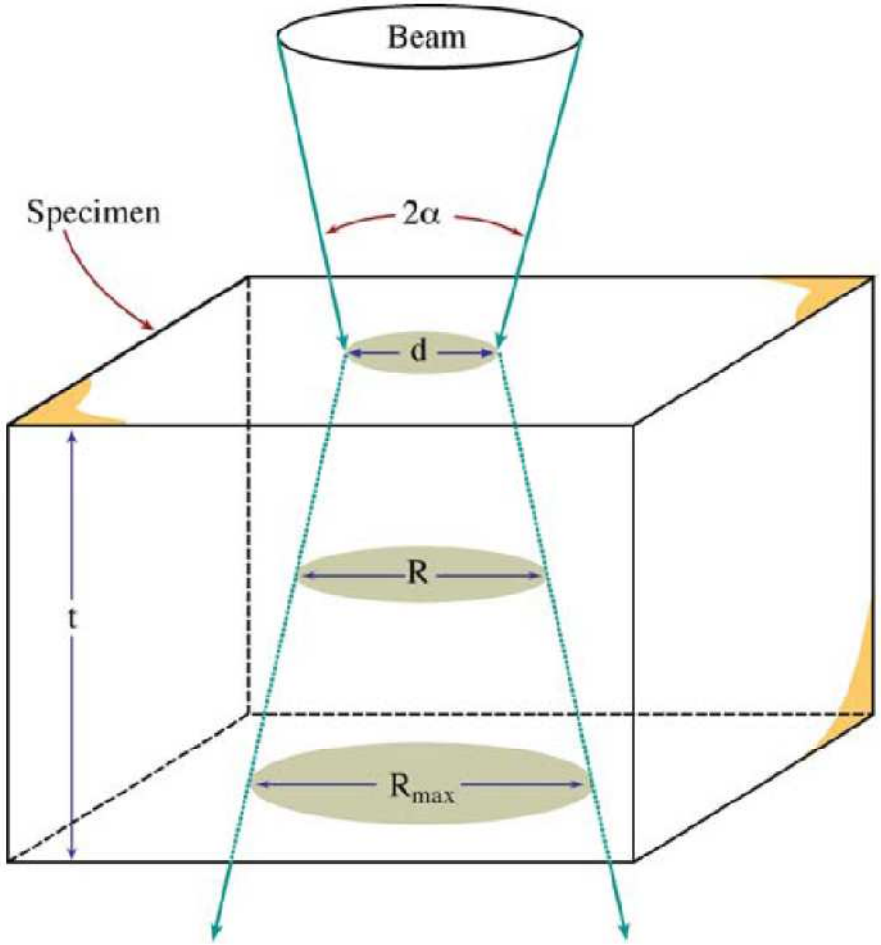
AIP | Journal of Applied Physics

Characterization of phosphorus-doped multiwalled carbon nanotubes

D. G. Larrude, M. E. H. Maia da Costa, F. H. Monteiro, A. L. Pinto, and F. L. Freire

J. Appl. Phys. **111**, 064315 (2012)

Resolução Espacial



Resolução

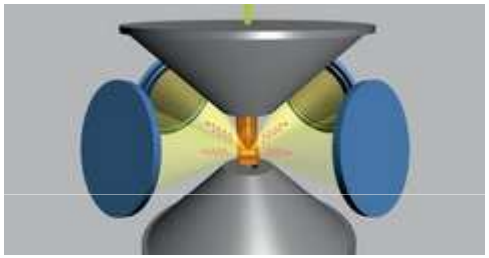
$$R_{Max} = \left(b^2 + d^2\right)^{\frac{1}{2}}$$

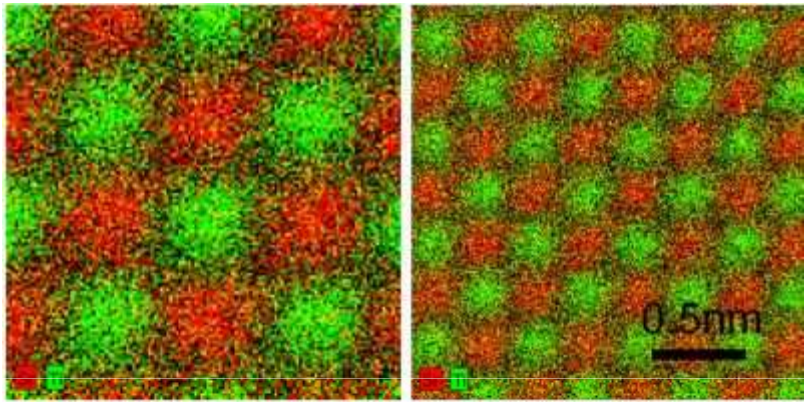
$$R = \frac{d + R_{Max}}{2}$$

Williams e Carter, 2009

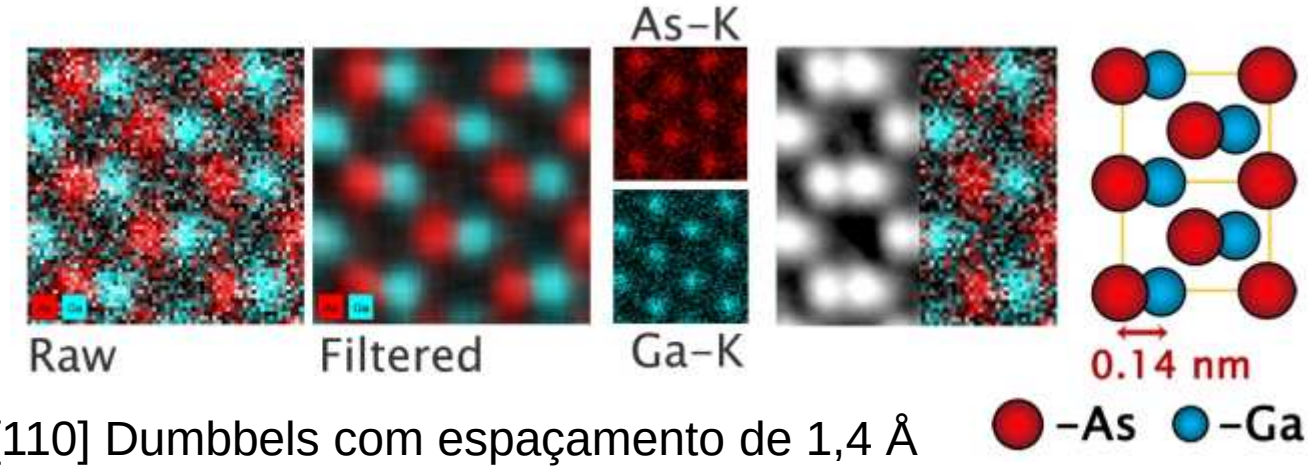
EDS com Resolução Atômica

Equipamento:
FEI Titan G2 com tecnologia ChemiSTEM



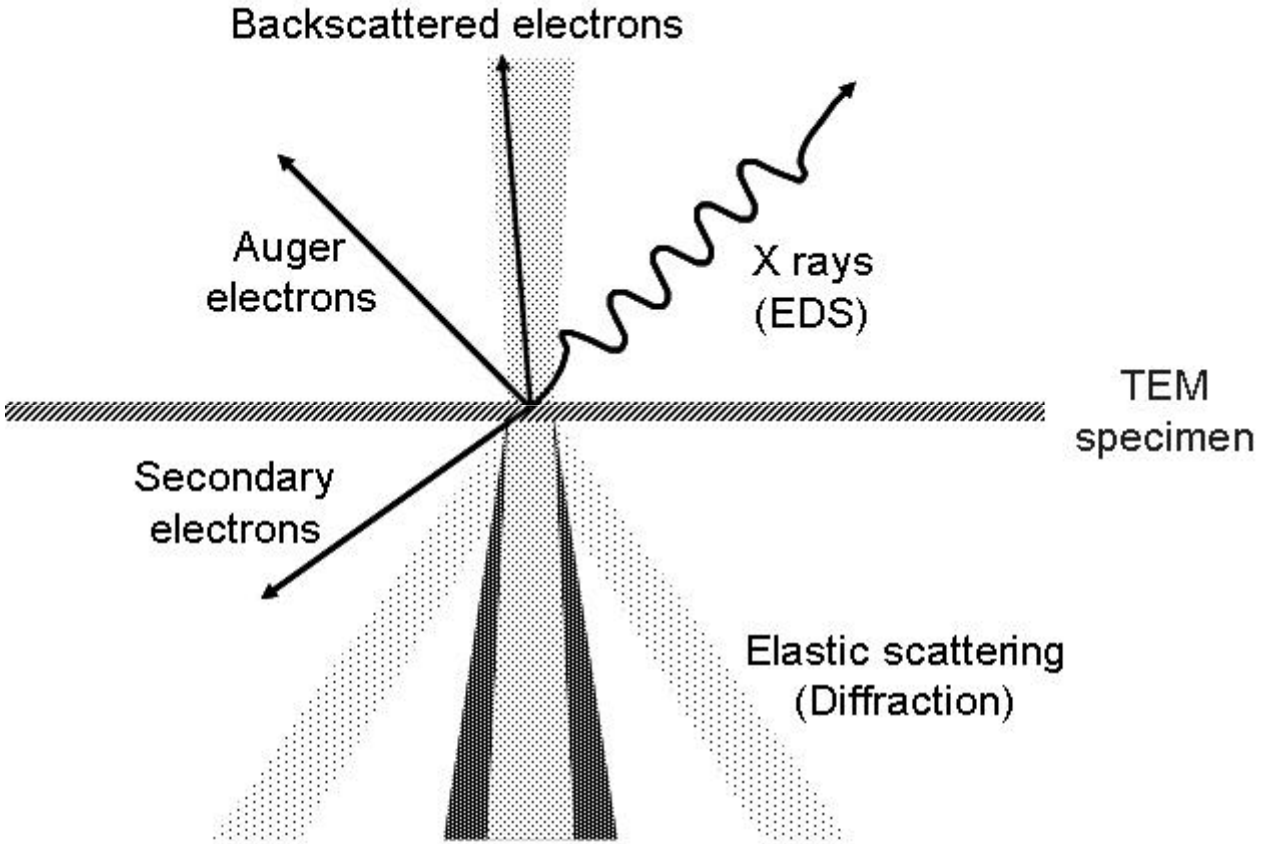


Titanato de estrôncio (0,075 Å/pixel)

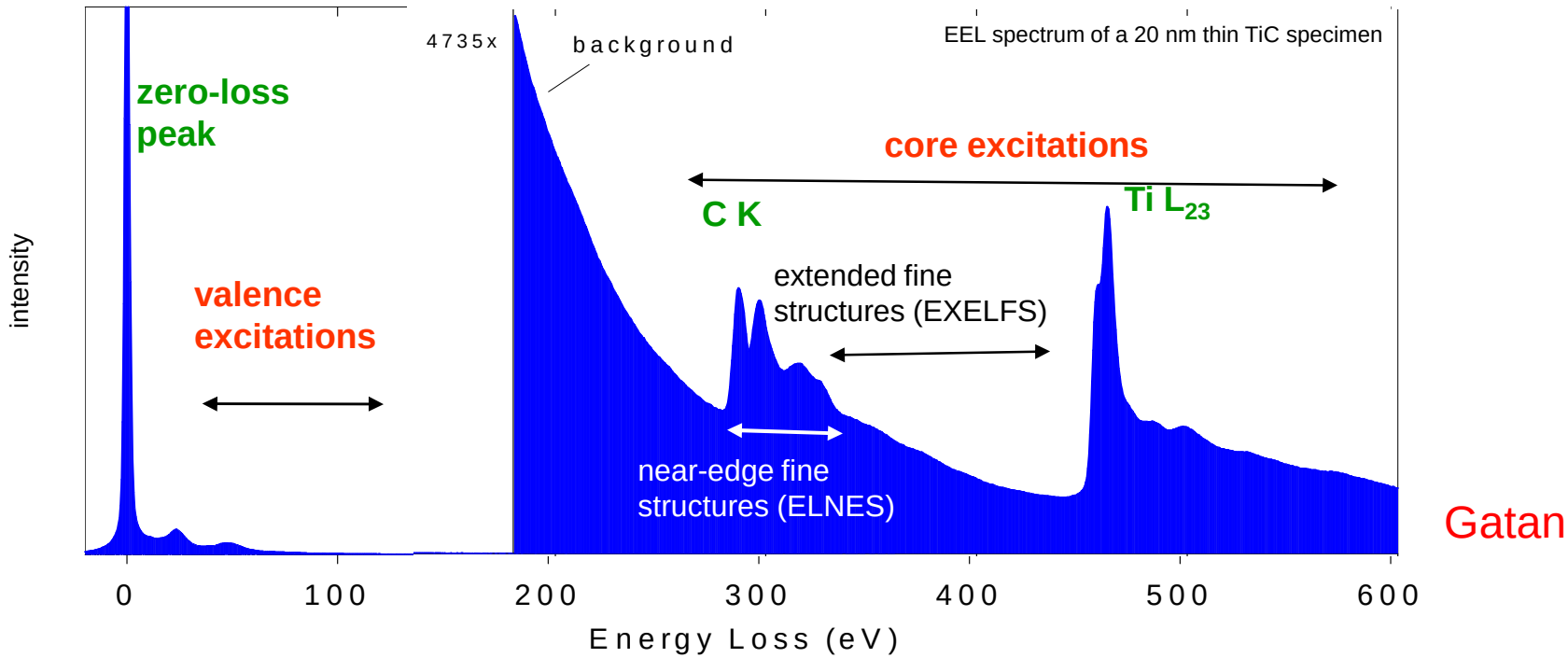


GaAs [110] Dumbbels com espaçamento de 1,4 Å

Electron Energy-Loss Spectroscopy (EELS)



EELS



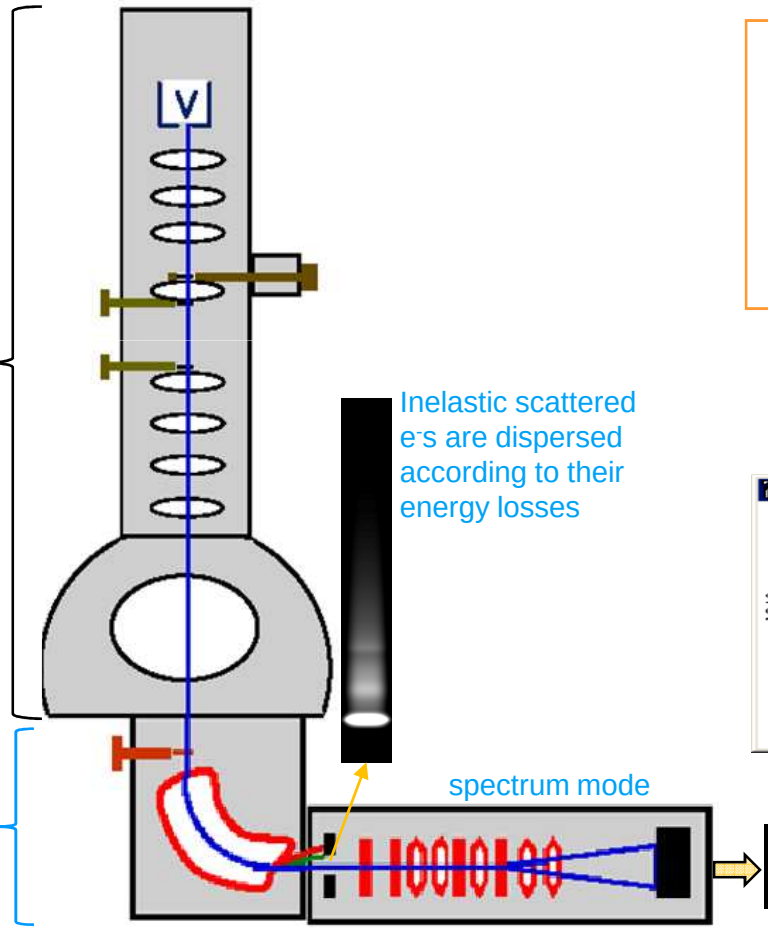
Gatan

- Zero loss peak / plasmon peak: espessura da amostra
- Valence excitations: densidade eletrônica das bandas de condução/valência, medida de band gap, efeitos de polarização, efeitos dielétricos
- Core excitations: Identificação e quantificação de elementos, investigação do ambiente eletrônico incluindo número de coordenação, estado de valência e tipo de ligação atômica
- Mapeamento elementar

EELS

Microscope column

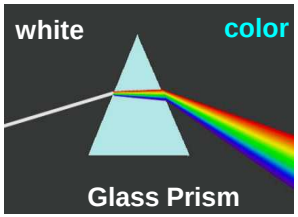
Post-column spectrometer

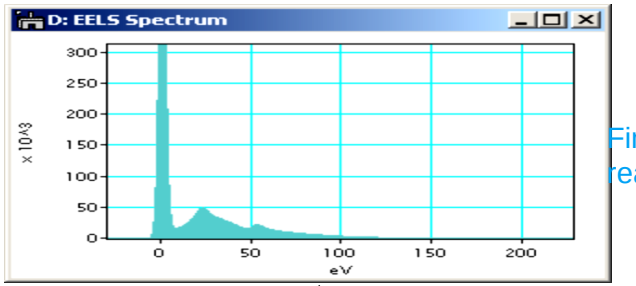


Inelastic scattered e⁻s are dispersed according to their energy losses

spectrum mode

Simply speaking, the major function of an EELS Spectrometer (GIF/PEELS) is dispersing the scattered electrons according to their lost energies into a spectrum.





Final EELS readout

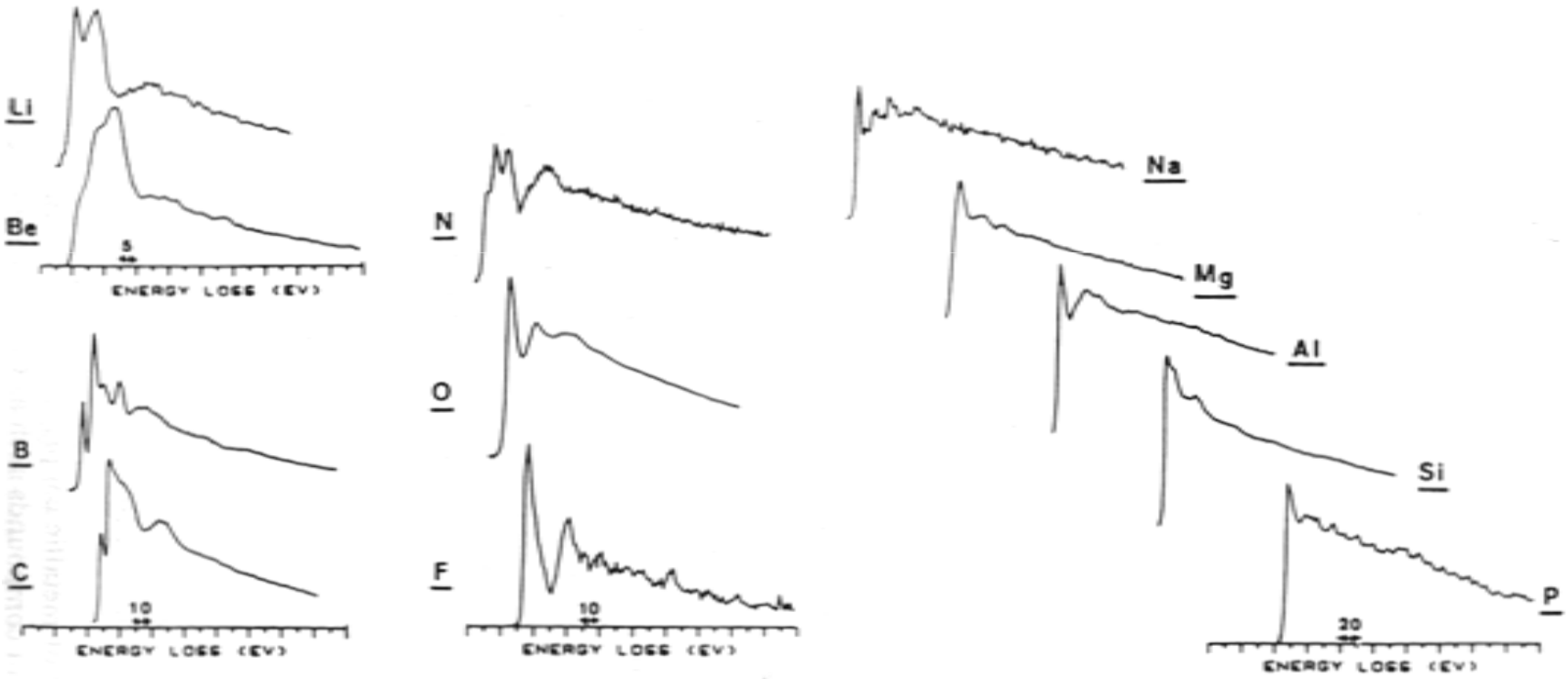
EELS spectrum projected onto CCD



Gatan

EELS

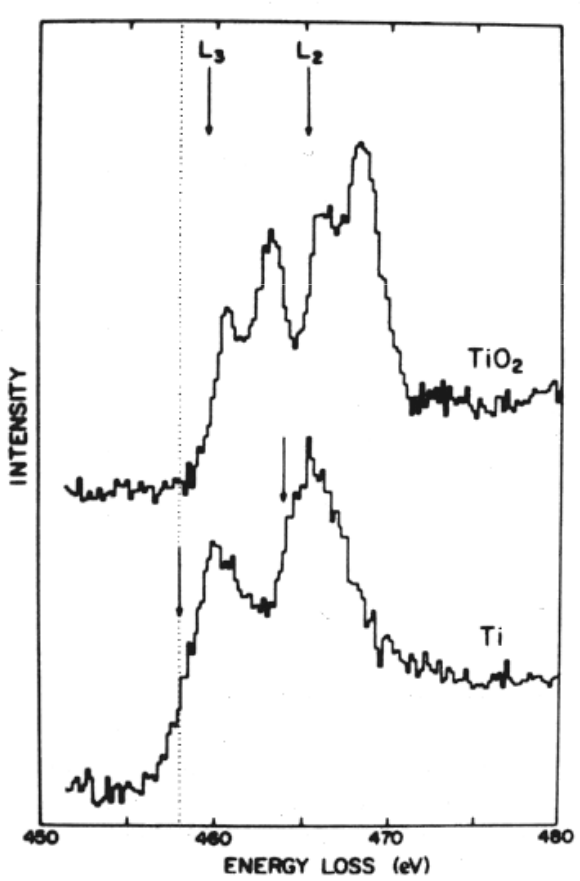
Sensibilidade à composição química



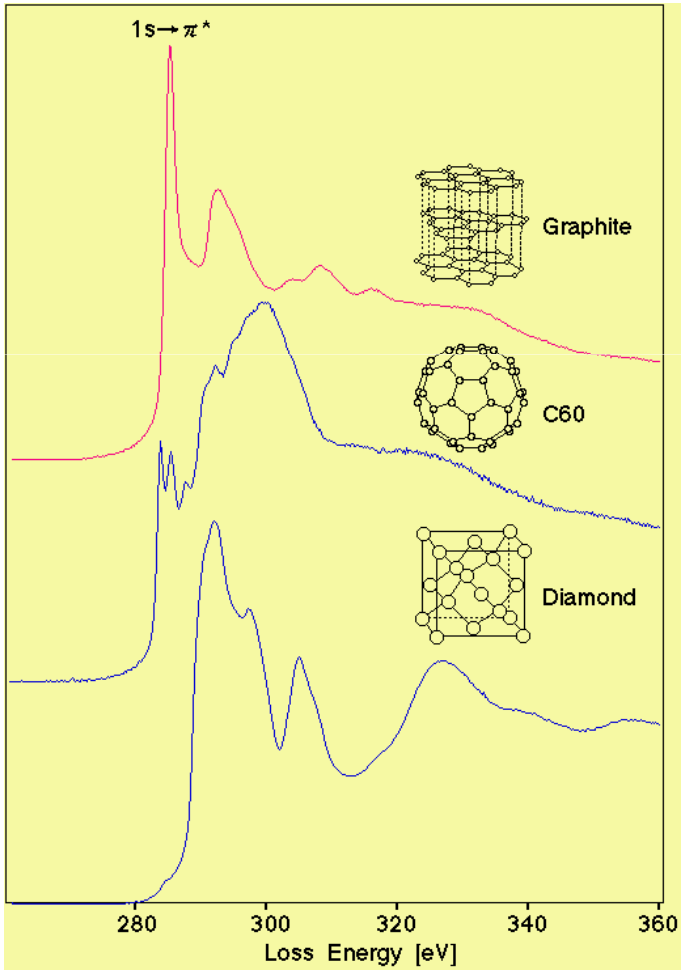
Gatan

EELS

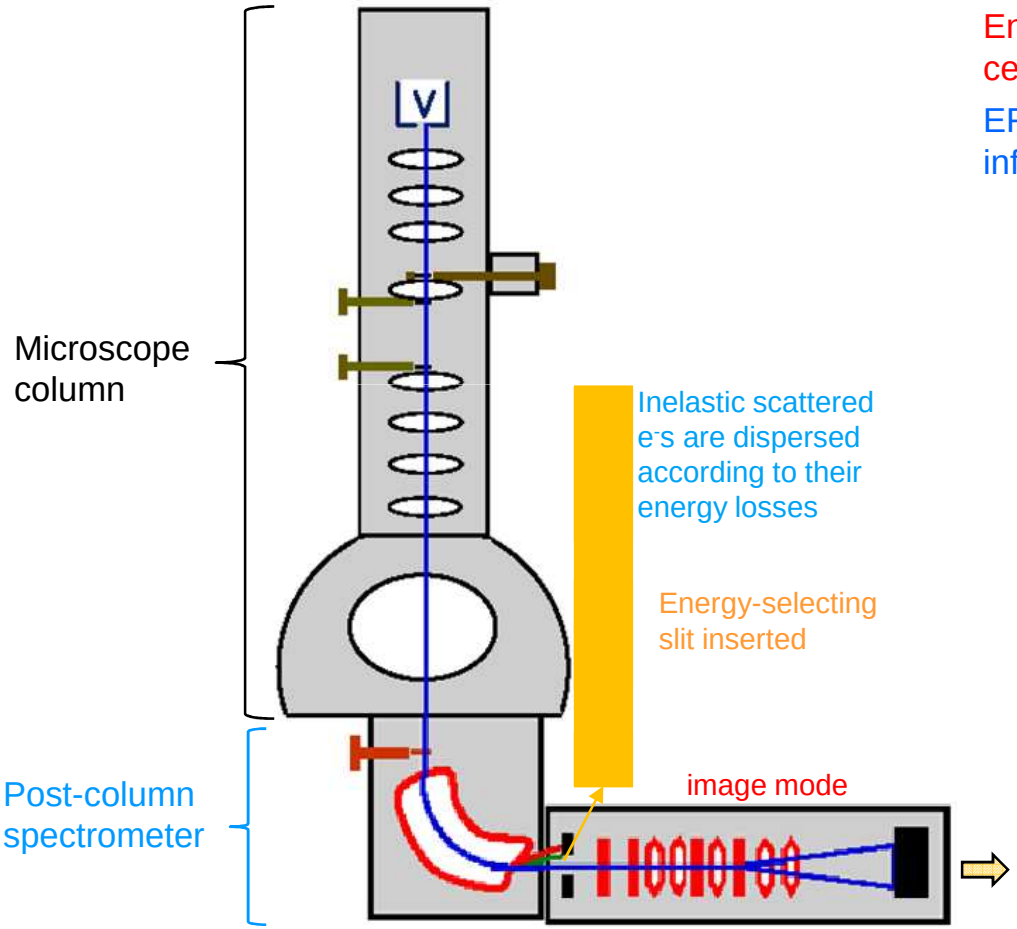
Sensibilidade ao estado de oxidação



Gatan



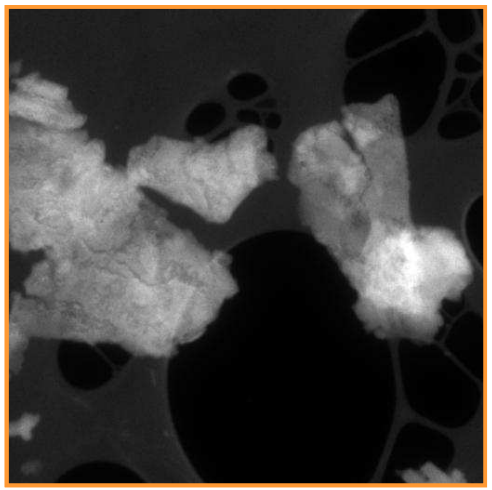
Imageamento por EELS



Energy filtered TEM (EFTEM): select the electrons with certain energy losses for imaging.

EFTEM has many uses, based on the wealthy information on EELS :

- Contrast enhancement in imaging & diffraction
  - zero-loss filtering; most probable loss imaging; contrast tuning; pre-carbon imaging
- Elemental mapping/Jump ratio imaging
  - 3 window method; 2 window method
- Chemical mapping

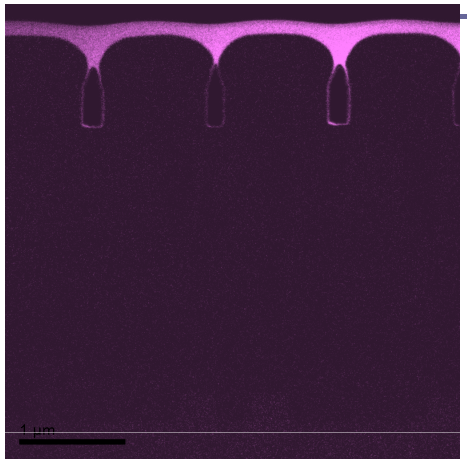


Zero loss filtered image projected onto CCD

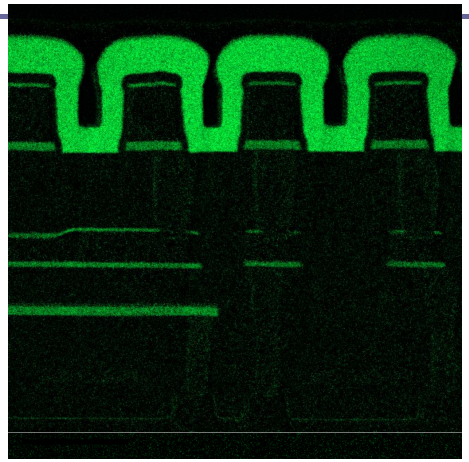
Gatan

Imageamento por EELS

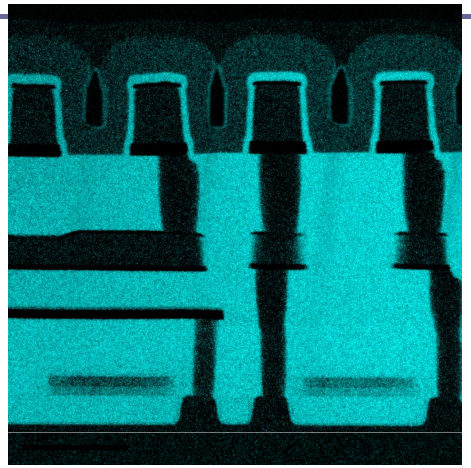
C-K map



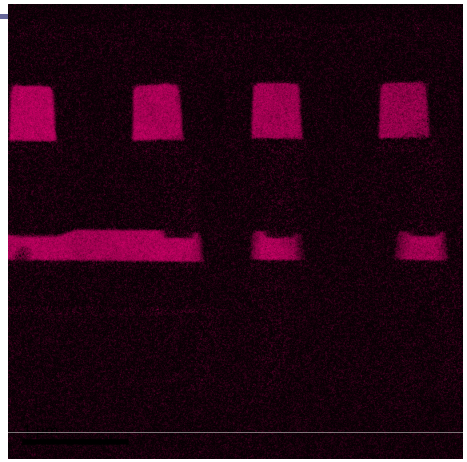
N-K map



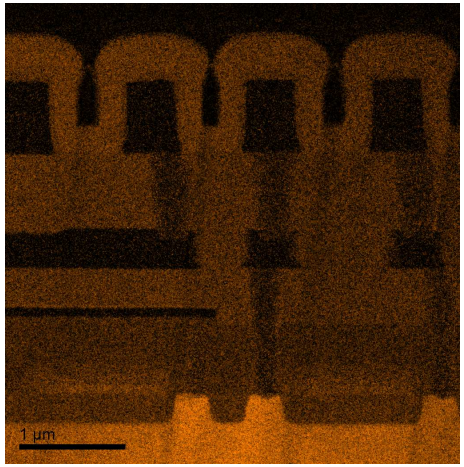
O-K map



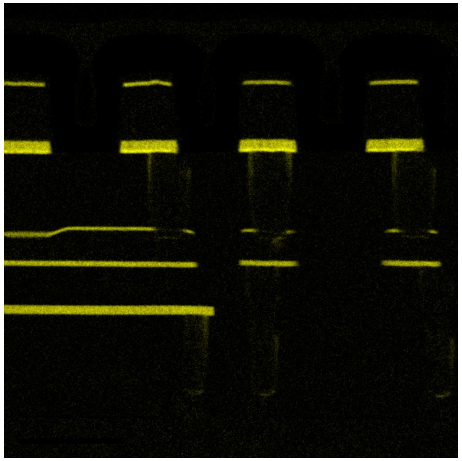
Al-K map



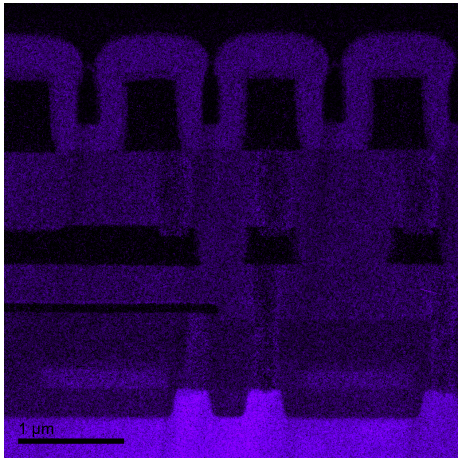
Si-K map



Ti-L2,3 map



W-M map



Overlap all Element

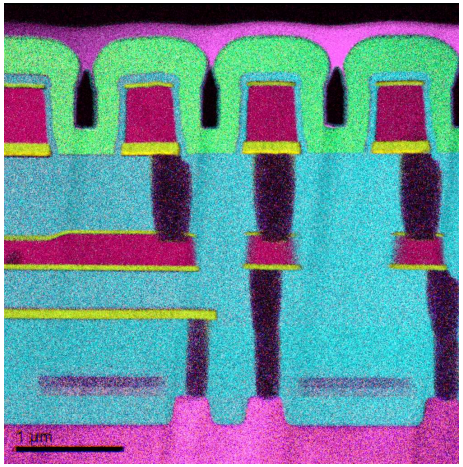


Image size : 1024 x 1024 pixels

Specimen : SRAM

Jeol

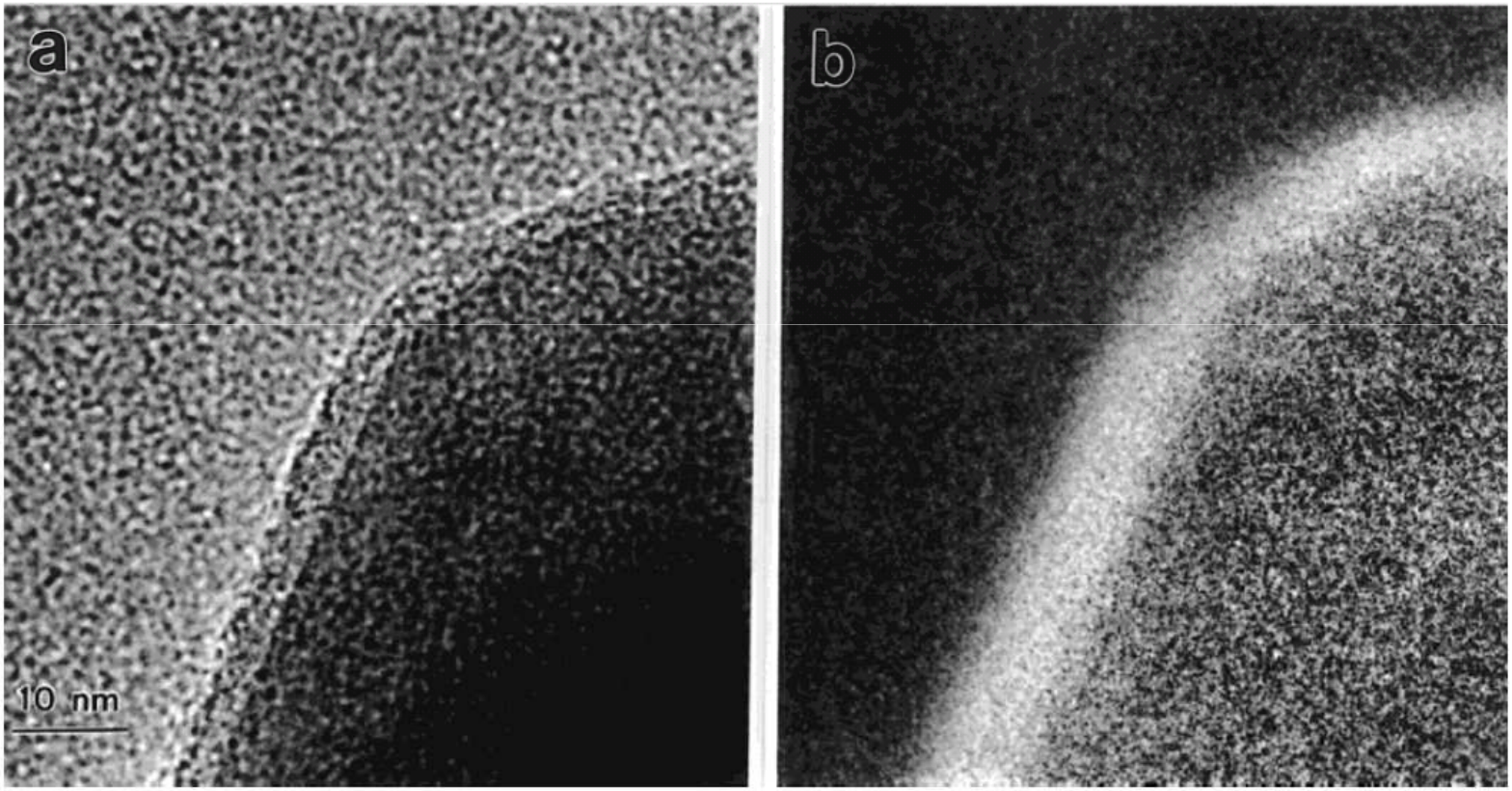
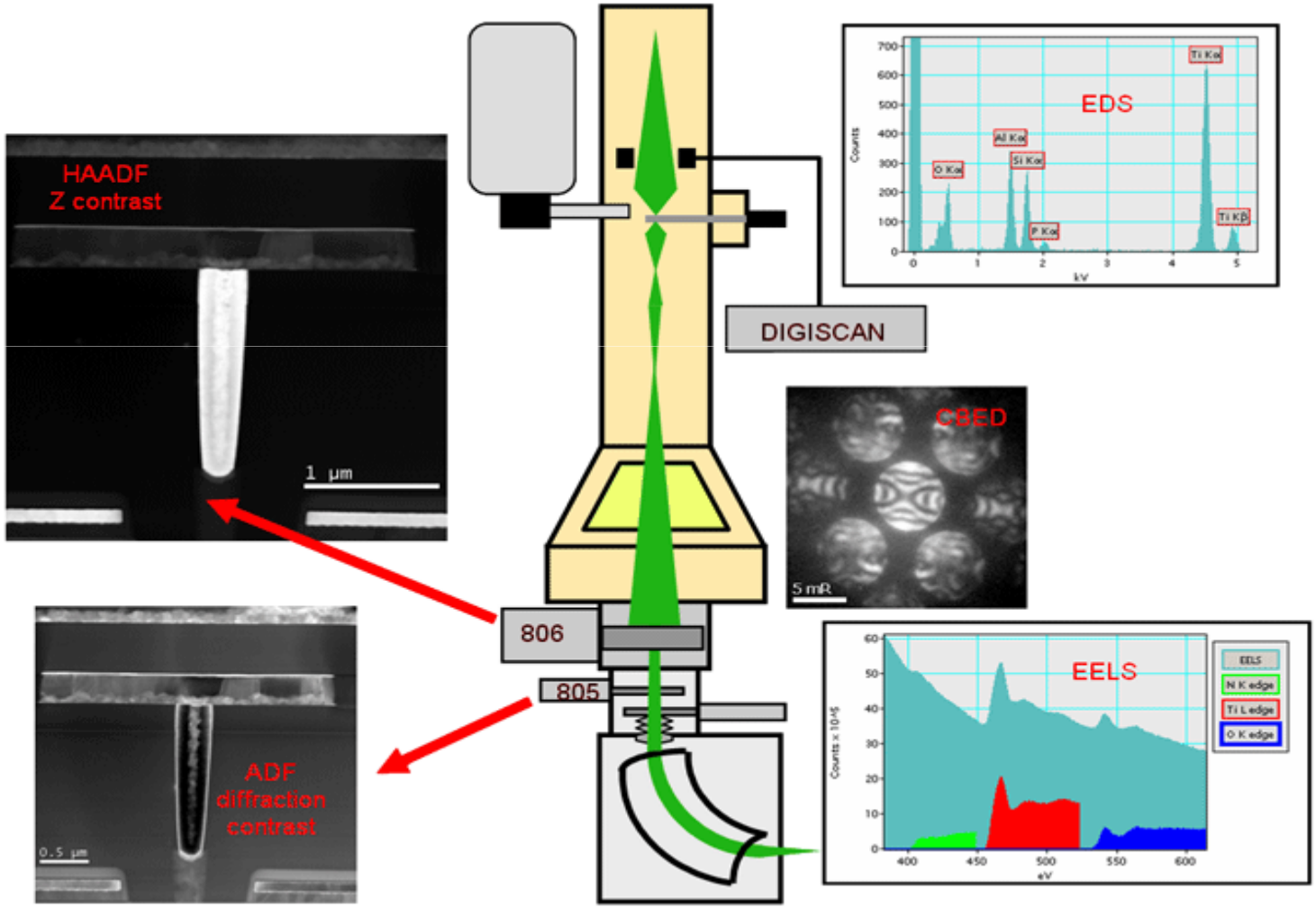


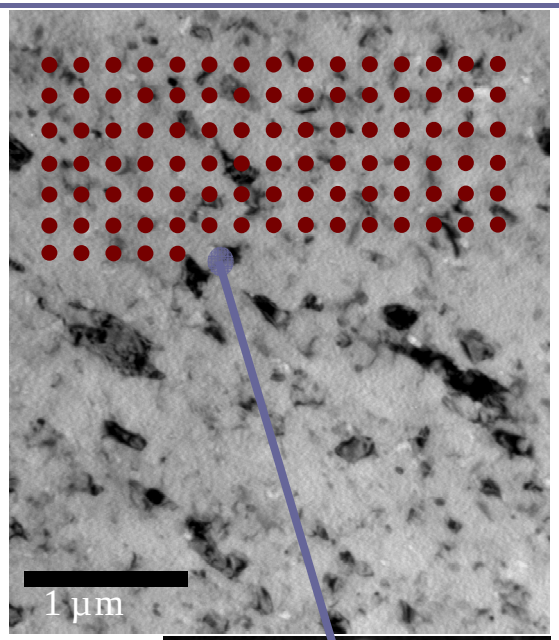
Figure 25. (a) Bright-field and (b) Si-L edge energy filtered TEM images of a TiO_2 particle coated with silica.

J. Phys. Chem. B, Vol. 104, No. 6, 2000

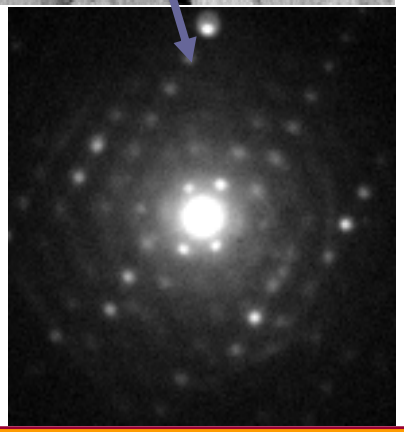
Colocando toda a capacidade analítica em um só microscópio



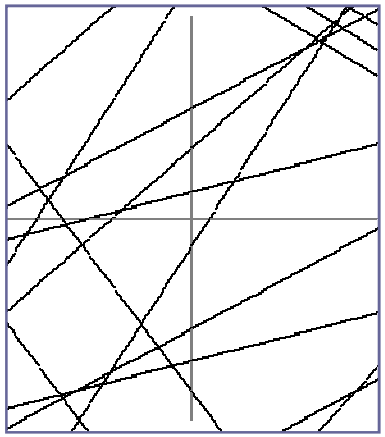
Coleta Automática de Padrões de Difração



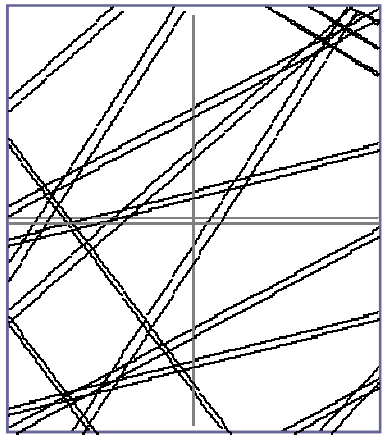
Severely deformed 7075 Al. Alloy



Kikuchi pattern

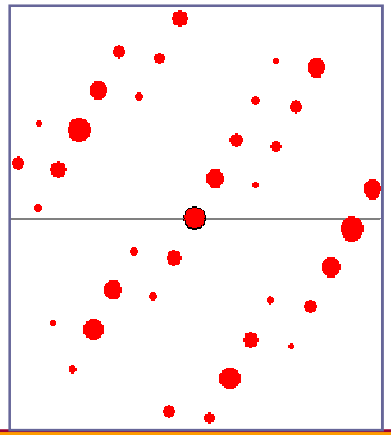


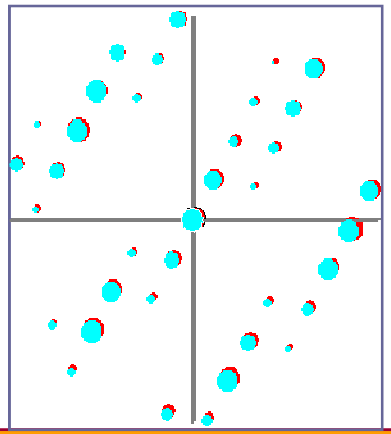
Orientation **Ω**



Orientation **Ω + Ω'(= Ω +0.1°)**

Bragg Spot pattern



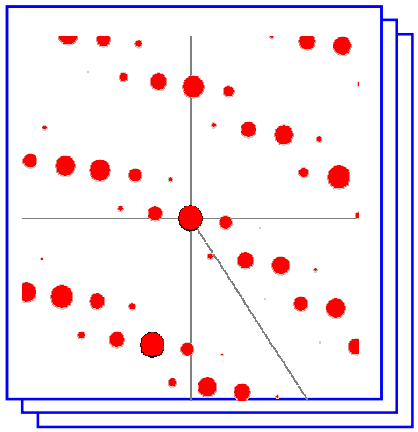


Nanomegas
Grenoble INP

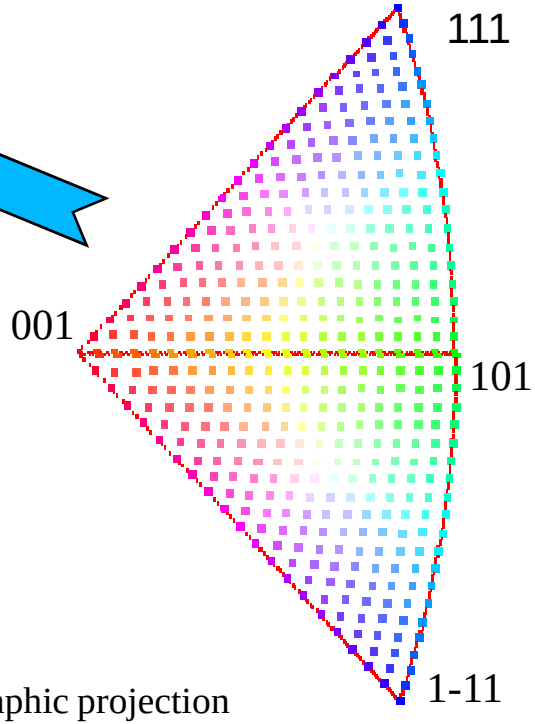
Diffraction Pattern Identification

Nanomegas/Grenoble INP

Pre-calculated templates



Template generation of all possible simulated orientations (every1º) within stereographic triangle for given crystal lattice(s) and symmetry

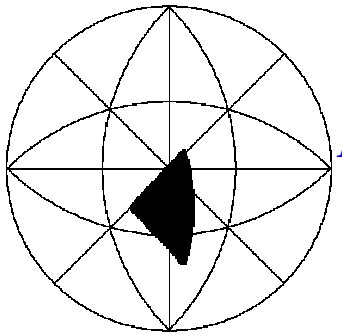


Stereographic projection

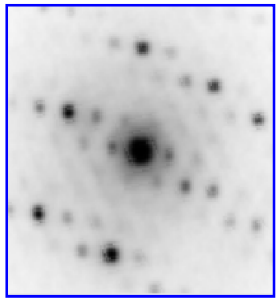
(example ,cubic) **~2000 simulated patterns**

$$Q(i) \sim \sum_{j=1}^{m} P(x_j,y_j)\, T_i(x_j,y_j)$$

Correlation index

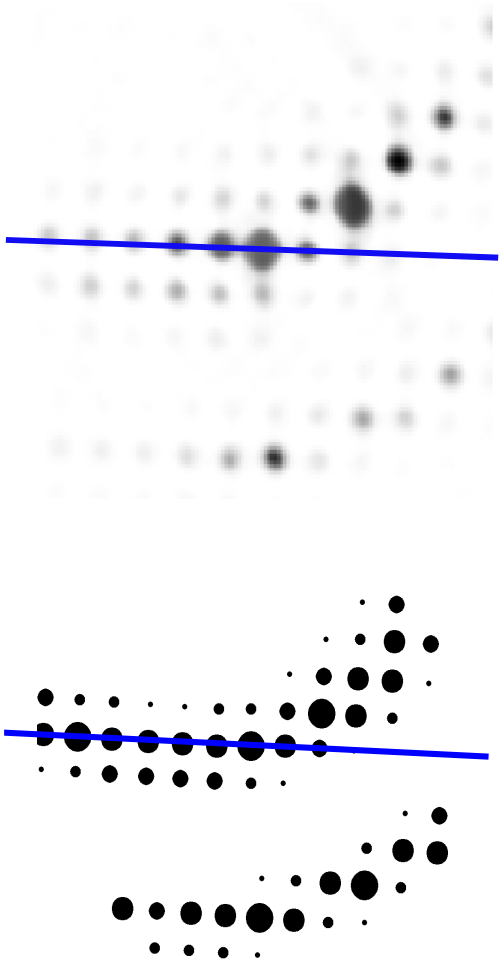


Acquired pattern

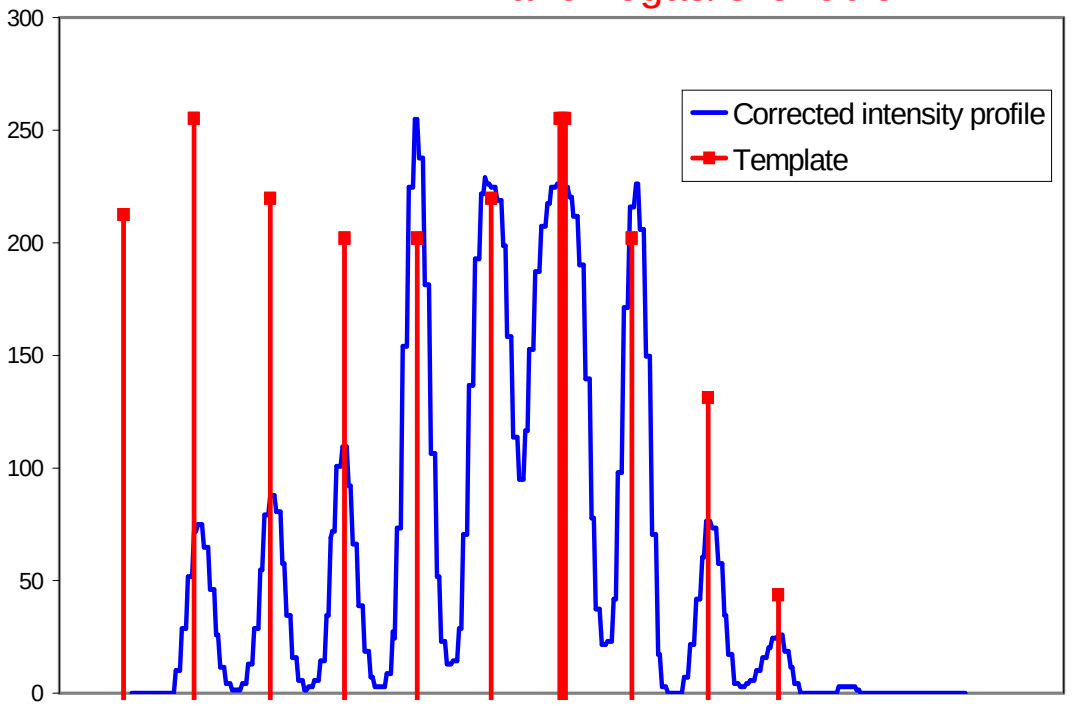


Degree of matching between experimental patterns and simulated templates is given by a correlation index ; highest value corresponds to the adequate orientation/phase

Index Calculation



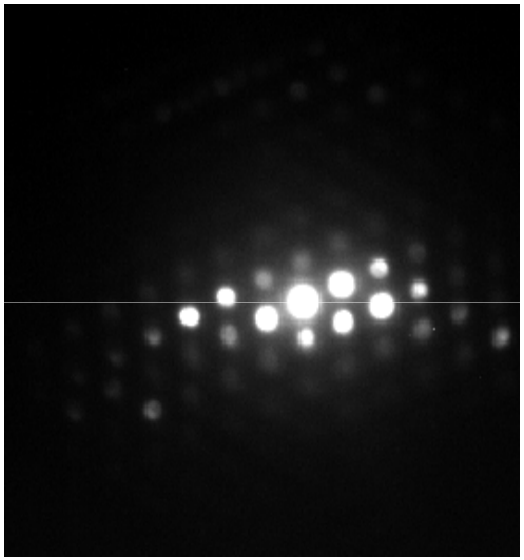
Nanomegas/Grenoble INP



$$Q(i) = \frac{\sum_{j=1}^{m} P(x_j,y_j)\, T_i(x_j,y_j)}{\sqrt{\sum_{j=1}^{m} P^2(x_j,y_j)}\ \sqrt{\sum_{j=1}^{m} T_i^2(x_j,y_j)}}$$

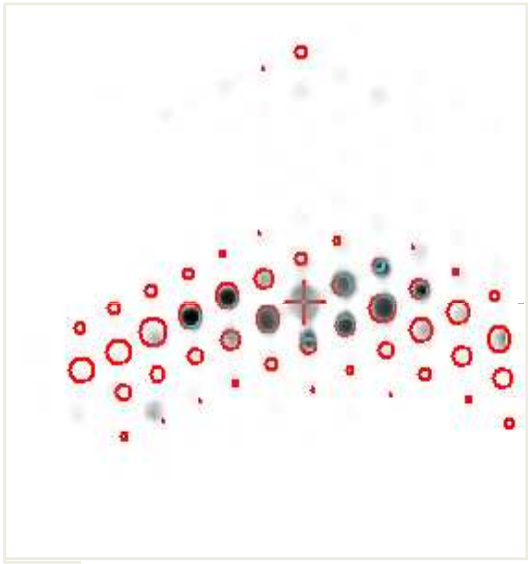
ASTAR identification example : nanocrystalline Cu

Nanomegas/Grenoble INP

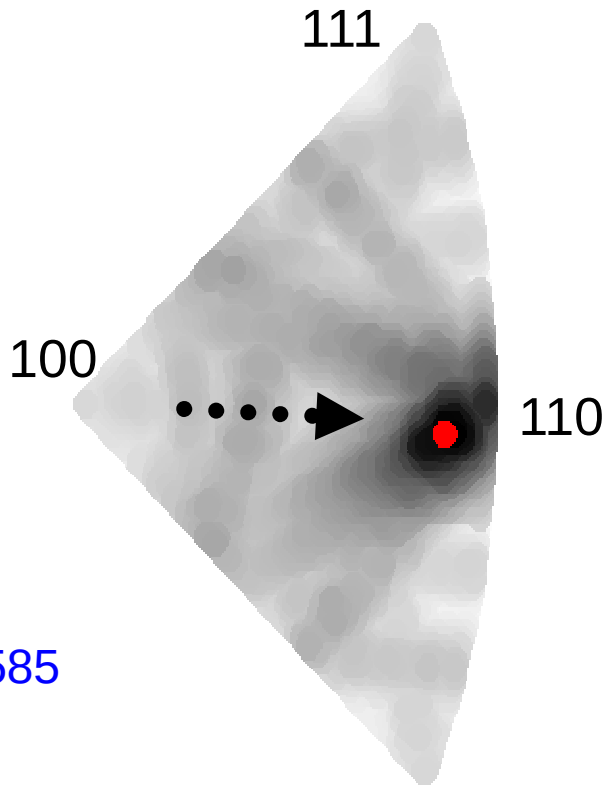


Diffraction pattern

(nanocrystalline cubic copper)



correlation index = 585

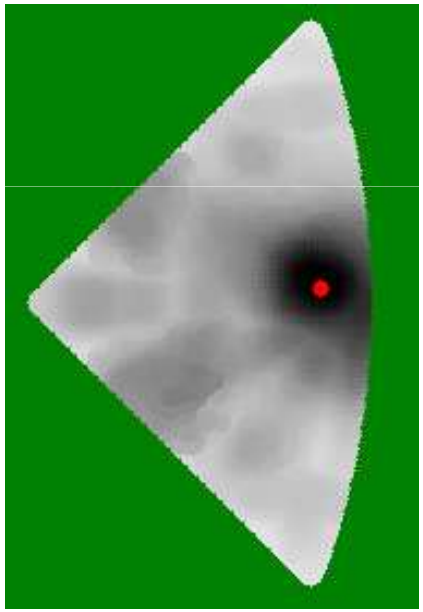


Correlation index map

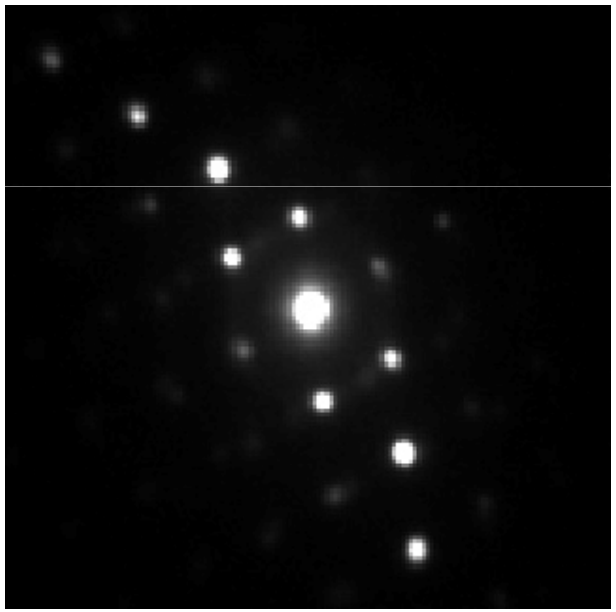
For a given ED pattern, the correlation index map is calculated for all possible template orientations and plotted on a map that represents a portion of the stereographic projection (reduced to a double standard triangle). That resulting map reveals the most probable orientation for every experimental spot ED pattern (in this case ED pattern is found to be close to 110 ZA orientation)

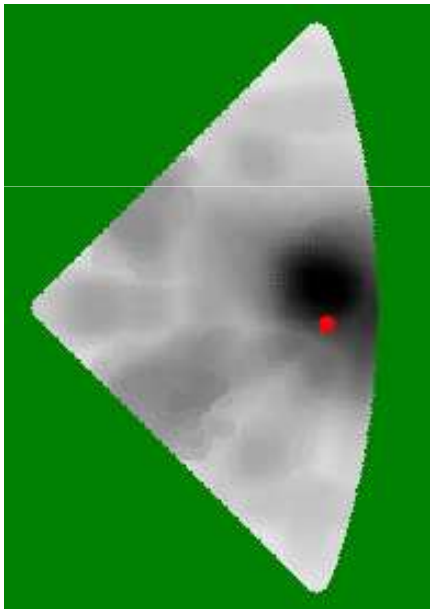
Crystallographic Orientation Identification

Q map over stereographic projection



Diffraction pattern





γ phase in Ni Superalloy

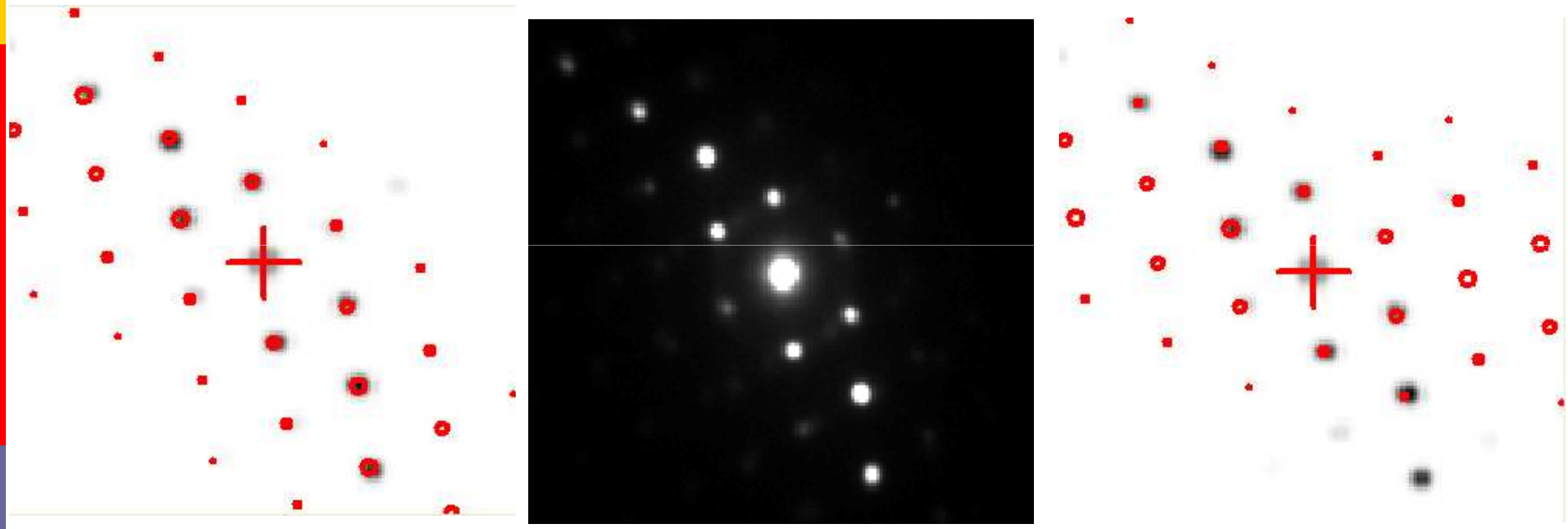
$$R = 100\,(1 - Q_2/Q_1)$$

Reliability

Crystallographic Orientation Identification

Q_1 = 836

Q_2 = 590

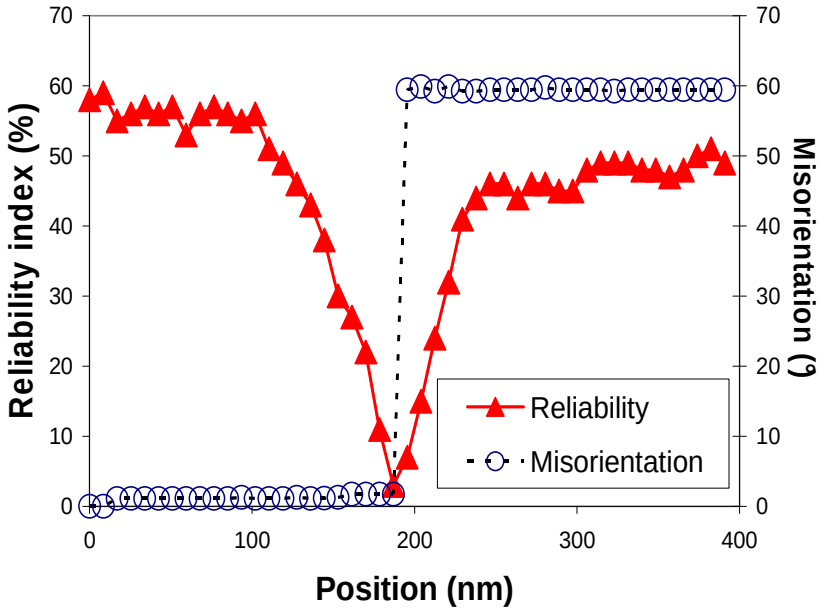


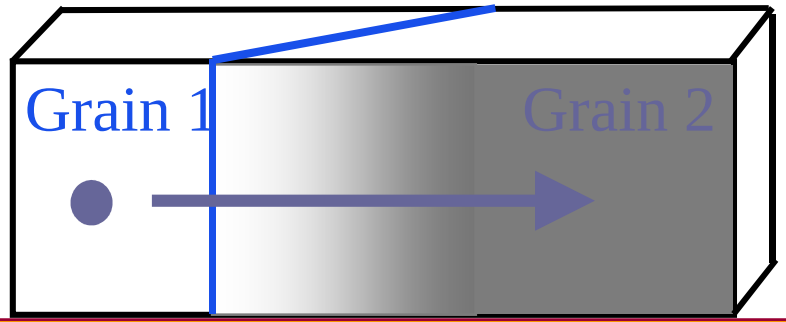
γ phase in Ni Superalloy

$R = 100\ (1 - Q_2/Q_1)$

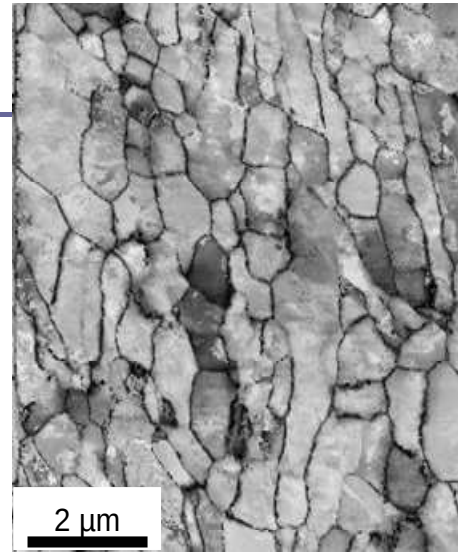
Orientation Reliability: 30

Reliability





reliability



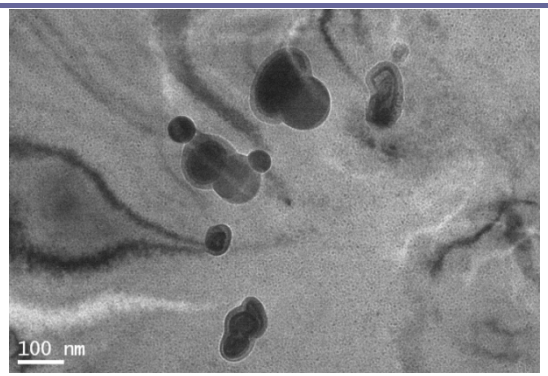
Fe - 60 ppmC severely deformed

Bright field

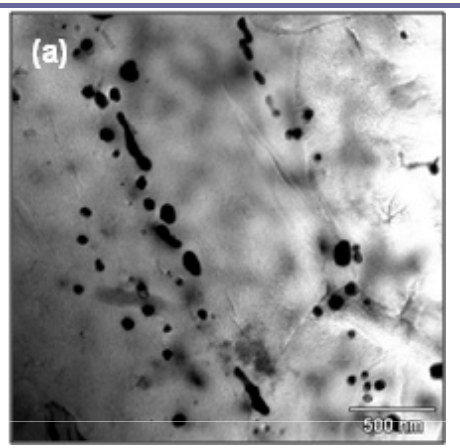
Orientation map

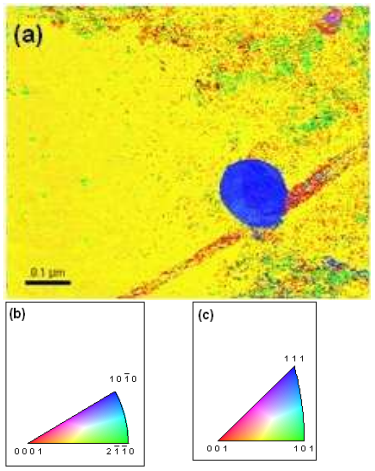


Tubo de Zr-2,5Nb para Indústria Nuclear

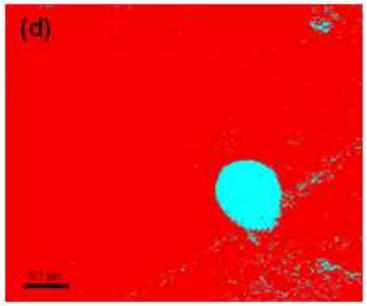


Micrografia de MET de Zr-2,5Nb CR

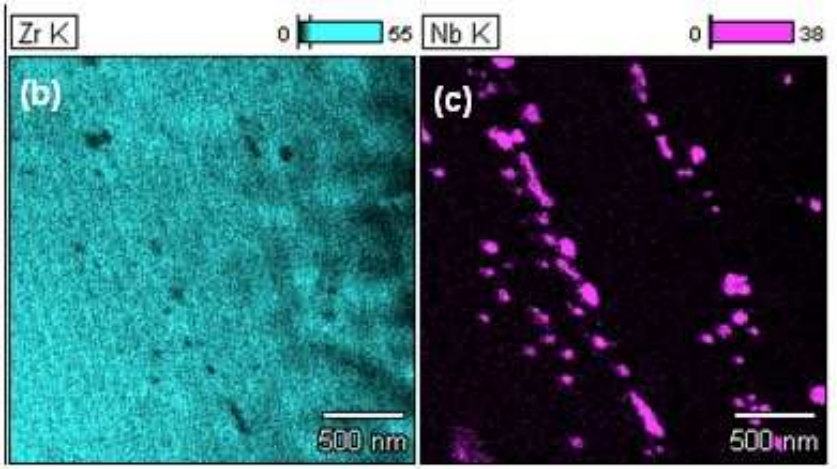




Mapa de orientação



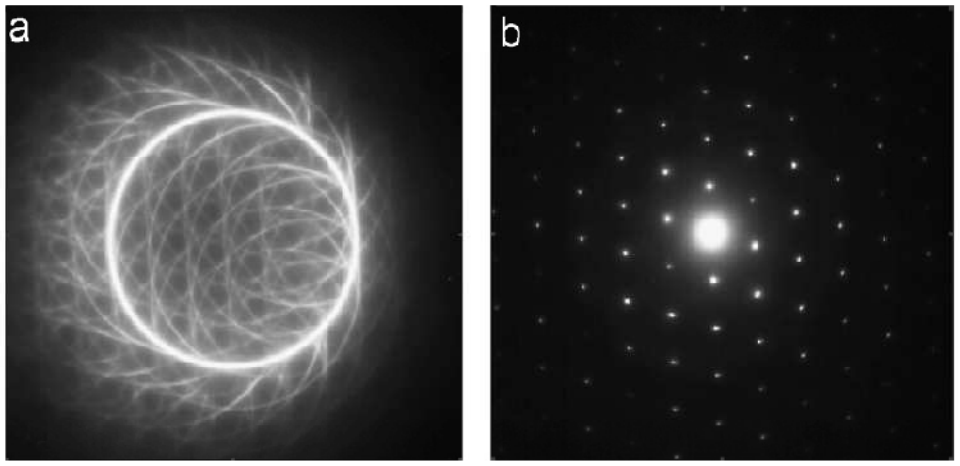
Mapa de Fases
Vermelho – fase α
Ciano – fase β_{II}



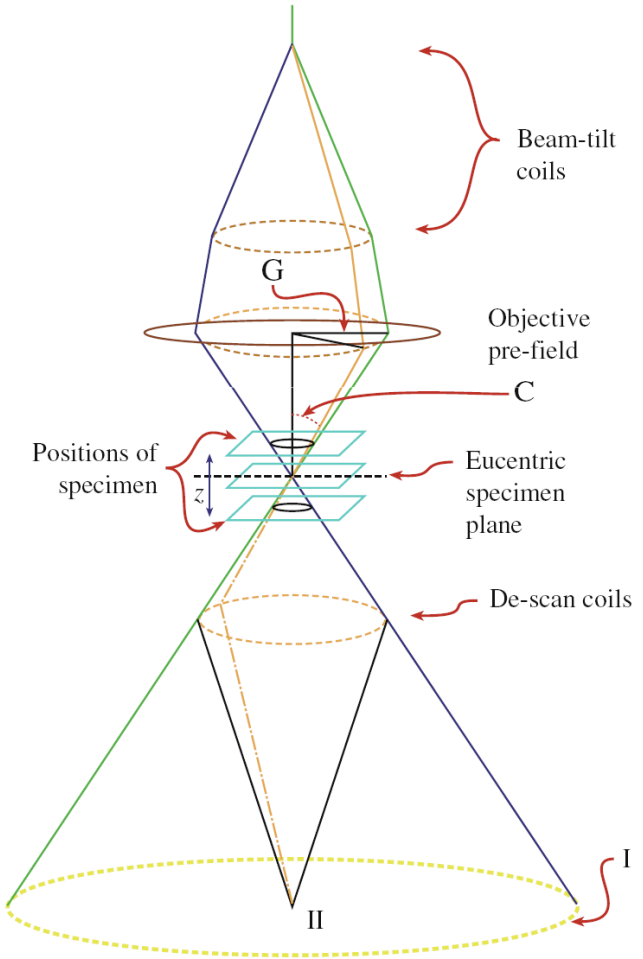
Micrografia de STEM e EDS de Zr-2,5Nb
Companhoni, Matheus, Marcondes e Pinto, J Mater Sci DOI 10.1007/s10853-012-6454-7

Difração com Precessão

- O feixe é inclinado com as bobinas que governam a execução de DP centrada e então girado
- É necessário realizar o giro inverso com as projetoras para reconstituir o DP

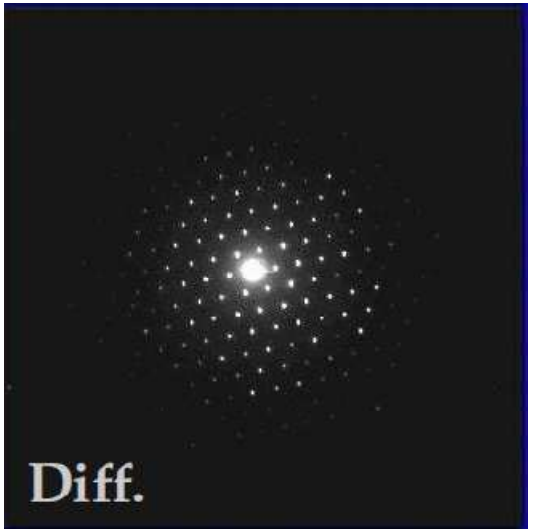


A. Avilov et al. / Ultramicroscopy 107 (2007) 431–444



Difração com Precessão

- O feixe é inclinado com as bobinas que governam a execução de DP centrada e então girado
- O padrão de difração integrado fica livre de efeitos dinâmicos



DP <111>
Granada de uvarovita ($Ca_3Cr_2(SiO_4)_3$ sem precessão

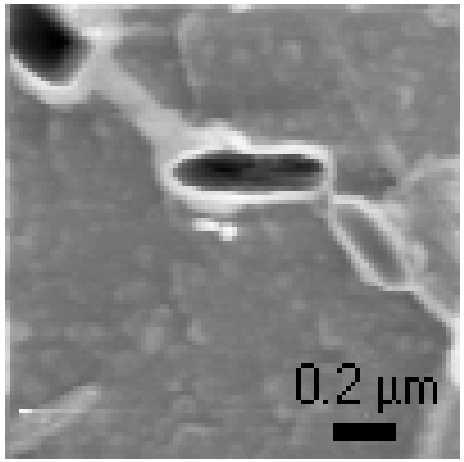


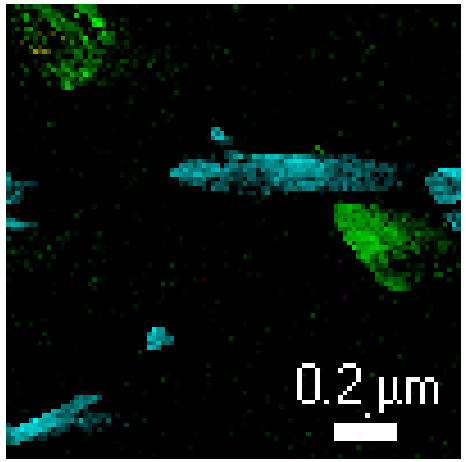
DP <111>
Granada de uvarovita (Ca3Cr2(SiO4)3 com precessão

Nanomegas/Grenoble INP

Aços CrMoW

- Aços Cr-Mo-W steels são empregados na indústria petroquímica e em termoelétricas
- A quantificação de fases é difícil mas ajuda a estimar a vida remanescente em fluência





M7C3 (Cr7C3)
M2C (Mo2C)
M6C (Fe3W3C)
Ferrite
Fe3C
MC (VC)

STEM e Catodoluminescência

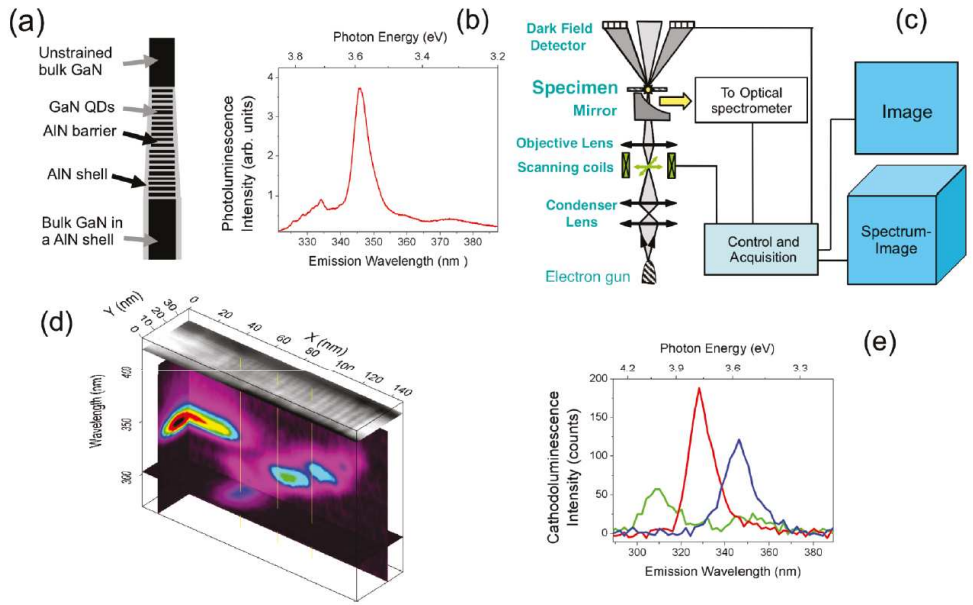


Figure 1. (a) Scheme of a GaN/AlN QDisks stack in a nanowire. (b) Photoluminescence of a typical GaN/AlN nanowire as schematized in (a) ($T = 4.2$ K The contributions of the different QDisks constituting the nanowire cannot be disentangled. (c) Principle of the cathodoluminescence spectral imagi setup in a STEM. (d) Typical output of a spectral imaging experiment. The top image is the HAADF image (GaN appears whiter, AlN darker), acquir simultaneously with the spectrum image. At each pixel (ca. 1 nm^2) a cathodoluminescence spectrum is acquired. After acquisition of the whole data s the information can be retrieved along various planes of the position-spectral 3D space. (e) Cathodoluminescence spectra extracted from the previo data set at position indicated by the thin yellow cylinders in (d). The contributions of different QDisks are much better disentangled.

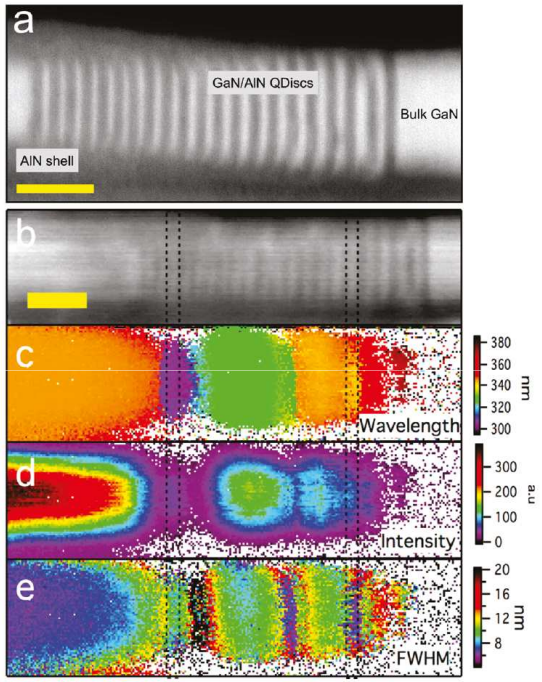
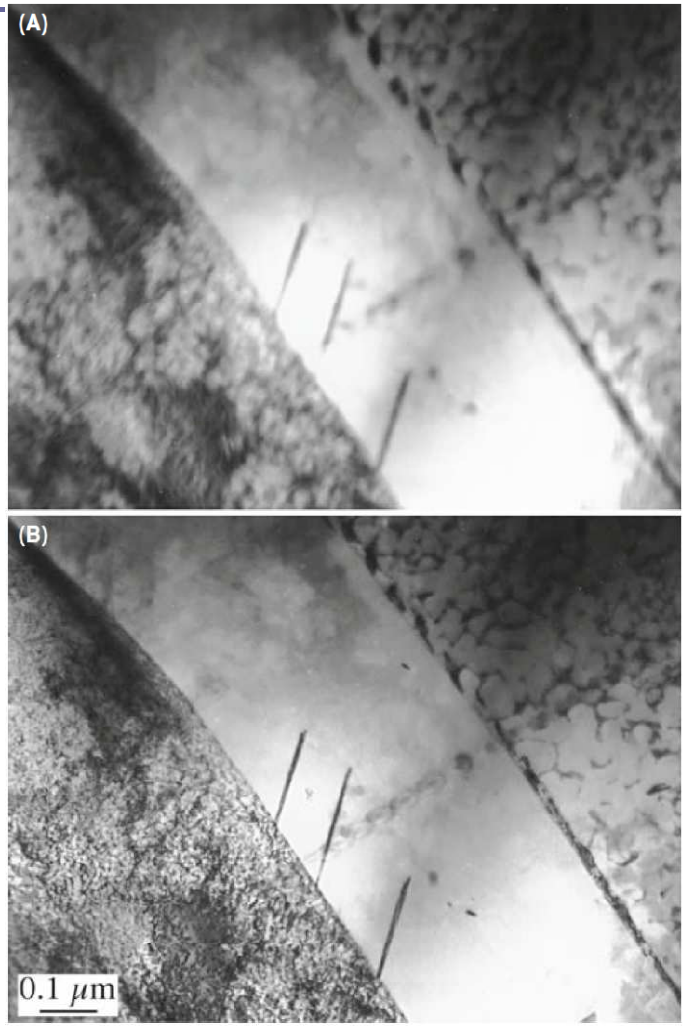


Figure 2. Spectral imaging of a GaN/AlN NW with 20 QDisks. It was acquired with 256 per 64 pixels of spatial sampling, 0.6 nm/pixel, and with 256 pixels of spectral sampling, 2 nm/pixel (wavelength), within less than 6 min. (a) HAADF image of a GaN/AlN nanowire (GaN appears whiter, AlN darker). Scale bar is 20 nm. (b) HAADF of the NW, acquired simultaneously with the CL. Scale bar is 20 nm. (c) Wavelength position of the most intense peak. (d) Intensity of the most intense peak. (e) Full width at half-maximum of the most intense peak. Some individual spectral features can be correlated to some individual quantum disks, as emphasized by the black dashed rectangles.

Zagonel et all. *Nano Lett.* 2011, 11, 568–573

Microscopia de Amostras Magnéticas

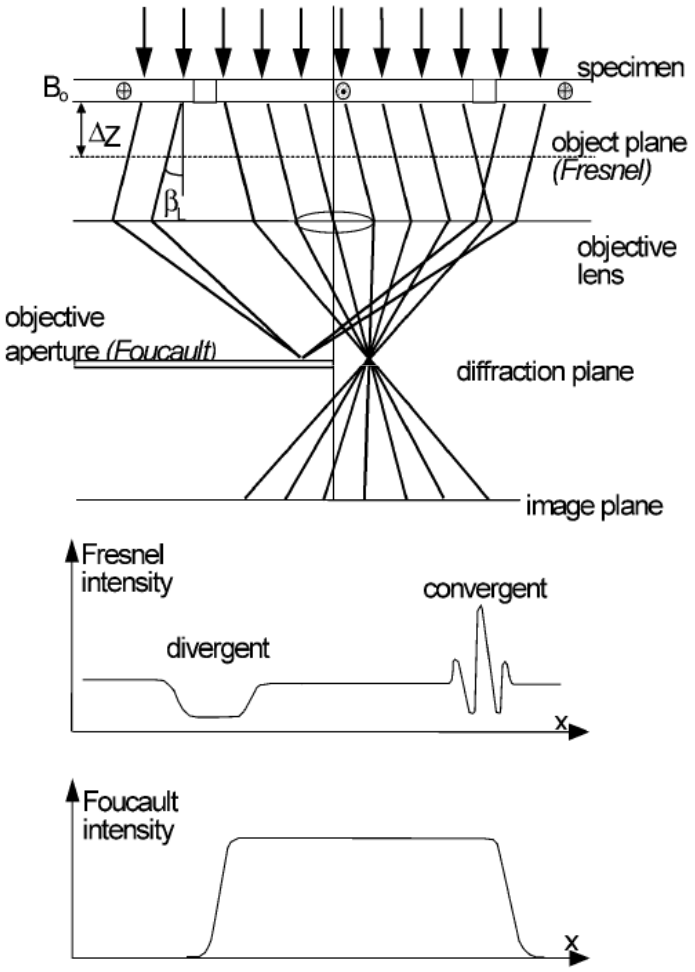
- Amostras devem estar em redes com grampo
- Objetivas devem ser desligadas durante a inserção
- Se a amostra sumir, desligue o microscópio
- Grande trabalho de alinhamento!!!
- DF centrada requer lentes especiais (Lorentz Microscopy)
- Lorentz Microscopy – lentes objetivas especiais de baixo campo na amostra de modo que os domínios magnéticos da amostra não sejam alterados pela objetiva



Williams e Carter, 2009

Microscopia de Lorentz

- Contraste de Fresnel
  - Modo TEM em campo claro
  - Desfocalização para delinear as paredes de domínios
- Contraste de Foucault
  - Campo escuro selecionando o spot fruto de desdobramento magnético

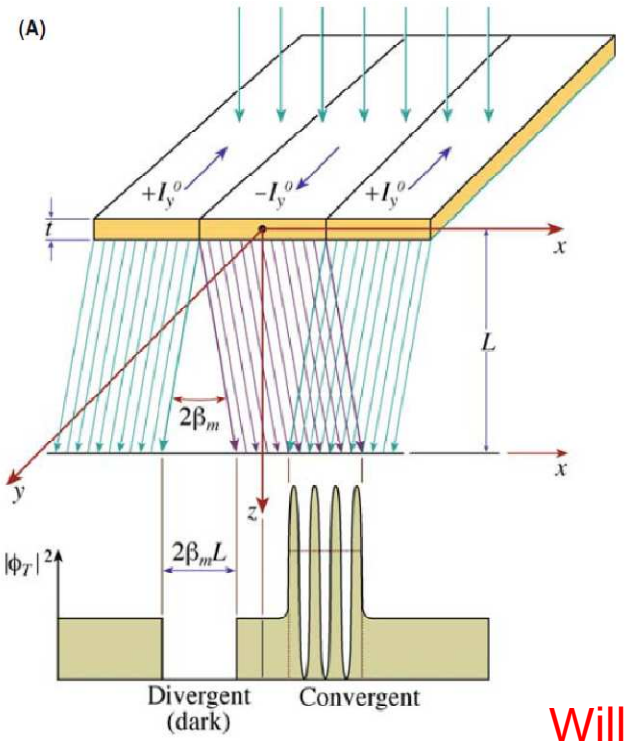


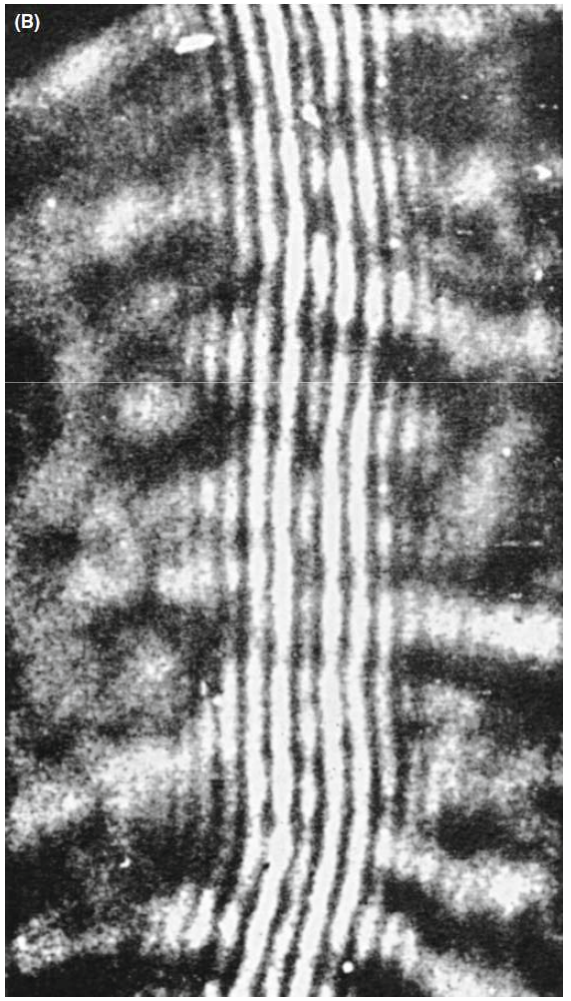
Chapman e Scheinfein, J. Mag. Mag. Mat 200 (1999) 729-740

Microscopia de Lorentz

Contraste de Fresnel

$$\Delta x = \frac{\lambda(L+\ell)}{2\ell\beta_m}$$

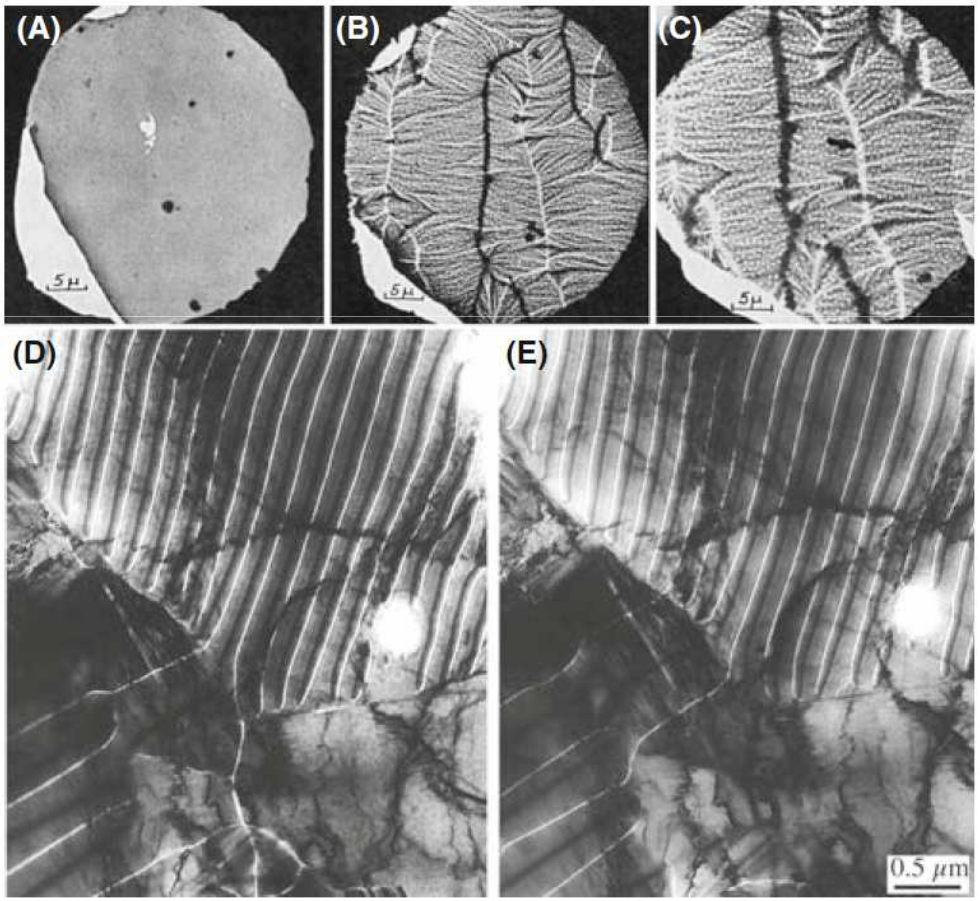




Williams e Carter, 2009

Microscopia de Lorentz

Contraste de Fresnel



Williams e Carter, 2009

Microscopia de Lorentz

É necessário trabalhar com uma lente objetiva que tenha menor campo magnético de modo a não alterar os domínios magnéticos da amostra

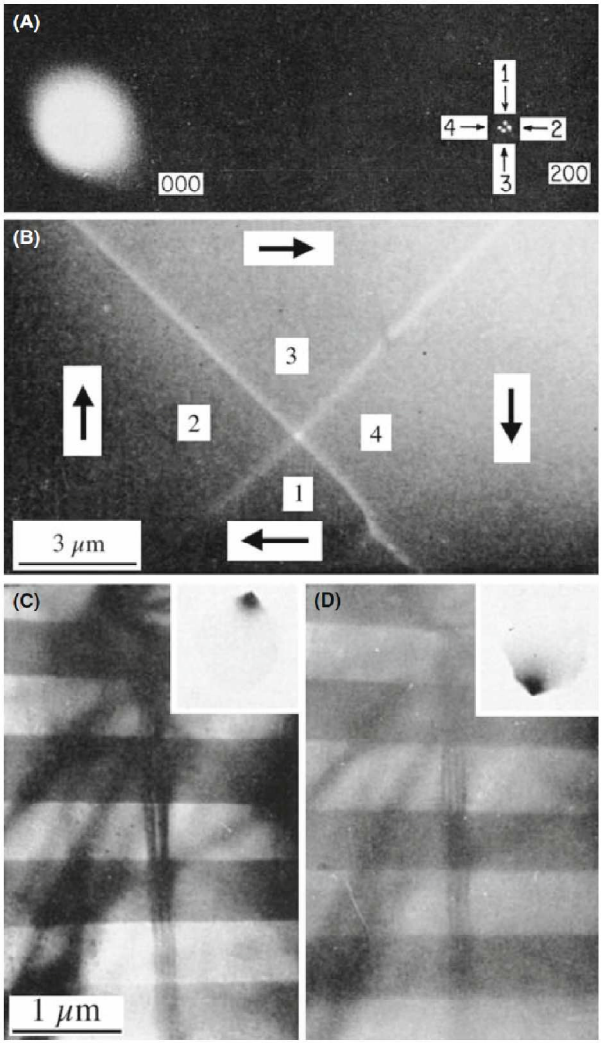
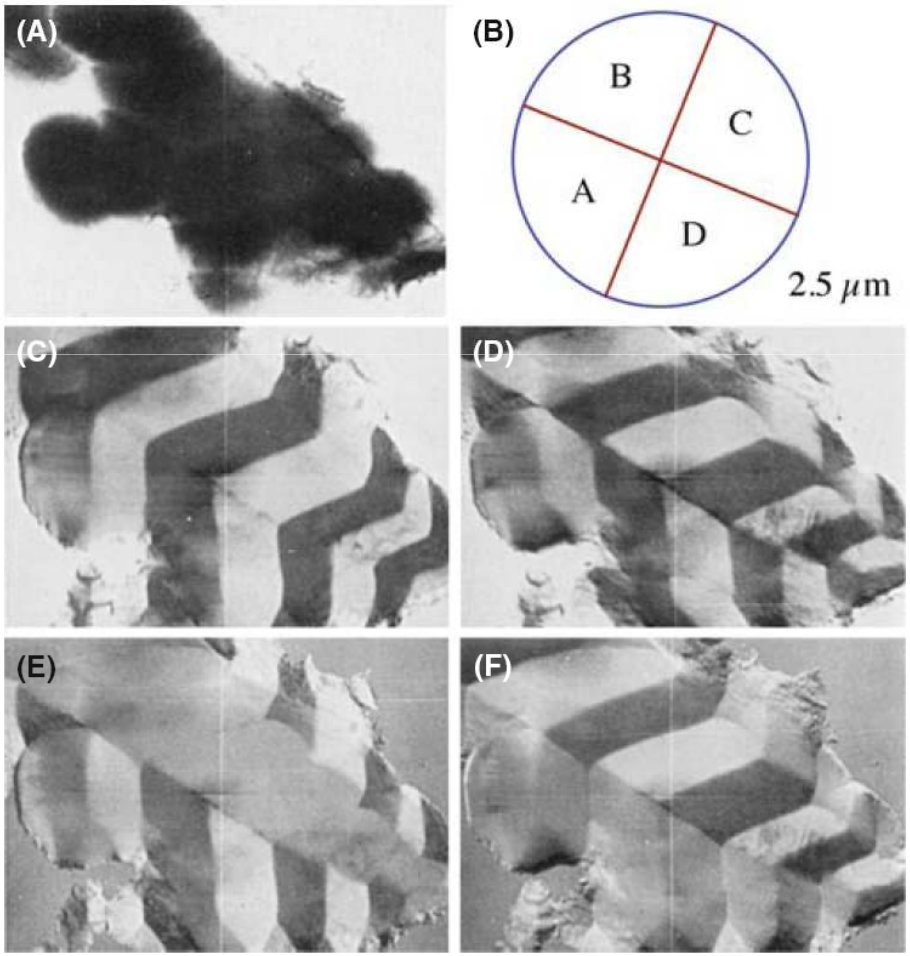


Imagem de Foucault
DF centrada

Williams e Carter, 2009

Microscopia de Lorentz



Imagens de Foucault de Fe puro utilizando os diferentes quadrantes de um detector de estado sólido obtidas em um STEM

Williams e Carter, 2009

Quase-Cristais

- As primeiras difrações dos quase-cristais que levaram ao Prêmio Nobel

VOLUME 53, NUMBER 20 PHYSICAL REVIEW LETTERS 12 NOVEMBER 1984

Metallic Phase with Long-Range Orientational Order and No Translational Symmetry

D. Shechtman and I. Blech
Department of Materials Engineering, Israel Institute of Technology–Technion, 3200 Haifa, Israel

and

D. Gratias
Centre d'Etudes de Chimie Métallurgique, Centre National de la Recherche Scientifique, F-94400 Vitry, France

and

J. W. Cahn
Center for Materials Science, National Bureau of Standards, Gaithersburg, Maryland 20760
(Received 9 October 1984)

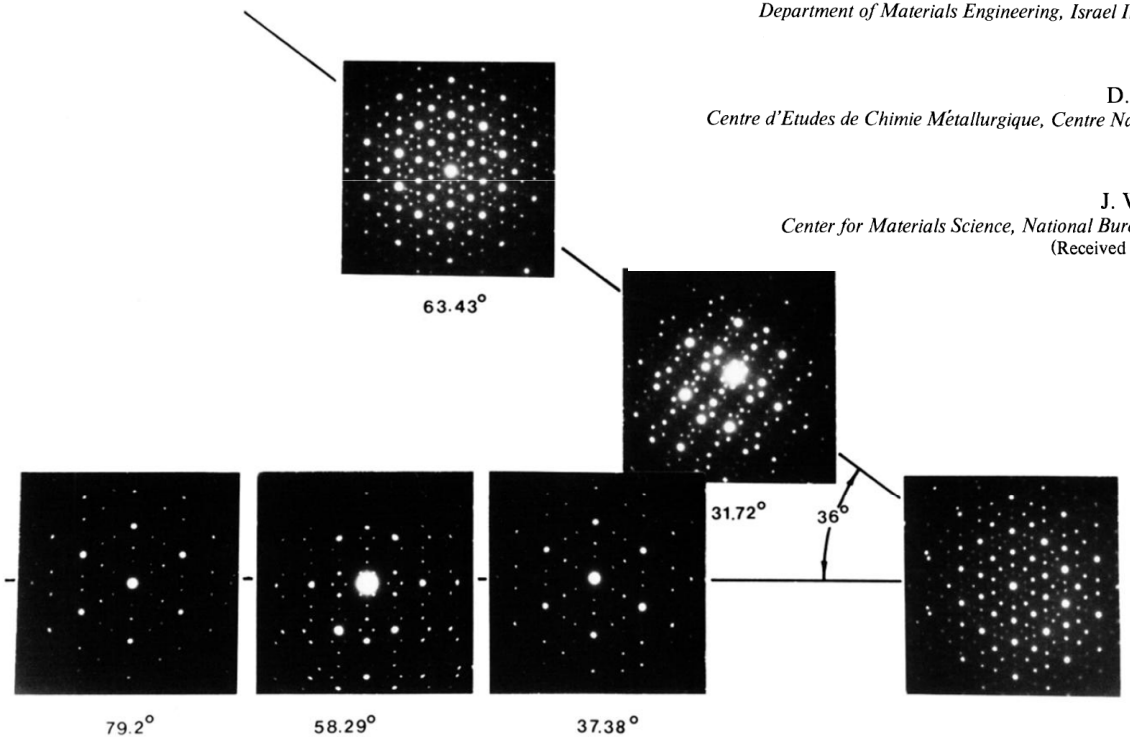


FIG. 2. Selected-area electron diffraction patterns taken from a single grain of the icosahedral phase. Rotations match those in Fig. 1.

Quase-Cristais

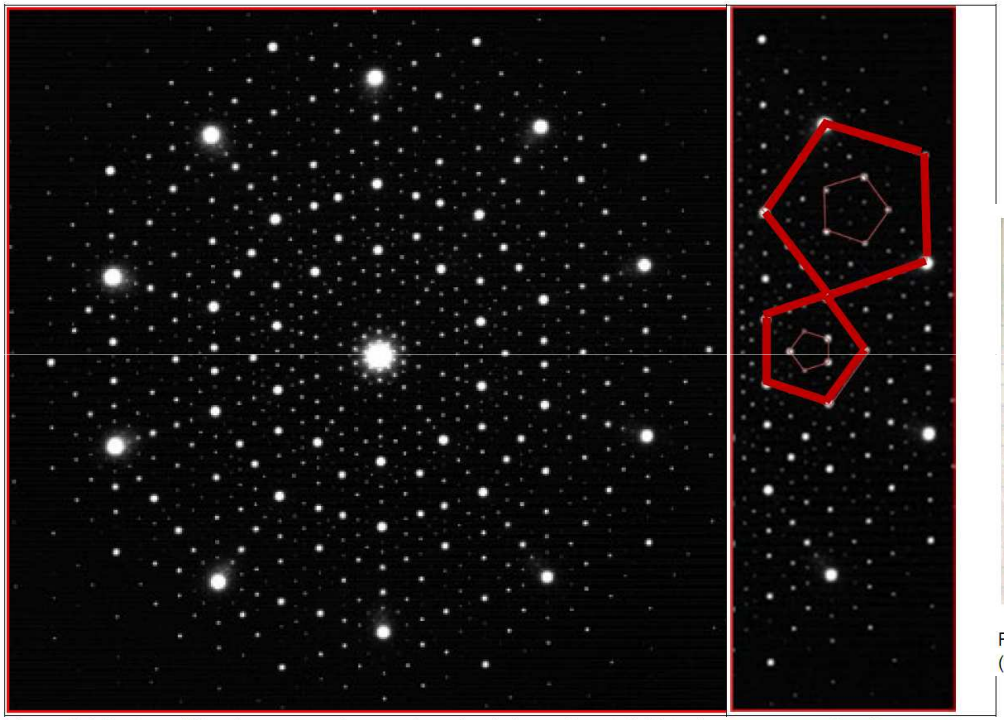


Figure 2. Electron diffraction pattern from an icosahedral quasicrystal. Note the presence of perfect pentagons highlighted in the diagram to the right. The linear scale between pentagons is τ, and the scale between a pentagon inscribed in another pentagon is τ^2. One of the great challenges of quasicrystal structure work is also apparent in this image. The intensity distribution of the diffraction pattern varies over many orders of magnitude, even in electron diffraction, and measuring the crucial weak reflections in an X-ray diffraction pattern within a reasonable time frame has only become possible with modern area detectors that were not around at the time of discovery.

http://www.nobelprize.org

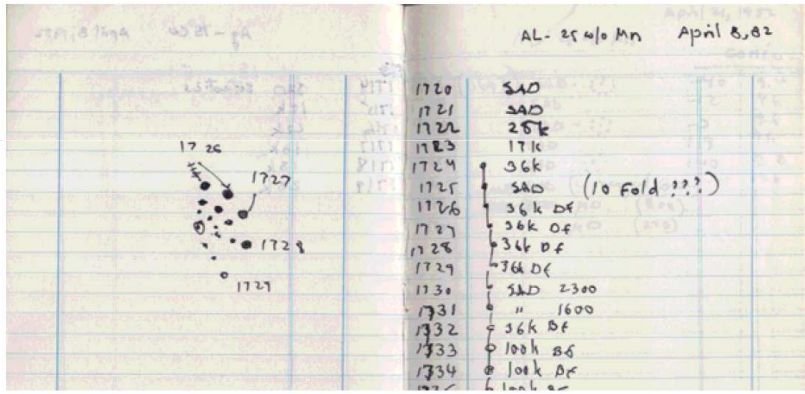


Figure 3. The notebook of Dan Shechtman dating the discovery of quasicrystals to 8 April 1982 (www.quasi.iastate.edu/discovery.html).

Quase-Cristais a partir de NP

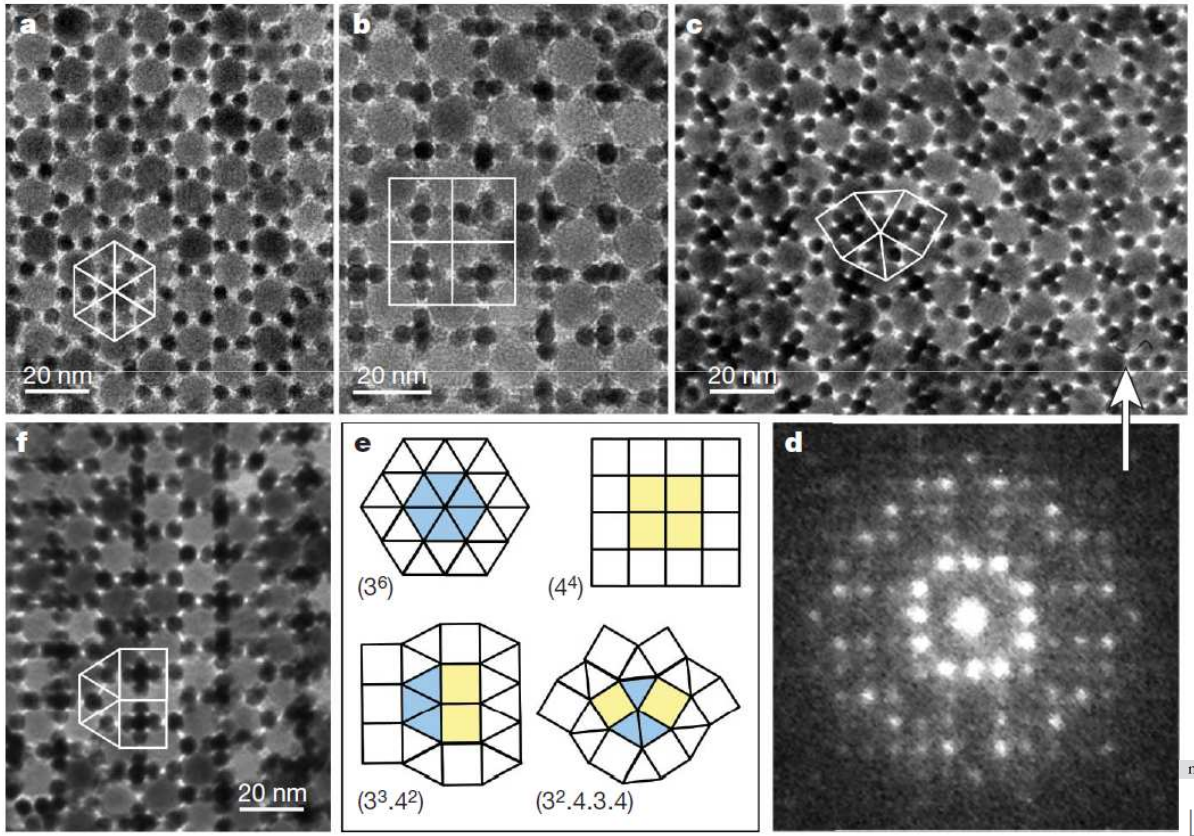


Figure 1 | Periodic binary superlattices self-assembled from 13.4-nm Fe_2O_3 and 5-nm Au nanocrystals. **a**, AlB_2-type superlattice; **b**, CaB_6-type superlattice; **c**, superlattice with AB_4 stoichiometry and the structural motif of the $(3^2.4.3.4)$ Archimedean tiling. **d**, Electron diffraction pattern measured from a ~6-μm^2 domain of the AB_4 superlattice shown in **c**. **e**, Archimedean tilings used to describe the structure of the nanoparticle superlattices. **f**, A fragment of a superlattice corresponding to the $(3^3.4^2)$ Archimedean tiling.

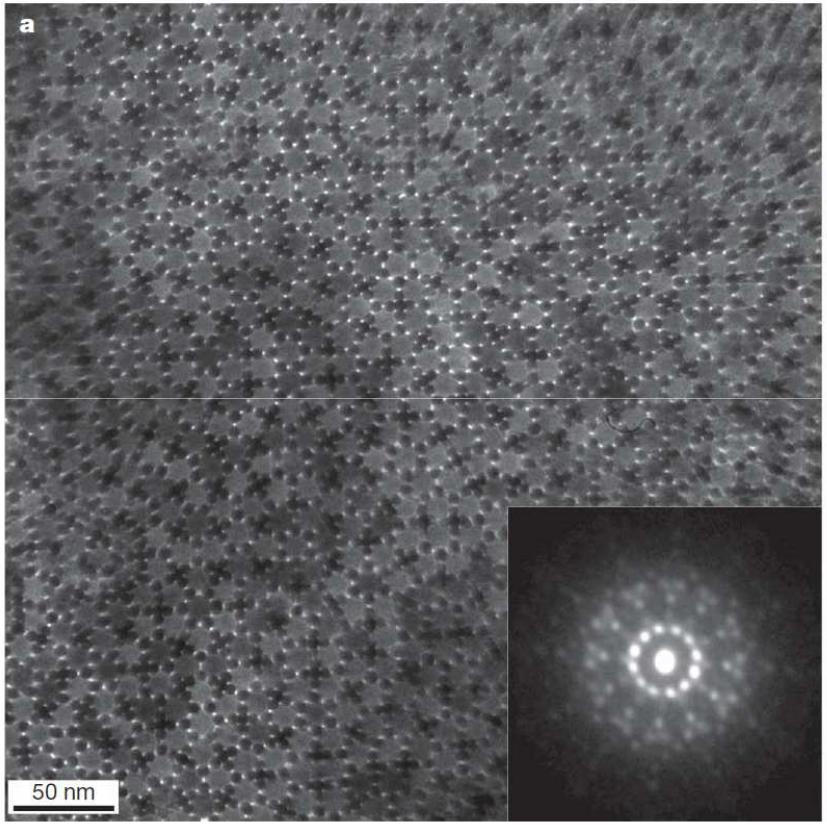
nature Vol 461|15 October 2009 doi:10.1038/nature08439

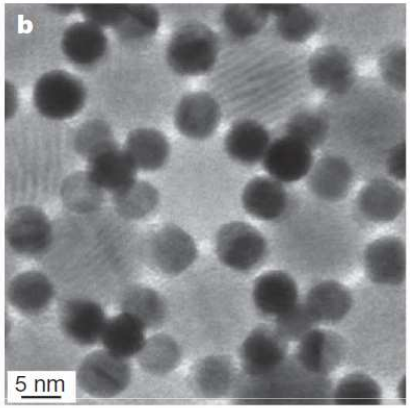
LETTERS

Quasicrystalline order in self-assembled binary nanoparticle superlattices

Dmitri V. Talapin[1,2]*, Elena V. Shevchenko[2]*, Maryna I. Bodnarchuk[1], Xingchen Ye[3], Jun Chen[4] & Christopher B. Murray[3,4]

Quase-Cristais a partir de NP





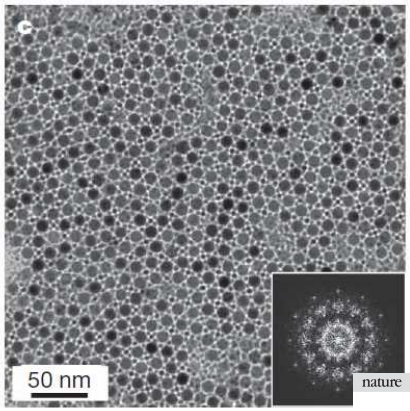


Figure 2 | Dodecagonal quasicrystals self-assembled from spherical nanoparticles. **a**, TEM image of a quasicrystalline superlattice self-assembled from 13.4-nm Fe_2O_3 and 5-nm Au nanocrystals. Inset, selected-area electron diffraction pattern with non-crystallographic 12-fold rotational symmetry measured from a ~6-μm^2 domain. **b**, Magnified view of a dodecagonal nanoparticle quasicrystal. **c**, Dodecagonal quasicrystalline superlattice self-assembled from 9-nm PbS and 3-nm Pd nanocrystals. Inset, fast-Fourier-transform pattern of the quasicrystalline superlattice.

nature Vol 461|15 October 2009 doi:10.1038/nature08439

LETTERS

Quasicrystalline order in self-assembled binary nanoparticle superlattices

Dmitri V. Talapin[1,2]*, Elena V. Shevchenko[2]*, Maryna I. Bodnarchuk[1], Xingchen Ye[3], Jun Chen[4] & Christopher B. Murray[3,4]

Quase-Crystal a partir de NP

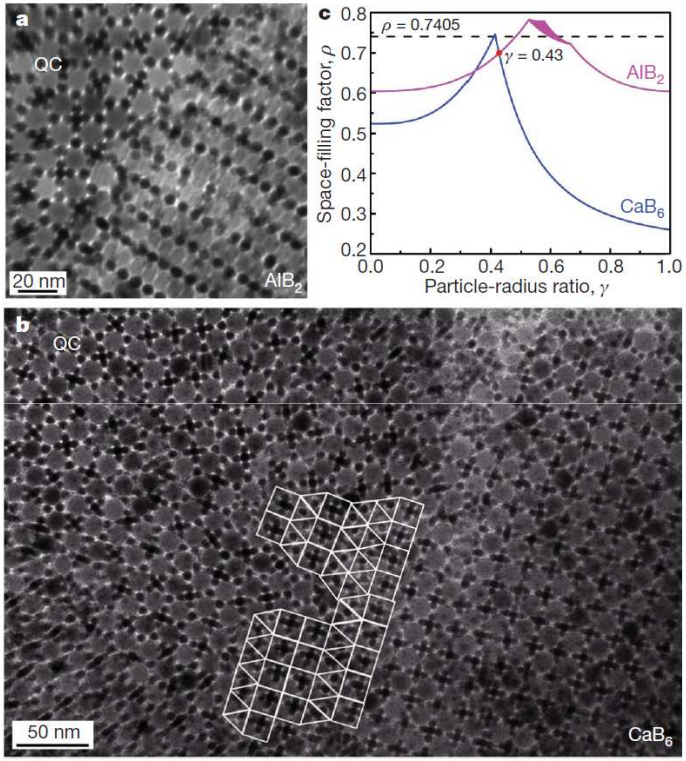


Figure 3 | Structure of the interface between quasicrystalline and crystalline phases. **a**, Interface between the DDQC phase and the AlB_2-type binary superlattice self-assembled from 13.4-nm Fe_2O_3 and 5-nm Au nanocrystals. QC, quasicrystal. **b**, Transition from the DDQC phase to the CaB_6-type binary superlattice of 12.6-nm Fe_3O_4 and 4.7-nm Au nanocrystals is facilitated by the presence of a 'wetting layer' of $(3^3.4^2)$ Archimedean tiling. **c**, Space-filling factors calculated for the AlB_2 and CaB_6 structures. The dotted line corresponds to the single-component close-packed structure with the space-filling factor $\rho = 0.7405$. The filled-in section in the AlB_2 line corresponds to different arrangements of densely packed spheres.

nature Vol 461|15 October 2009 doi:10.1038/nature08439

LETTERS

Quasicrystalline order in self-assembled binary nanoparticle superlattices

Dmitri V. Talapin[1,2]*, Elena V. Shevchenko[2]*, Maryna I. Bodnarchuk[1], Xingchen Ye[3], Jun Chen[4] & Christopher B. Murray[3,4]

Avaliando a tensão entre precipitado (Pb) e matriz (Al)

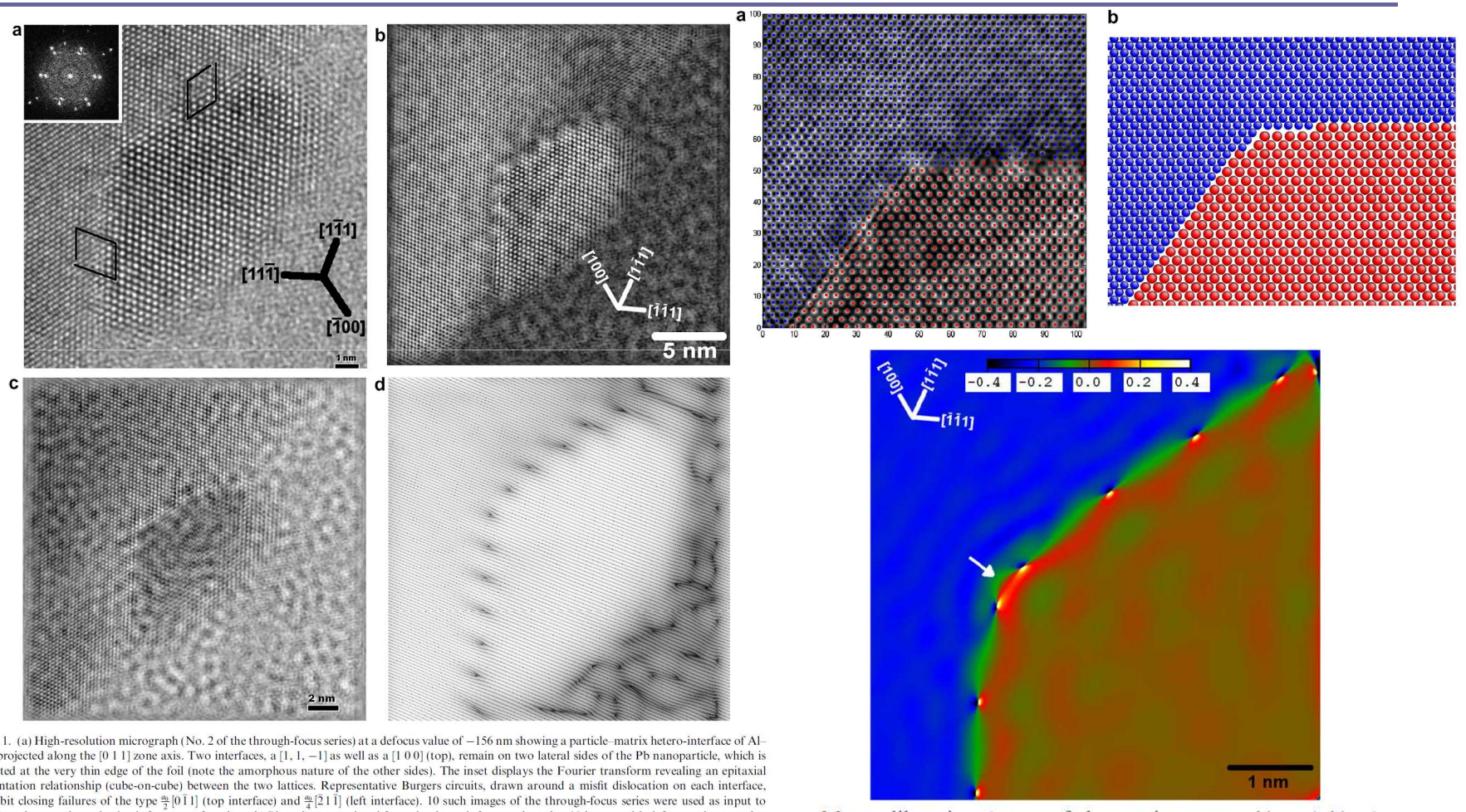


Fig. 1. (a) High-resolution micrograph (No. 2 of the through-focus series) at a defocus value of −156 nm showing a particle–matrix hetero-interface of Al–Pb projected along the [0 1 1] zone axis. Two interfaces, a [1, 1, −1] as well as a [1 0 0] (top), remain on two lateral sides of the Pb nanoparticle, which is located at the very thin edge of the foil (note the amorphous nature of the other sides). The inset displays the Fourier transform revealing an epitaxial orientation relationship (cube-on-cube) between the two lattices. Representative Burgers circuits, drawn around a misfit dislocation on each interface, exhibit closing failures of the type $\frac{a_0}{2}[0\bar{1}1]$ (top interface) and $\frac{a_0}{2}[2\,1\,\bar{1}]$ (left interface). 10 such images of the through-focus series were used as input to retrieve the complex-valued exit-face wave function. (b) Phase image retrieved from the through-focus series using 10 images with defocus values ranging from −154 to −203 nm as input. (c) Amplitude image retrieved from the through-focus series using 10 images with defocus values ranging from −154 to −203 nm as input. (d) Filtered phase image showing the (1, −1, 1) lattice fringes only. The misfit dislocations are clearly visible. Note the lateral offset of the individual dislocation cores from each other.

Mean dilatation (trace of the strain tensor: $\frac{1}{2}\varepsilon_{xx} + \frac{1}{2}\varepsilon_{yy}$)

H. Rösner et al. / Acta Materialia 58 (2010) 162–172

Quantum Dots

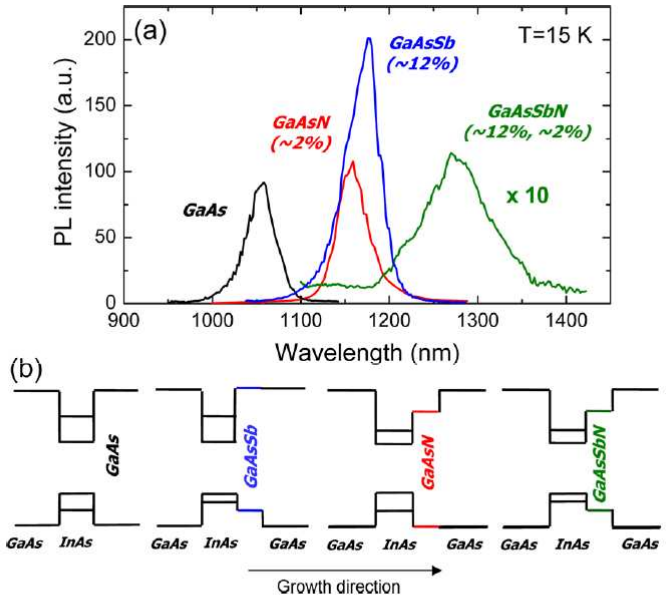


FIG. 1. (Color online) (a) 15 K PL spectra of four InAs/GaAs QD layers capped with different materials: GaAs, GaAsSb, GaAsN, and GaAsSbN. The nominal Sb and N contents in the quaternary alloy are the same as in the ternary counterparts. (b) Sketch of the expected band structure in each case.

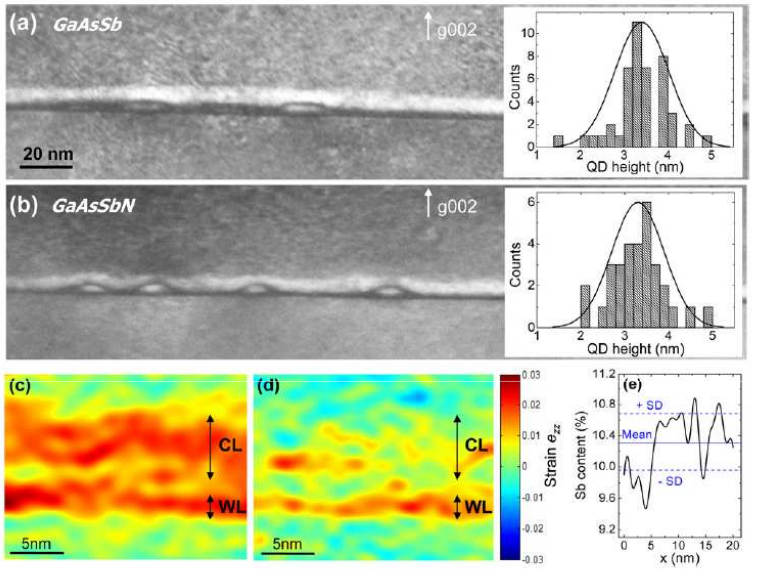


FIG. 2. (Color online) g002 dark field TEM images of samples S-Sb (a) and S-SbN (b). The insets show the measured QD height distribution in each case. (c) and (d) show the strain maps obtained from HRTEM images acquired along the [011] zone axis of samples S-Sb and S-SbN, respectively. (e) shows the deduced Sb content profile along the [011] direction in sample S-Sb. The mean value is 10.3% and the standard deviation (SD) 0.4%.

Ulloa *et al.* Appl. Phys. Lett. **100**, 013107 (2012)

Criando modelos de nanocristais

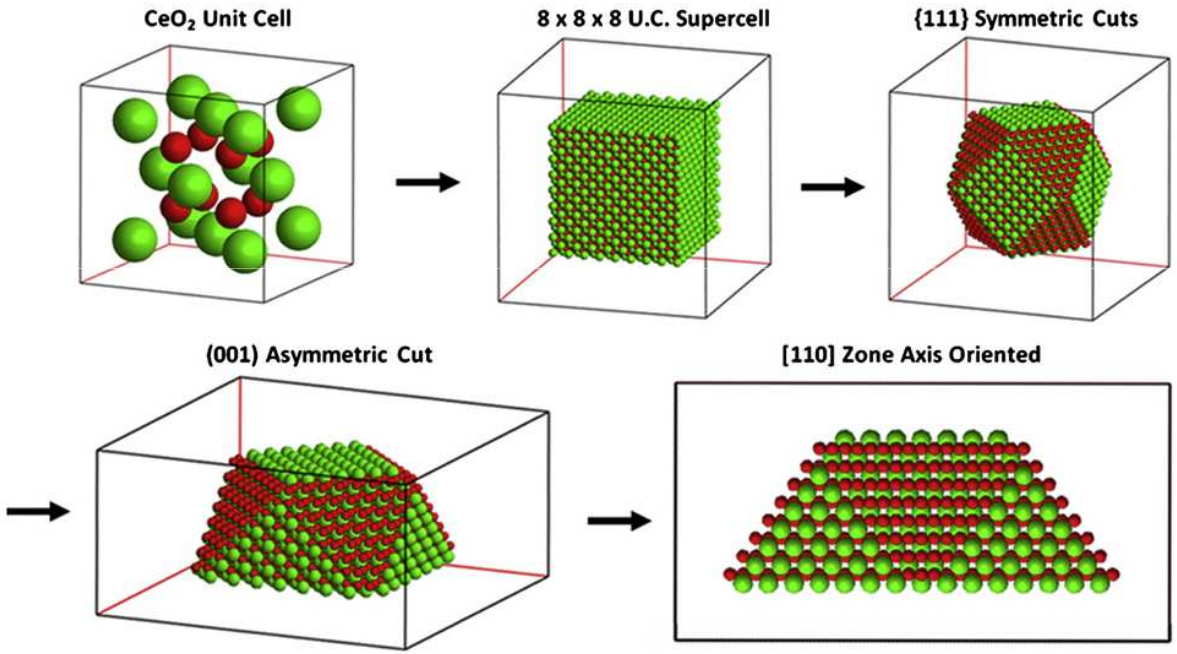


Fig. 3. Construction example at each operation step.

D.G. Stroppa et al. / Ultramicroscopy 111 (2011) 1077–1082

Simulando nanocristais em HRTEM

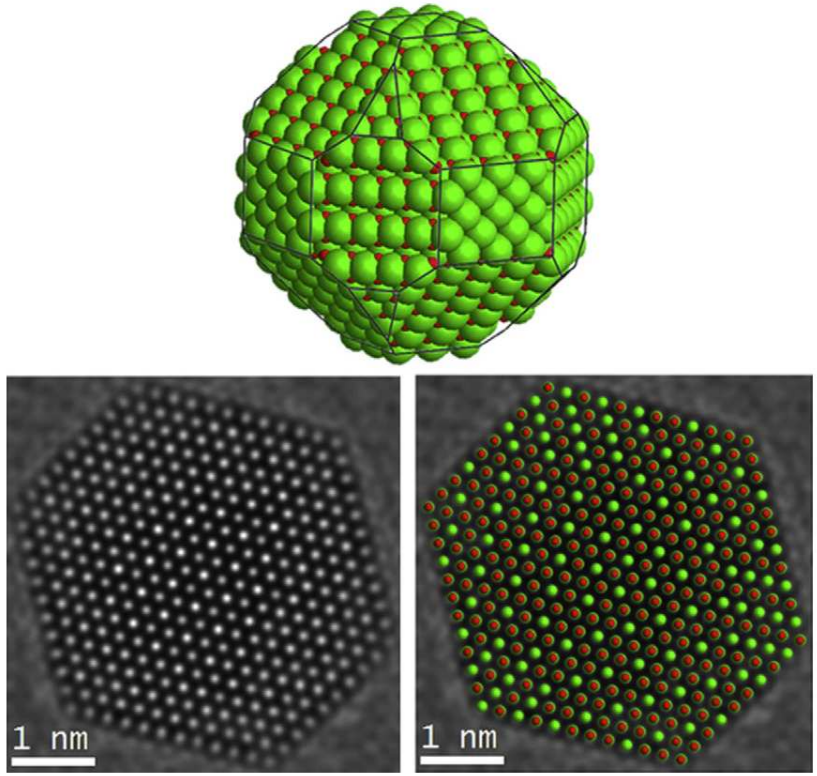


Fig. 4. (a) Trimetric view of a CeO_2 faceted nanocrystal model (example 1, Ce atoms in green), (b) ⟨1 1 1⟩ Zone Axis HRTEM multislice simulation (300 kV; Cs=0.7 mm; dF=−64 nm), and (c) simulated image and model structure superimposition. (For interpretation of the references to color in this figure legend, the reader is referred to the web version of this article.)

D.G. Stroppa et al. / Ultramicroscopy 111 (2011) 1077–1082

Simulação x HRTEM

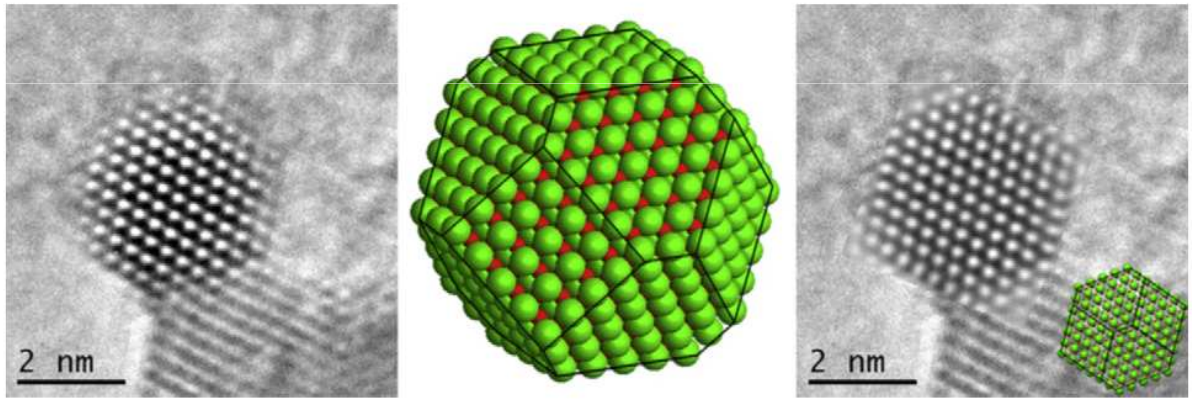
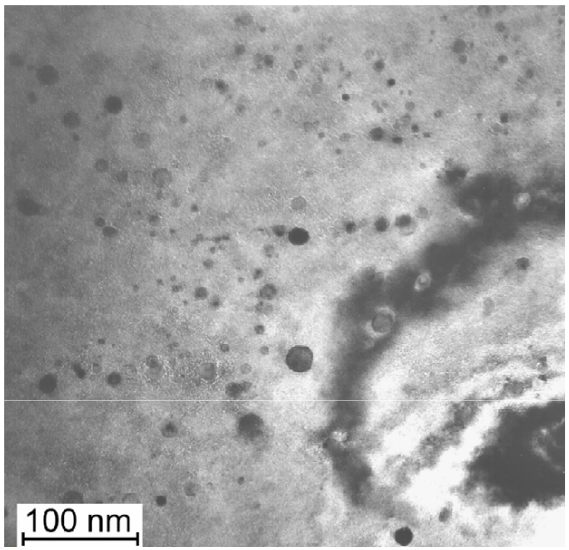
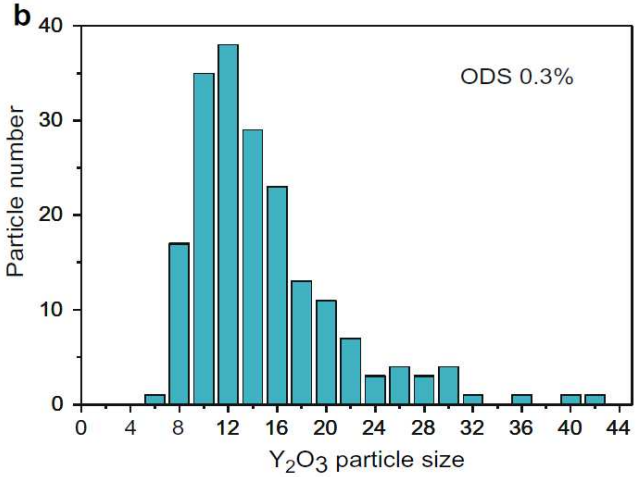


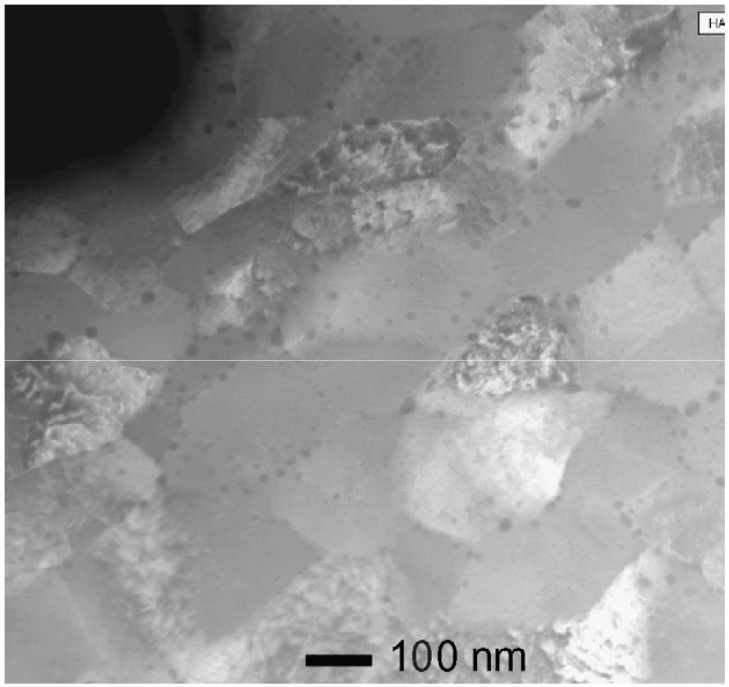
Fig. 8. CeO_2 nanocrystal characterization supported by MEGACELL. The geometrical analysis of the original HRTEM image (left) supported the construction of geometrical models (center), whose adequacy was tested by the superimposition of the simulated frames and the original HRTEM images (right). Surface area ratio of the exposed {1 0 0} to the {1 1 1} facets could be retrieved from the geometrical model and its value is approximately 0.66.

D.G. Stroppa et al. / Ultramicroscopy 111 (2011) 1077–1082

RAFM ODS 9Cr1W0.3Y_2O_3 Steel







Ch.Ch. Eiselt et al. / Journal of Nuclear Materials 385 (2009) 231–235

Obrigado pela atenção!

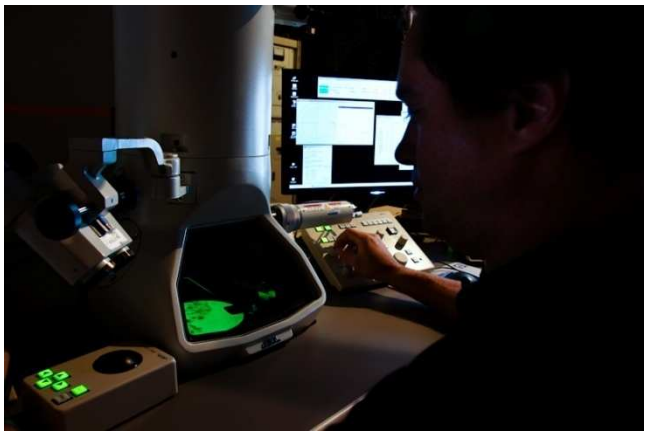


50 anos
PÓS-GRADUAÇÃO CBPF

www.cbpf.br/labnano

Contato:
André L. Pinto
pinto@cbpf.br





Referências

- Williams, D. B. e Carter, C. B., "Transmission Electron Microscopy" , Ed. Springer, 2009.
- Goodhew, P. J. et all, "Electron Microscopy and Analysis", Ed. Taylor & Francis, London, 2001
- Apresentação da Jeol – MET
- Pei, Y. T. et al. *Nanostructured TiC/a-C coatings for low friction and wear resistant applications.* Surface & Coatings Technology 198 (2005) 44.
- Wang, Z. L.m Transmission Electron Microscopy of Shape-Controlled Nanocrystals and their Assemplies. J. Phys. Chem. B 104 (2000) 1153.
- Companhoni, Matheus, Marcondes e Pinto, Analysis of microstructure and microhardness of Zr-2.5Nb processed by High-Pressure Torsion (HPT). J. Mater. Sci. DOI 10.1007/s10853-012-6454-7
- Lima, Pinto et all, Quantitative observatins of precipitation in 2.25Cr-1Mo steel exposed to different creep conditions in a power station. Eng. Fail. Analysis 16 (2009) 1493.

Referências

- Qin, F. X. et al. *Microstructure and electrochemical behavior of Ti-coated $Zr_{55}Al10Ni_5Cu30$ bulk metallic glass*. Intermetallics 17 (2009) 945.
- Larrude, Maia da Costa, Monteiro Pinto e Freire, Characterizayion of phosphorous-doped multiwalled carbon nanotubes. J. Appl. Phys. 111 (2012) 064315.
- Rodrigues, V. e Ugarte, D. Metal nanowires: atomic arrangement and electrical transport properties. Nanotechnology 13 (2002) 404.
- Ryou et al. Properties of InP self-assembled quantum dots embedded in In0.49(AlxGa1-x)0.51P for visible light emitting laser applications grown by metalorganic chemical vapor deposition. J. Appl. Phys. 91, 8 (2002) 5313.
- Zagonel et all. Nanometer scale spectral imaging of quantum emitters in nanowires and its correlation to their atomically resolved structure. Nano Lett. 11 (2011) 568
- Rösner et all. Strain mapping along Al-Pb interfaces. Acta Materialia 58 (2010) 162.
- Chapman e Scheinfein, J. Mag. Mag. Mat 200 (1999) 729-740

Referências

- Stroppa et al. MEGACELL: A nanocrystal model construction software for HRTEM multislice simulation. Ultramicroscopy 111 (2011) 1077
- Talapin et al. Quasicrystalline order in self-assembled binary nanoparticle superlattices. Nature 461 (2009) 964
- Shechtman et al. Metallic phase with long-range orientational order and no translational symmetry. Physical Review Letters 53 (1984) 1951
- http://www.nobelprize.org/nobel_prizes/chemistry/laureates/2011/advanced-chemistryprize2011.pdf
- Eiselt et al. Journal of Nuclear Materials 385 (2009) 231